CDS 99-003

Passive Control of Flutter and Forced Response in Bladed Disks via Mistuning

Thesis by

Benjamin Shapiro

In Partial Fulfillment of the Requirements
for the Degree of
Doctor of Philosophy

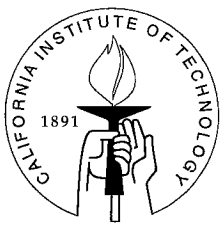

California Institute of Technology
Pasadena, California

1999
(Submitted May 7, 1999.)

Acknowledgments

To my parents, Alex and Julia Shapiro, for their love, support, concern and vast quantities of food. In all ways, they gave me the drive necessary to get this far. To my brother, Dan Shapiro, for his ability to see the humour in any situation. His company and friendship made my many trips to the East coast a pleasure, instead of just a chore. To my advisor, Richard Murray, for his honesty, interest, excitement and advice. I could not have asked for a better advisor. To the people I worked with at United Technologies, Dan Gysling, Scott Copeland and Sriram Srinivasan, for their interest and help. They gave me a valuable industry insight that goes beyond this thesis. And to my friends who are too many to name, for dancing, sport, conversation and laughter which made graduate school a pleasure. All of you made my time at Caltech unforgettable.

Abstract

Mistuning or blade to blade variation in jet-engine bladed-disks can lead to large changes in engine performance. Even the small random mistuning associated with manufacturing tolerances can significantly change both stability boundaries and forced response. This thesis addresses two questions. Analysis: given any mistuning (random or intentional), what is the resulting change in performance? And passive control: can intentional mistuning be used to improve stability and forced response in a robust manner?

A general framework based on symmetry arguments and eigenvalue/vector perturbations is presented to answer both questions. Symmetry constrains all facets of mistuning behaviour and provides simplifications for both the analysis and control problems. This is combined with the eigenvalue/vector perturbation which captures the nonlinear mistuning dependence and solves the analysis problem. It is shown that intentional mistuning can provide robust damping and so guarantee improved stability and forced response under fixed manufacturing tolerances. Results are demonstrated on a high-fidelity low-order model derived from computational-fluid-dynamic data.

Contents

List of Figures

List of Tables

Chapter 1 Introduction

The gas turbine power plants used in todays airplanes, helicopters, ships and power generators are complex, high-performance devices whose development dates back as far as a patent issued to J. Barber in 1791 [Bat84, Pot72]. Although jet-engines have been built and operated successfully for the last four decades, their inherent complexity still gives rise to unexpected behaviour. Figure 1.1 shows a typical aircraft jet-engine. It contains complex moving parts which interact with high-speed high-pressure airflow. The result is a host of complex behaviours and potential instabilities. Some of these are shown in Figure 1.2 and

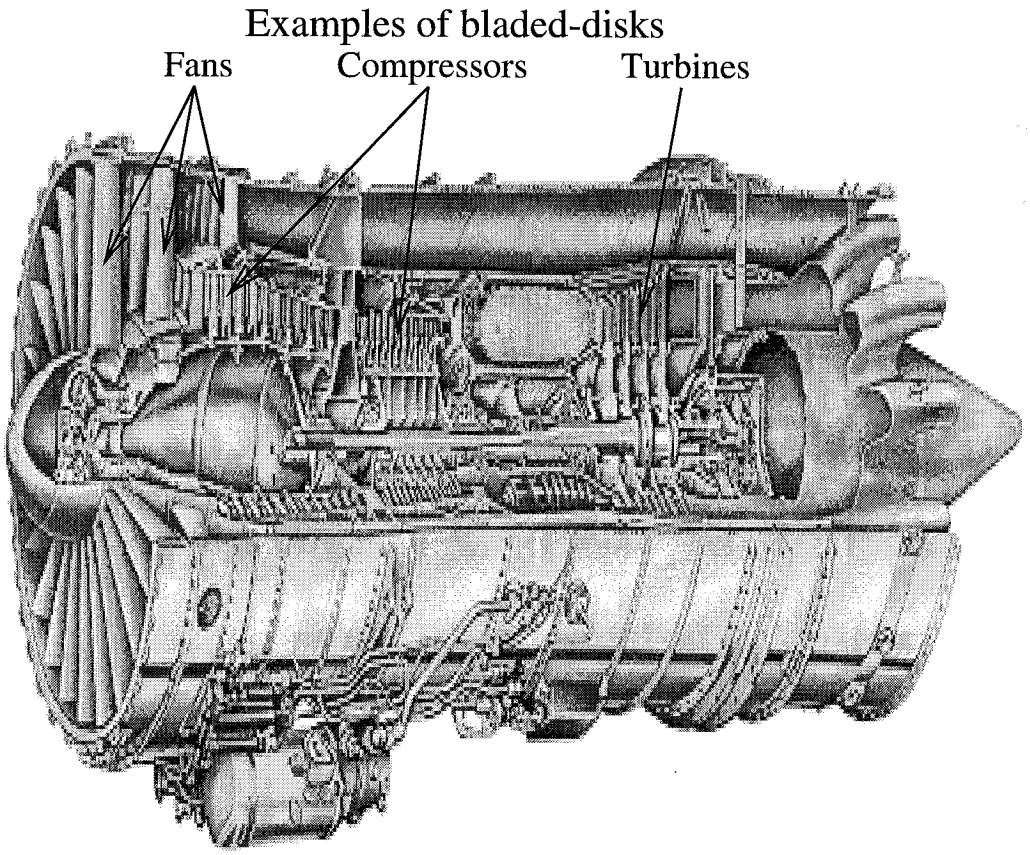

Figure 1.1: Pratt & Whitney JT8D jet-engine.

interested readers are referred to [Gre81] for a general overview of turbomachinery instabilities. In particular, the interaction of spinning rotors with fast flowing compressed fluid and

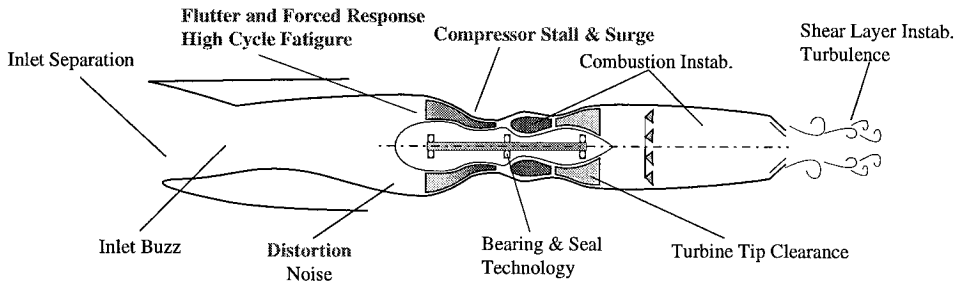

Figure 1.2: Turbomachinery instabilities. (Figure courtesy J. Paduano)

its associated wakes (shed from upstream stationary objects such as stators and inlet guide vanes) may create severe instabilities and unacceptable forced response in bladed disks. If caught within the design cycle, such unexpected behaviour creates time-delays and additional costs. When instabilities and performance drops are first noticed in operation, they can increase operating costs, require engine recalls and at worst cause loss of life. Our concern is with the behaviour of bladed-disks; specifically we focus on the dynamics of fans and compressors found in jet-engines (see Figure 1.1). We address two issues: flutter instabilities and forced response.

Flutter refers to unstable blade vibrations caused by coupling between aerodynamics and blade mechanics. Such vibrations can cause blade failure and so engines must be designed to operate away from flutter boundaries. Unfortunately, flutter is encountered in many regimes of engine operation (see Figure 1.3) and hence drastically limits engine performance. Consequently, the ability to eliminate or reduce the severity of flutter can lead to increased safety, higher efficiency and significant cost and weight savings in future engine designs.

Forced response refers to stable blade vibration caused by aeromechanical disturbances. For instance, the rotating disk spins past stationary objects such as struts and inlet guide vanes. These objects provide a stationary aerodynamic disturbance, either via a flow distortion or through shed wakes. Mechanical forcing may also be created by small shaft imbalances. Blade forced response vibrations cause high-cycle metal fatigue (basically crack growth) which can ultimately lead to blade failure. Large vibration amplitudes speed crack growth, reduce blade life and increase operating and maintenance costs. Moreover, in the case of unexpectedly large vibrations, cracks initially below the detection limit may prop-

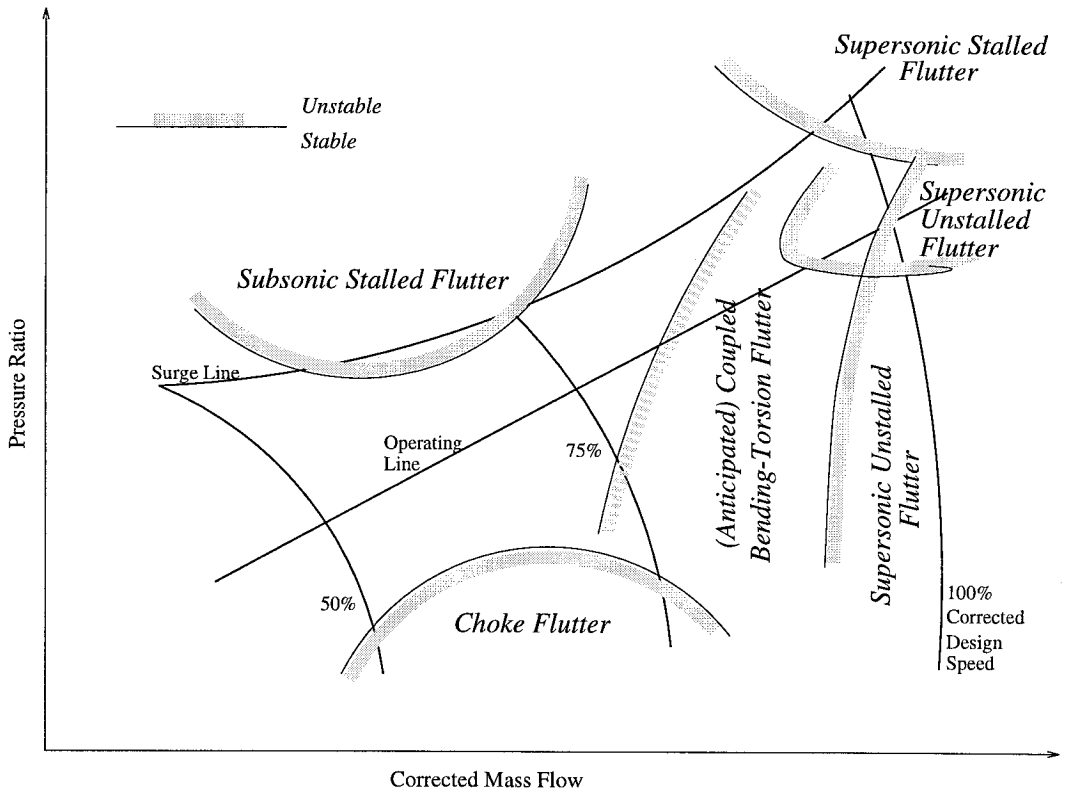

Figure 1.3: Compressor map showing typical flutter boundaries [Ben86].

agate faster then predicted and cause catastrophic failure between assigned blade checks. Hence it is crucial to predict correct (or conservative) forced response amplitudes under manufacturing and wear uncertainties.

The high-cycle fatigue (HCF) caused by forced-response in (titanium) engine parts has been identified as the dominant unexpected engine failure mode from 1989 to 1994 [Dav95] and as the predominant cause of several hundred accidents over the past three decades [SAB92]. These incidents have ranged from Class A mishaps down to maintenance actions. (Class A mishaps involve either: (a) property damage in excess of one million dollars, (b) Air Force aircraft damaged beyond economical repair, or (c) human fatality or a permanent and total disability.) Moreover, HCF problems are typically difficult to identify prior to failure even though the root cause may have been present for some time. As a result, it is very difficult to guard against HCF in the field. Such data forces an obvious question: what causes these surprise HCF failures?

One contributing factor is blade asymmetry caused by manufacturing tolerances or wear

and tear, which can lead to large asymmetric forced response with resulting HCF. Ideally, fans or compressors are tuned (meaning all blades are identical). In reality, manufacturing along with engine wear creates mistuning (blades differ from one another). It is well known that even a small amount of mistuning can induce a large asymmetric forced response known as mode-localization [DH69, MM88]. However, only certain mistuning patterns lead to an unacceptable response. Since the majority of engines remain operational the probability of these patterns occurring must be small. Still, the same probability may be unacceptably large by safety standards (we show such an example in Section 5.2.2). HCF failure due to mistuning displays all the symptoms cited above: failure due to an unacceptable mistuning pattern is unexpected (of low probability and probably not seen or predicted by any experiment or analysis) and it is dormant (root cause present for considerable time before failure).

Not only does mistuning dramatically affect forced response (and associated HCF) but it can also significantly change the performance limiting flutter boundaries of Figure 1.3. Figure 1.4 shows data from the NASA F100 full-scale engine research program [Chi84]. At the end of Phase II testing, 12 blades were fitted with new strain-gages and substituted back into the first-stage fan rotor in order to begin Phase III testing. The average blade frequency increased from 1098 Hz to 1107 Hz, a small but generally stabilizing change. However, the flutter boundaries decreased dramatically for both inlet pressures (13.8 and 17.2N/cm^2). Here the engine operates along the "normal operating line" of Figure 1.4; as the throttle is opened one moves left along this line. The flutter boundaries shown denote when stability is lost along this operating line. The above change in flutter boundaries corresponds to a 7% drop in corrected airflow. Blade mistuning was the most plausible suspect for this dramatic decrease in stability (this is contrary to most cases cited in the literature where stiffness mistuning is typically stabilizing).

Although random mistuning may lead to HCF and/or flutter, intentional mistuning can provide benefits. For example, it can push back flutter margins to allow increased performance (as noted in [Ben84, CH85, KK82, Whi64, Sha98]). Since this increase in stability is typically accompanied by a larger forced response with resulting HCF, intentional mistuning has been viewed as a tradeoff between a benefit in stability versus a detriment in forced response. It is true that introduction of any mistuning typically creates a larger

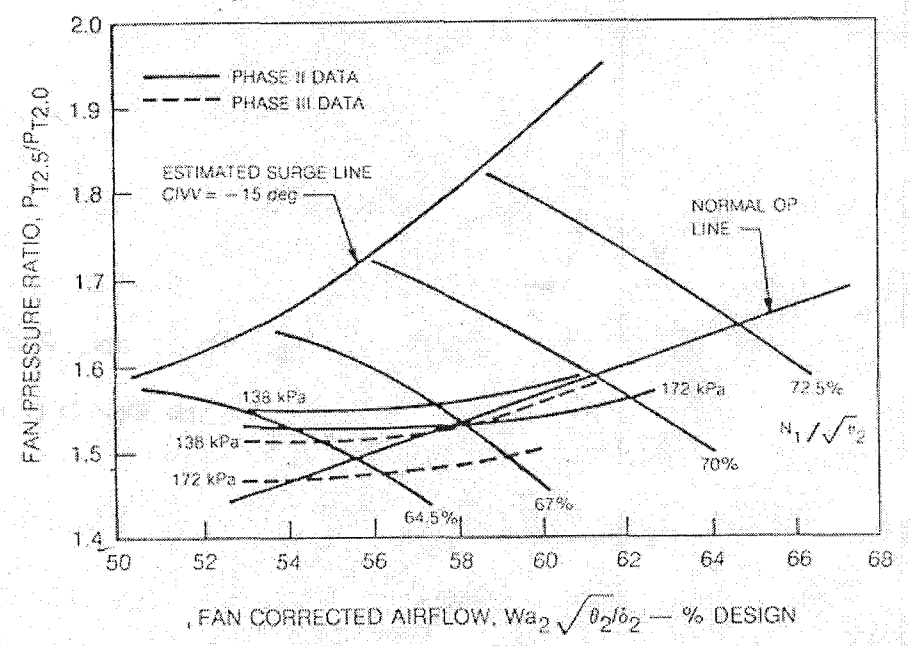

Figure 1.4: Large stability drop (apparently) caused by blade mistuning.

forced response (mistuning always creates additional resonance behaviour). However, there will always be some mistuning present (due to uncertainty, tolerances and wear) so we must compare the probable or worst case behaviour under uncertainty at the tuned point versus the probable or worst case behaviour under uncertainty at an intentionally mistuned point. If the intentional mistuning is chosen intelligently, it may lead to improved robust behaviour. In Section 5.2.2 we show a case where the tuned system is not robust: small manufacturing tolerances can lead to disastrous forced response and even instability. Upon introduction of intentional mistuning, the system becomes robust: now acceptable forced response and stability are guaranteed under the same manufacturing tolerances. Clearly, the latter situation is preferable to the former. Consequently, intentional mistuning (if done properly) might answer the challenge posed by the Air Force Scientific Advisory Board (AFSAB) [SAB92] to prevent fatigue failure through better management of vibratory stresses. It is the opinion of the AFSAB that this task cannot be accomplished through improving resistance of materials to vibratory stresses (except perhaps through composites) or by improved non destructive evaluations. We feel that intentional mistuning is one of the more practical alternatives—

it makes use of existing technology and does not require new materials or manufacturing techniques.

To this end, we must understand the effect of mistuning on stability and forced response. It is impossible to do so experimentally as even with just two different blade types the number of combinations grows as 2^r where r is the number of blades. Consequently, our approach must be analytic. Moreover, it must not only predict behaviour for a given mistuning, but it should reveal underlying design tradeoffs to facilitate improved engine design. Figure 1.5 shows our analysis goal. At the top of the figure we find a first cut approach: take an engine model $\dot{x} = f(x, z, t)$ and plug in mistuning z to find response X and stability extension s. Such an approach is not useful for two reasons: a) it is computationally intractable (to map out the mistuning space we have to run the possibly complex model f on the order of 2^r times) and b) it provides no insight. By comparison, the approach at the bottom of Figure 1.5 takes model $\dot{x} = f(x, z, t)$ as its input and generates the functionals $X(z)$ and $s(z)$ as output. Now we have an (ideally simple) expression for stability and forced response as a function of mistuning z. From expressions $X(z)$ and $s(z)$ we can learn sensitivities and design tradeoffs. Instead of iterating on mistuning, we can iterate on models. Computation complexity has been vanquished and since the method is model independent we can gain invaluable understanding on how sensitivity to mistuning varies with parameters and between models. This thesis presents the analysis arrow and *achieves* the analysis goal at the bottom of Figure 1.5, providing simple accurate functionals $X(z)$ and $s(z)$ that reveal underlying design tradeoffs. This is done by perturbing eigenvalues and eigenvectors about the tuned point to provide the functional approximation, exploiting system symmetry at every step.

By comparison, previous work [KK82, PM92] varies between the top and middle of Figure 1.5. It is not difficult to justify this statement: there are a number of problems considered intractable in the literature which are straightforward in our framework. For example, the combinatoric optimization problem of arranging mistuned blades to maximize stability is claimed intractable in the literature [Wat93] but is solved closed form in Section 5.1.2 (albeit in a practical special case). Robustness guarantees under manufacturing tolerances cannot be achieved using current methods in the literature but are given here in Section 5.2.2. In [WP90], Monte Carlo simulations are performed on a specific model to check probability of

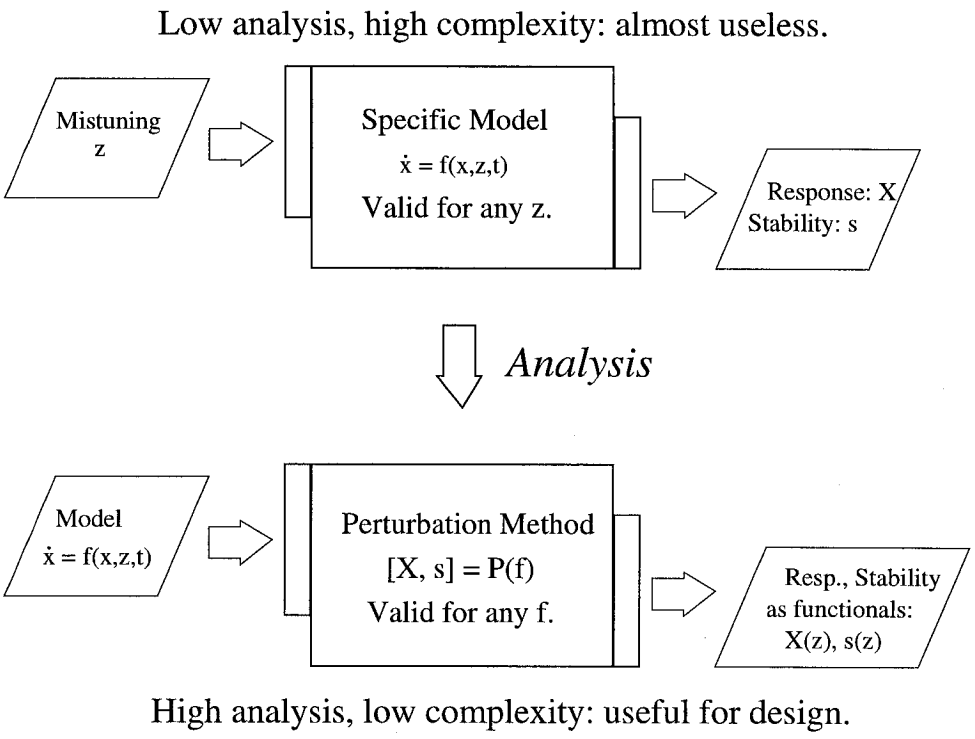

Figure 1.5: Developing a method valid for any model.

unacceptable forced response (precisely the top approach of Figure 1.5). This approach is justified by the claim that all analytic methods (such as [Sin86]) fail when the system is lightly damped. This is not so. At worst, Monte Carlo simulation can be performed orders of magnitude more efficiently on our functional relation $X(z)$ of equations (4.92), (4.94) and (4.69). At best, these equations will be amenable to analytic estimates of probabilities—certainly we can guarantee a zero probability in some cases by the bounds of Section 5.2.2.

Both the analysis and optimization of mistuning has been addressed in past research, with focus on issues of stability and forced response. Dugundi and Bundas [DB84] use Whitehead's aerodynamic coefficients [Whi60] to predict the stability increase for alternate blade mistuning. Bloemhof [Blo87] considers stability increases due to single, double and triple blade alternate mistuning along with aperiodic or random mistuning. Most work on the "side effects" of mistuning has focused on forced response. Papers in this area include [DB84, KK82, PD87, PM92, Whi66]. Work on related "side effects" such as decreased operating range can be found in Srinivasan and Frye [SF76]. In terms of optimization, efficient solutions to the stability optimization issue do not exist in the literature because

there are no efficient solutions of the analysis problem for *arbitrary* mistuning. Crawley, Hall [CH85] and Nissim, Haftka [NH85] tackle an optimization problem where they minimize the size of mistuning (implicitly assuming that resulting "side effects" are also minimized) subject to a required stability increase. Even though this is a reasonable approach, we note that in both papers only local optimums are found and both methods are restricted to small problems (less then 14 blades) by lengthy computation times. For the same reason there are no forced response optimization results (solving the stability problem is a prerequisite for a forced response solution). As a result, robustness questions for stability and forced response are beyond the scope of tools found in the literature.

In addition, even though mistuning is concerned primarily with symmetry and symmetry breaking, previous mistuning work has not made use of symmetry arguments to aid in the analysis. Yet it has been recognized in the dynamics literature that symmetry tools can provide valuable information about system behaviour. This dynamics literature includes an analysis of bifurcation behaviour [GS80], and periodic orbit dynamics [GL97], under symmetry and symmetry breaking. The large scope and depth of symmetry breaking research is discussed in some broad review articles and books; [Lau96], [GSS88] and [Chi91]. Since the subject of nonlinear dynamics, periodic orbits and bifurcations is inherently highly mathematical; the results presented are technically intricate and there remain many important open questions. In this thesis we focus on a linear problem (linear in the state vector, not in the mistuning), hence the results derived by symmetry arguments are much stronger and provide a great deal of information about mistuning behaviour not available in current mistuning literature.

Moreover, various perturbation schemes found in the mistuning literature have severe drawbacks. The work in [PM92] treats both blade coupling ϵ and the mistuning vector z as perturbation parameters. At $\epsilon = 0, z = 0$ all eigenvalues collapse to the single blade modes. From this the authors conclude that the eigenvalue motion will be discontinuous (which is false since the eigenvalues are simple) and so a perturbation about $z = 0$ is not used. Instead, the authors perturb about $\epsilon = 0, z \neq 0$ which is clearly undesirable—it is not possible to see past the $z = 0$ singularity. Meanwhile, Sinha [Sin86] and others use a series expansion to invert almost singular matrices. Their method fails as conditions approach lightly-damped

resonance—the case of interest. In contrast, the work of Mignolet and Hu [MH97] is valid over a wide range of mistuning z because it matches a series perturbation valid for very small mistuning with a coupling ϵ perturbation valid over large mistuning. However, this work only provides statistical information (what are the probabilities of instability and unacceptable forced response) and is not useful for intentional mistuning design.

There do exist some careful experimental results [KP97, LWS93, MM88, SF76, SC85]. Unfortunately, because of the explosive growth of pattern combinations with the number of blades, these experiments provide high-fidelity but limited information. By providing a unified mistuning framework, this thesis circumvents the pitfalls mentioned above. General tools are derived for mistuning analysis and optimization. There are two basic threads in this thesis; 1) symmetry arguments and 2) an approximation via eigenvalue/vector perturbation. It is shown in Chapter 3 that symmetry greatly constrains the allowable mistuning behaviour. Hence symmetry results are derived for all aspects of the mistuning problem including initial model formulation, equilibrium points, eigenvalues and eigenvectors. The symmetry arguments presented also allow for simplification of the optimization problem; as in Chapter 5. The eigenvalue/vector perturbation scheme is discussed in Chapter 4. By approximating eigenvalues and eigenvectors (while exploiting symmetry) we can capture the strong nonlinear mistuning dependence for lightly-damped bladed-disks. This perturbation method also allows the phrasing of tractable optimization problems; as in Chapter 5. Finally, results are demonstrated for a high-fidelity low-order model derived from computational fluid dynamic (CFD) data; see Chapter 6. Most importantly, the tools in this thesis provide an intuitive understanding of the mistuning problem: its sensitivities, tradeoffs and possible solutions.

Selected Nomenclature

α^* = beneficial mistuning crossover, defined in (5.4) and Figure 5.1.

a = linear stability coefficient, see (4.16), (4.17) and (4.38).

A = $A(z) = [i\omega I - M(z)]$, used in (4.5).

b = diagonal quadratic stability coefficient, see (4.16), (4.17) and (4.39).

c_i = ith off-diagonal quadratic stability coefficient, see (4.16), (4.17) and (4.40).

B_ℓ = ℓth forcing vector, see (3.18).

β = $\beta(z)$, first m elements or first block of $B_\ell(z)$, see (4.66).

f = $(f_1, f_2, \ldots, f_r)$ cascade model (3.1), f_j dynamics of jth blade.

$\bar{f}$ = $\bar{f}(x, z)$ unforced system in (4.1).

f' = $f'(x, z, t)$ forced dynamics, see (4.1).

k = $r/2$ when r even, $(r-1)/2$ when r odd, see (4.79).

ℓ = spatial mode index in fixed frame, see (3.18).

L = $\ell \bmod r$ the tuned response mode, see (4.70).

λ_j^d = $\lambda_j^d(z)$ an eigenvalue of $M(z)$, indexing of Theorem 3.4.1.

Λ = $\Lambda(z)$ diagonal matrix of eigenvalues of $M(z)$, see (4.60).

m = number of states per blade.

M = $M(z)$ linearization of $\bar{f}$ about x^*, see (3.12).

$\bar{M}$ = $M(0)$ tuned circulant matrix with blocks $\bar{M}_j$, see (3.15).

μ_j^d = $\mu_j^d(z)$ an eigenvalue of $A^{-1}(z)$, indexing of Theorem 3.4.1.

n = rm, total number of states.

ω = $\ell\Omega$ forcing frequency for ℓth mode, defined below (3.18).

Ω = cascade angular velocity, Figure 3.1.

ϕ, ψ_i = $\phi_{j,d}, \psi_i^{j,d}$, quadratic eigenvalue perturbation coefficients of (4.78).

Φ = $\Phi_{j,d}$, quadratic eigenvalue perturbation matrix, defined above (4.79).

p_j = $e^{2\pi ij/r}$, jth phase coefficient, see Theorem 3.4.1.

Q_j = $\bar{M}_1 + p_j\bar{M}_2 + p_j^2\bar{M}_3 + \cdots + p_j^{r-1}\bar{M}_r$, jth block in Theorem 3.4.1.

r = number of blades.

σ = $\sigma_{j,d}$, linear eigenvalue perturbation coefficient of (4.78).

s = $s(z)$ stability extension, defined in (4.10).

S = stability extension matrix, see (4.17).

T, T^{-1} = $T(z), T^{-1}(z)$ matrix of right, left eigenvectors of $M(z)$, see (4.60).

t = time.

τ = $2\pi/r\Omega$ system symmetry time lag, equation (3.5).

U = loading.

u_j^d = $u_j^d(z)$, first m elements or block of $U_j^d(z)$, see (4.66).

U_j^d = $U_j^d(z)$ left (row) eigenvector of $M(z)$, in indexing of Theorem 3.4.1.

v_j^d = $v_j^d(z)$, first m elements or block of $V_j^d(z)$, see (4.66).

V_j^d = $V_j^d(z)$ right (column) eigenvector of $M(z)$, in indexing of Theorem 3.4.1.

φ = rotation operator, defined in (3.4).

x = $(x_1, x_2, \ldots, x_r)$ system state, $x_j \in \mathbb{R}^m$ states for jth blade.

x^* = $x^*(z)$ equilibrium point of unforced system $\bar{f}$, see (4.1).

X = $X(z)$ forced response in frequency domain (4.5), X_j^q for jth blade, qth mode.

ξ = $\xi(\hat{x}, s, z, t)$ solutions of cascade model (3.1); for initial condition $\hat{x}$ at time $t = s$ with mistuning z.

z = $(z_1, z_2, \ldots, z_r)$ mistuning vector, $z_j \in \mathbb{R}$ mistuning of jth blade.

ζ = $\zeta(\theta)$ disturbance in stationary frame, Figure 3.1.

Chapter 2 Description of Flutter and Forced Response

Flutter is the generic name given to a wide range of instabilities caused by the coupling between aerodynamic and structural forces. Examples include vibration of Venetian blinds in breezy rooms, instabilities in power lines due to shed vorticity, divergence in aircraft wings at high speeds, instabilities in helicopter blades as they impact preceding wakes, and vibration of blades in turbomachines. These instabilities may take the form of growing oscillations (such as seen in blades or power lines), or they may take the form of a more violent breakaway behaviour (as can be encountered in airplane wings which can twist back and snap at sufficiently large airspeeds). In both divergent and oscillatory cases, flutter creates severe performance limitations. For airplanes, helicopters and turbomachines, divergent behaviour is clearly disastrous. Similarily, the vibrations caused by oscillatory flutter can create unacceptable structural forces which also lead to failure. As a result, these engineering devices must operate away from flutter boundaries (as in Figure 1.3).

Since flutter behaviour is created by aeromechanical coupling, its modeling requires both structural mechanics and aerodynamics. In the case of aircraft and turbomachines, the aerodynamic modeling is more problematic than the structural mechanics portion. In part, this is because aircraft and turbomachines operate at high Reynolds numbers and so the aerodynamic behaviour is complex and typically handled by large aerodynamic codes, while the structural mechanics (although also dealing with complex geometries) can be solved numerically and projected onto a small number of known mode shapes to provide tractable models. Mostly, the difficulty in aerodynamics stems from a better understanding of structural mechanics as compared to aerodynamics (with turbulence acting as the classic demonstration of insufficient understanding in aerodynamics).

Due to the difficulty in modeling aerodynamics and also because the primary concern has been with finding allowable operating regimes, flutter analysis has traditionally dealt with

predicting flutter boundaries. The standard linear problem is given by

$$[M]\ddot{x} + [\zeta]\dot{x} + [K]x = F \tag{2.1}$$

where M, ζ, K are the structural mass, damping and stiffness matrices, x is the structural state and F denotes the aerodynamic forces. The fundamental observation here is that on the flutter boundary the free motion is purely periodic corresponding to an eigenvalue pair on the imaginary axis. The special case of incipient divergent behaviour implies an eigenvalue at the origin, or a period of size zero. Imposing this purely periodic motion of frequency ω ($x(t) = qe^{i\omega t}$) leads to the eigenvalue problem

$$(-\omega^2[M] + i\omega[\zeta] + [K])q = f(U, \omega) \tag{2.2}$$

where U is the applied aerodynamic loading. Hence one needs to know the aerodynamic response to pure periodic motion at frequency ω with aerodynamic loading U, or $f(U, \omega)$ above. This cannot be found in general. However, for various flow conditions it can be attained analytically (say two-dimensional aerodynamic strip theory), computationally (by computational fluid dynamic codes) or experimentally (by imposing periodic motion and measuring the resulting aerodynamic forces at various frequencies) at a given set of loadings U and frequencies ω. To find the flutter boundaries one searches for U and ω which provide solutions of equation (2.2). The minimum solution U provides the flutter boundary with associated frequency of instability ω. (At this minimum U, we first find an eigenvalue $\lambda = i\omega$ on the imaginary axis.) An overview of cascade flutter analysis can be found in [For94].

This type of flutter boundary analysis is not sufficient for our aims. First, the model (2.2) only holds at the frequencies where $f(U, \omega)$ has been evaluated. As we mistune the cascade, we find that eigenvalues are moving substantially through the complex plane, including off the imaginary axis, and the knowledge at a given frequency (or discrete set of frequencies) on the imaginary axis is no longer sufficient. Moreover, the standard assumption of constant inter-blade-phase-angle (all blades vibrate with equal amplitude separated by a constant

phase) is no longer true in the mistuned case. Second, for forced response calculations it is crucial to have the correct (typically small non-zero) damping, yet equation (2.2) only holds at zero system damping. Third, model (2.2) has the form: $\dot{y} = A(\omega)y$ where the linear dynamics depend on the state y through its frequency ω. As such, this model is not amenable to standard linear dynamics and control tools (stability, robustness, eigenvalue/vector motion with parameters). Hence there is a need for models that do not impose periodic motion.

A simple dynamical flutter model with no imposed motion is shown in Figure 2.1. Here

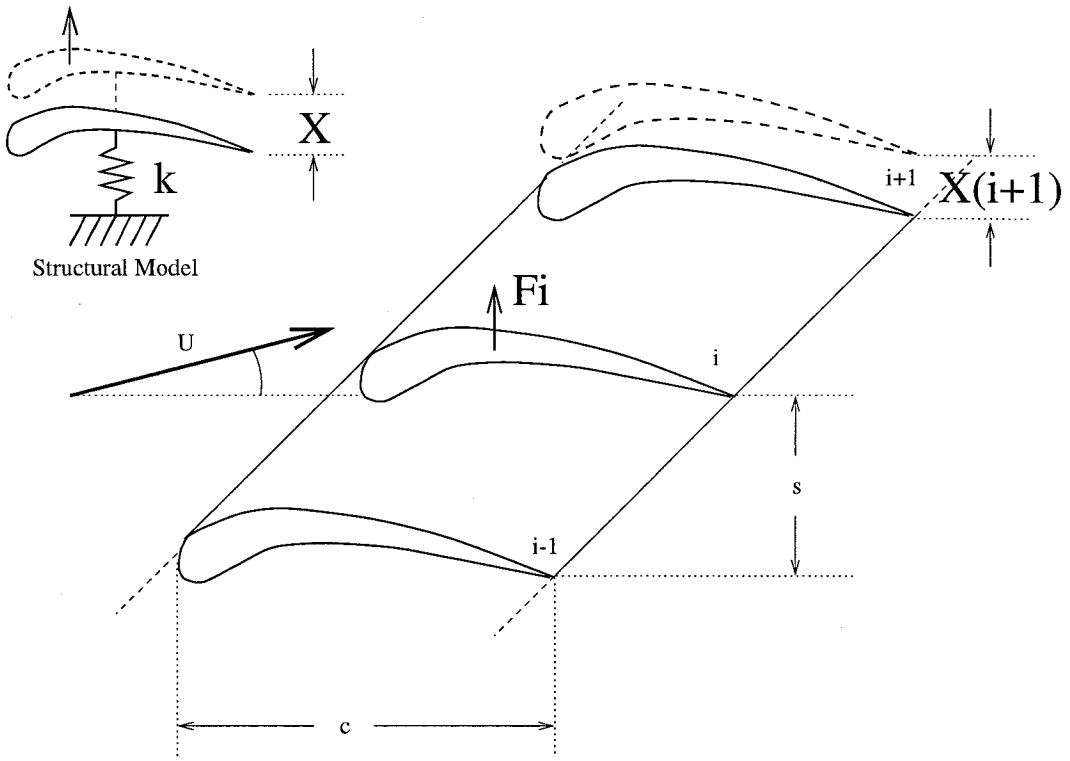

Figure 2.1: Simplest cascade flutter model.

the jth blade displacement is given by x_j. The structural model is given by a simple mass-spring system

$$m\ddot{x}_j + kx_j = \alpha U\dot{x}_j + \beta U^2[x_{j+1} - x_{j-1}] \tag{2.3}$$

and the aerodynamic force is taken to be $F_j = \alpha U\dot{x}_j + \beta U^2[x_{j+1} - x_{j-1}]$. The $\alpha U\dot{x}_j$ term corresponds to steady aerodynamic damping due to blade velocity $\dot{x}_j$. The blade coupling $\beta U^2[x_{j+1} - x_{j-1}]$ captures the physical intuition that blade j must turn the quantity of air

between blades $j+1$ and $j-1$. This intuition is surprisingly accurate; when model (2.3) is compared against the quasi-steady model of Section 4.6, it is found that F_j captures the leading order (quasi-steady) dynamics. This is one of the simplest cascade models that will display instability as loading U increases.

Of course, the usefulness of a simple model such as (2.3) is limited. One can construct more advanced models by including more phenomenological effects. As more effects are included the model complexity and cost of computation increases. An alternate approach is to take high-fidelity computational fluid dynamic (CFD) models (such as Euler or Navier Stokes solvers) and to reduce the dynamics to provide a tractable low-order model. This is the approach taken by Willcox et al. [WPP99]. They perform principle orthogonal decomposition on data from a CFD code to provide low-order aerodynamic models valid for any motion and amenable to mistuning analysis. Mistuning results using their model are presented in Chapter 6.

Issues in forced response are essentially the same. The extension required is the addition of outside excitation (typically aerodynamic, but possibly mechanical as in a shaft imbalance) in equation (2.1). This yields the linear problem

$$[M]\ddot{x} + [\zeta]\dot{x} + [K]x = F + Ge^{iw_f t} \tag{2.4}$$

where $Ge^{iw_f t}$ is the external periodic forcing. Once again the difficulty is in analyzing the aerodynamics (find F and G in terms of structural states x). Choice one is to assume $x(t) = qe^{iw_f t}$ and find $F = F(U, w_f), G = G(U, w_f)$ for a discrete set of loadings U and forcing frequencies w_f. This is the classical approach which provides limited information; one must search over prohibitively many U, w_f pairs to provide a complete model. For example, it is not sufficient to search along the flutter boundary of equation (2.1) because the Fs found in that case correspond to a system with zero damping and this system will exhibit infinite amplitude when forced at resonance. The second choice is to develop a finite approximation for F and G in terms of aerodynamic states y to yield the closed set of

equations

$$[M]\ddot{x} + [\zeta]\dot{x} + [K]x = F(U,y) + G(U,y)e^{iw_f t} \tag{2.5}$$

$$\dot{y} = A(U)y + B(u)x + C(U)e^{iw_f t}. \tag{2.6}$$

This is the approach in [WPP99] and it allows the inclusion of forced response.

To get an understanding of how mistuning affects flutter boundaries, it is possible to proceed quite a distance without writing down any specific flutter model. The mathematics in this thesis is aimed at that goal, we only write down models when they become necessary. There exist many intuitive explanations of mistuning to match the mathematics. On the most general level, bladed disks operate in high-energy environments (large aerodynamic loads, fast rotation speeds, high Mach numbers) and so instabilities can be created or destroyed by even a small change in how much energy is being transfered between the structure and the fluid. It is also true that flutter typically manifests as traveling waves rotating around the disk. A small nonuniform change in blade properties serves to interrupt the progress of the instability around the disk. Equivalently, different disk modes have different dampings. One of these modes goes unstable first. Mistuning couples the modes together and can delay the instability of the least stable mode by mixing it with higher damped modes. From a rigorous mathematical standpoint, we find that mistuning flutter sensitivity can be caused by small blade coupling which creates nearby eigenvalues and causes fast eigenvalue motion, or by a slow change in minimum damping with loading U which means even a small change in eigenvalues results in a big change in operating range.

Forced response sensitivity is caused by the breaking of eigenvector symmetry. When the system is tuned, all the eigenvectors (tuned mode shapes) are symmetric. This means that a mode three forcing will only excite the third tuned mode shape. Once mistuning occurs the eigenvectors lose symmetry and so a third nodal diameter forcing can excite all modes. Hence mistuning creates additional resonances. The amount of additional response depends on the forcing frequency (the distance from resonance) and the damping (this is why it is crucial to have models that correctly predict damping). Since bladed-disks are typically lightly-damped, the resonance caused by mistuning is severe. Intentional mistuning can be used to

provide robust damping—as in the flutter case mistuning can shift eigenvalues to the left significantly. As a result, the tuned, lightly-damped, sensitive case (small random mistuning creates large response) can be replaced by the robust, significantly-damped, mistuned case (additional small random mistuning does not destroy the increased damping and response remains acceptable).

Chapter 3 Application of Symmetry Tools

Mistuning is fundamentally concerned with symmetry and symmetry breaking. As a result, the symmetry arguments presented in this section are the natural tools of analysis. Basically, these arguments formalize the obvious statement

> *Given a tuned system, mistuning blade one and observing blade two is the same as mistuning blade three and observing blade four.*

Being natural, these arguments provide both powerful and general results.

In terms of generality, symmetry arguments apply to *any* bladed disc model. In our formulation these arguments are applied to any dynamic discrete blade cascade model of the form $\dot{x} = f(x, z, t)$. As a special case, they hold for imposed sinusoidal motion models where the dynamics are restricted to $x(t) = \bar{x} + x'e^{iwt}$ (these models are widely seen in the aerodynamics literature [Whi66, KK82, Blo87, Chi85, CS85]). Extensions to other types of dynamic models (such as the actuator disc model found in Gysling and Myers [GM96]) are clear. Moreover, conclusions achieved by symmetry considerations apply even when $f(x, z, t)$ cannot be written explicitly as is the case in commonly used computational-fluid-dynamic (CFD) models.

In terms of power, the scope of symmetry arguments is demonstrated below. Still, it is revealing to mention one result before embarking on our analysis. Mistuning has a reputation as a difficult problem primarily due to computational complexity. Even if we have only two blade types, the number of mistuning patterns grows as 2^r where r is the number of blades. This has led to the notion that it is not possible to find global optimals for combinatoric mistuning optimization problems. For example, the combinatoric optimization problem of arranging a given set of mistuned blades to maximize stability is claimed intractable in the literature [Wat93]. However, in Section 5.1.2 we show how a practical special case may be solved analytically by symmetry exploitation. Hence symmetry arguments can be used to dramatically reduce problem difficulty.

Our mistuning problem has two components. Component one deals with system stability and performance range extension (Section 4.2), component two deals with forced response and resulting high-cycle-fatigue (Section 4.3). In terms of symmetry arguments, component one (stability) turns out to be a special case of component two (forced response). As a result, we start with symmetry arguments for the time-varying system (3.1) below, which is aimed at forced response, and then specialize our discussion to time-invariant unforced systems (3.10), aimed towards stability, at a later point.

3.1 Discrete Blade Model Symmetry

Suppose our fan or compressor has r blades. Consider any discrete blade model of the form

$$\dot{x} = f(x, z, t) \tag{3.1}$$

where $x = (x_1, x_2, \ldots, x_r) \in \mathbb{R}^{rm}$ is the state vector with $x_i \in \mathbb{R}^m$ corresponding to aerodynamic and structural states for the ith blade. For example, x_1 could contain the first blade position and velocity, along with all aerodynamic states associated with blade one. Mistuning is represented by the vector $z \in \mathbb{R}^r$. An element $z_i \in \mathbb{R}$ denotes mistuning for the ith blade. For example, if we mistune the stiffness of individual blades then define the ith blade stiffness $k_i = k_0(1 + z_i)$ where k_0 is the nominal or tuned stiffness. As in this example, $z = 0$ will always denote the tuned case. Finally, t represents time since we allow time dependent forcing.

Consider now the dynamics of the first blade

$$\dot{x}_1 = f_1(x_1, x_2, \ldots, x_r, z_1, z_2, \ldots, z_r, t) \tag{3.2}$$

which correspond to the first "block row" (the first m rows) of the vector field f in model (3.1). Clearly, the dynamics of the first blade ($\dot{x}_1$) depend on the state of the third blade (x_3) the same way the dynamics of the second blade ($\dot{x}_2$) depend on the state of the fourth blade (x_4). The same holds for the mistuning vector z, the dynamics of the first blade ($\dot{x}_1$) depend

on the mistuning of the seventh blade (z_7) the same way the dynamics of the third blade ($\dot{x}_3$) depend on the mistuning of the ninth blade (z_9). Applying this chain of logic to all blades we must have

$$\begin{aligned}
\dot{x}_1 &= f_1(x,z,t) = f_1(\ x_1,x_2,x_3,\ldots,x_{r-1},x_r,\ z_1,z_2,z_3,\ldots,z_{r-1},z_r,\ t) \\
\dot{x}_2 &= f_2(x,z,t) = f_1(\ x_2,x_3,\ldots,x_{r-1},x_r,x_1,\ z_2,z_3,\ldots,z_{r-1},z_r,z_1,\ t+\tfrac{2\pi}{r\Omega}) \\
\dot{x}_3 &= f_3(x,z,t) = f_1(\ x_3,x_4,\ldots,x_r,x_1,x_2,\quad z_3,z_4,\ldots,z_r,z_1,z_2,\quad t+\tfrac{4\pi}{r\Omega}) \\
&\ \ \vdots \qquad\qquad\qquad\qquad\qquad\qquad \vdots \\
\dot{x}_r &= f_r(x,z,t) = f_1(\ x_r,x_1,\ldots,x_{r-2},x_{r-1},\quad z_r,z_1,\ldots,z_{r-2},z_{r-1},\quad t+\tfrac{2\pi(r-1)}{r\Omega}).
\end{aligned} \tag{3.3}$$

The time shift of $2\pi/r\Omega$ in expression (3.3) follows from assuming a stationary disturbance, as would be generated by stator/inlet guide vane wakes or by an inlet distortion. For a cascade of undeformed blades rotating at angular velocity Ω past such a stationary disturbance (as in Figure 3.1) the disturbance at blade two will precede the same disturbance at blade one by $2\pi/r\Omega$. Now consider the case where blades are deforming due to their states x and possibly their mistuning z (for example, mistuning stiffness will change the nominal deformation of blades under aerodynamic loading). If at time t blade one is deformed from its nominal angular position θ_1 by some amount ψ due to its state ($x_1 = \alpha$) and its mistuning ($z_1 = \beta$), then it occupies the position $\theta_1 + \psi(\alpha,\beta)$ and has some shape deformation $\zeta(\alpha,\beta)$. It follows that if blade two has the same state ($x_2 = \alpha$) and mistuning ($z_2 = \beta$) at time $t + 2\pi/r\Omega$ then it must deform an identical amount and will also occupy the position $\theta_1 + \psi(\alpha,\beta)$ with the same shape $\zeta(\alpha,\beta)$. At these two identical conditions (same position and shape) blade one and blade two will experience the same dynamics due to forcing. This is precisely the statement in (3.3), $\dot{x}_1$ depends on x_1, z_1 and t the same way $\dot{x}_2$ depends on x_2, z_2 and $t + 2\pi/r\Omega$.

To ease notation we define the rotation operator φ which rotates vectors of size m or rm to the left. The scope of the argument (size r or rm) is clear from context,

$$\begin{aligned}
\varphi^j[z_1,z_2,\ldots,z_r] &= [z_{1+j},z_{2+j},\ldots,z_r,z_1,\ldots,z_j], \qquad z_i \in \mathbb{R} \text{ or } \mathbb{C} \\
\varphi^j[x_1,x_2,\ldots,x_r] &= [x_{1+j},x_{2+j},\ldots,x_r,x_1,\ldots,x_j], \qquad x_i \in \mathbb{R}^m \text{ or } \mathbb{C}^m.
\end{aligned} \tag{3.4}$$

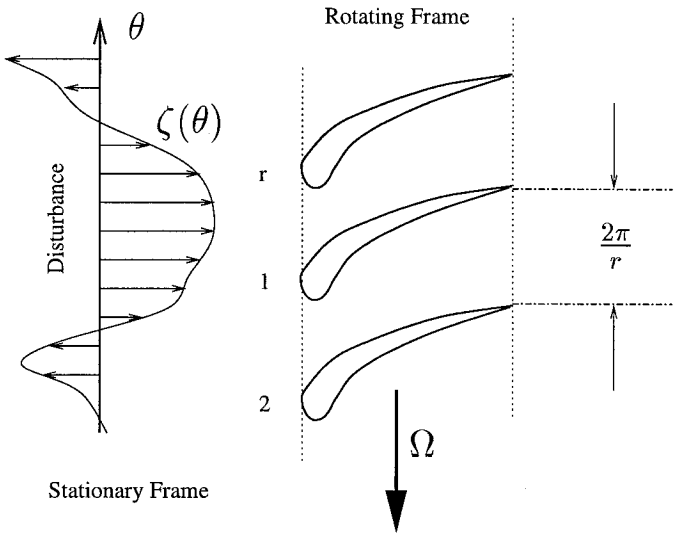

Figure 3.1: Cascade disturbance.

For convenience, φ^1 is written simply as φ and φ^{-1} is the inverse rotation to the right. Using the rotation operator and defining $\tau = 2\pi/r\Omega$, condition (3.3) on model (3.1) can be rewritten succinctly as

$$\varphi f(x, z, t) = f(\varphi x, \varphi z, t + \tau). \tag{3.5}$$

Applying (3.5) a total of r times we note $f(x, z, t) = f(x, z, t + 2\pi/\Omega)$ which is of course the periodicity associated with a complete rotation.

Expression (3.5) is a *system symmetry* and is the basic building block for all the analysis that follows. It holds for linear and nonlinear systems whether they be low order models or computationally expensive CFD simulations. All parts of the mistuning problem (including questions relating to linearizations, stability, forced response or optimization) inherit a portion of this system symmetry which may be exploited to great advantage.

3.2 Trajectory Symmetry

The results below follow immediately from the system symmetry shown in (3.5). Let $\xi(\hat{x}, s, z, t)$ denote trajectories or solutions to (3.1) with initial condition $\hat{x}$ at time s where the mistuning has been fixed at z. For this initial condition $\hat{x}$ at time $t = s$ (so $x(s) =$

$\xi(\hat{x}, s, z, s) = \hat{x}$), the state of the system at any other time t is given by $x(t) = \xi(\hat{x}, s, z, t)$. It follows from (3.5) that solutions ξ must satisfy

$$\varphi\xi(\hat{x}, s, z, t) = \xi(\varphi\hat{x}, s + \tau, \varphi z, t + \tau). \tag{3.6}$$

Equation (3.6) says that if we know the solution for $\hat{x}, s$ and z, then we have also found the trajectory for initial condition $\varphi\hat{x}$ at time $s + \tau$ with mistuning φz.

Theorem 3.2.1 *For model (3.1) with symmetry (3.5) the trajectories $\xi(\hat{x}, s, z, t)$ satisfy condition (3.6).*

Proof: Let $\eta(t) = \varphi\xi(\hat{x}, s, z, t) - \xi(\varphi\hat{x}, s+\tau, \varphi z, t+\tau)$. By construction, $\eta(s) = \varphi\hat{x} - \varphi\hat{x} = 0$ and so we have

$$\begin{aligned}
\dot{\eta}(t) &= \varphi\dot{\xi}(\hat{x}, s, z, t) - \dot{\xi}(\varphi\hat{x}, s + \tau, \varphi z, t + \tau) && \text{by construction} \\
&= \varphi f(\xi(\hat{x}, s, z, t), z, t) - f(\xi(\varphi\hat{x}, s + \tau, \varphi z, t + \tau), \varphi z, t + \tau) && \text{from (3.1)} \\
&= f(\varphi\xi(\hat{x}, s, z, t), \varphi z, t + \tau) - f(\xi(\varphi\hat{x}, s + \tau, \varphi z, t + \tau), \varphi z, t + \tau) && \text{symmetry (3.5)} \\
&= f(\eta(t) + \xi(\varphi\hat{x}, s + \tau, \varphi z, t + \tau), \varphi z, t + \tau) \\
&\quad - f(\xi(\varphi\hat{x}, s + \tau, \varphi z, t + \tau), \varphi z, t + \tau) && \text{by construction} \\
&\triangleq H(\eta, t) && \text{a definition.}
\end{aligned}$$

Clearly $H(0, t) = 0$ for all t, regardless of values $\hat{x}, s$ and z. Thus $\eta(t)$ satisfies $\dot{\eta} = H(\eta, t)$, $\eta(s) = 0$ with $H(0, t) \equiv 0$ and so η starts at zero and stays zero for all time. Consequently, $\eta(t) = \varphi\xi(\hat{x}, s, z, t) - \xi(\varphi\hat{x}, s + \tau, \varphi z, t + \tau) = 0$ for all $\hat{x}, s, z$ and t. ∎

In the special case of a tuned cascade ($z = 0$ or more generally $\varphi z = z$ which is equivalent to $z_1 = z_2 = \cdots = z_r$) and no forcing (no time dependence in (3.1)) we can drop the now redundant z and t notation to reduce (3.5) to

$$f(x) = \varphi^{-1} f(\varphi x). \tag{3.7}$$

If we further pick tuned initial conditions $\varphi\hat{x} = \hat{x}$ then (3.6) becomes (s is dropped because all starting times are equivalent)

$$\varphi\xi(\hat{x}, t) = \xi(\hat{x}, t) \tag{3.8}$$

which implies $\xi_1(\hat{x}, t) = \xi_2(\hat{x}, t) = \cdots = \xi_r(\hat{x}, t)$ and the solution remains tuned for all time.

We shall find that the mistuning problem is essentially linear, hence we will exploit a special case of (3.5) and (3.6). Nevertheless, it is instructive to note the scope of symmetry arguments which provide results for the full nonlinear system (3.1).

3.3 Unforced Dynamics and Equilibrium Symmetry

We are concerned with the stability and forced response of bladed disks. Both stability and forced response are considered about an equilibrium point of the unforced system. Consequently, we split the forced nonlinear system (3.1) into an unforced $\bar{f}$ and forcing perturbation f' portion,

$$\dot{x} = f(x, z, t) = \bar{f}(x, z) + f'(x, z, t). \tag{3.9}$$

Here $\bar{f}$ is the dynamics of (3.1) if there is no disturbance and f' is defined as $f - \bar{f}$. Since the time-invariant dynamics are just a special case of equation (3.1), they must satisfy a special case of condition (3.5). Specifically, $\bar{f}$ has symmetry

$$\bar{f}(x, z) = \varphi^{-1}\bar{f}(\varphi x, \varphi z). \tag{3.10}$$

Symmetry (3.10) will drastically restrict the behaviour of equilibrium points.

Consider any equilibrium point $x^*(z)$ of the unforced system, $\bar{f}(x^*(z), z) = 0$. (It is crucial to note that in practice x^* can vary with mistuning. For instance, a change in stiffness will cause different nominal deformations in blades due to aerodynamic loading.) First we consider equilibrium points $x^*(0)$ of the tuned unforced system $\bar{f}(x, 0)$, the following result is standard (see [GSS88]).

Lemma 3.3.1 *Given the tuned unforced system $\bar{f}(x,0)$ with symmetry $\varphi\bar{f}(x,0) = \bar{f}(\varphi x,0)$, consider any equilibrium point $x^*(0)$. Then $\varphi^j x^*(0)$ for $j \in (1,2,\ldots,r)$ are also equilibria of $\bar{f}(x,0)$. If $x^*(0) = \varphi x^*(0)$ then this family of equilibria collapses to a single equilibrium.*

Proof: By symmetry and since x^* is an equilibrium of $\bar{f}$,

$$\bar{f}(\varphi^j x^*(0),0) = \varphi^j \bar{f}(x^*(0),0) = 0.$$

Hence $\varphi^j x^*(0)$ form a total of r equilibrium points. If $x^*(0) = \varphi x^*(0)$ they are all equal. ∎

Note that symmetry on the tuned unforced system $\varphi\bar{f}(x,0) = \bar{f}(\varphi x,0)$ does not imply a symmetric equilibrium point $x^*(0) = \varphi x^*(0)$, as in the example below:

Example 3.3.1 *Consider the tuned unforced system (no z or t dependence)*

$$\begin{aligned}\dot{x}_1 &= f_1(x_1,x_2) = x_1 - x_2 + 3x_1x_2 - 2x_1^2 - x_2^2 + 6\\ \dot{x}_2 &= f_1(x_2,x_1) = x_2 - x_1 + 3x_1x_2 - 2x_2^2 - x_1^2 + 6\end{aligned}$$

which satisfies the tuned symmetry condition $\varphi f(x) = f(\varphi x)$. There are no symmetric equilibria x^* of the form $x_1^* = x_2^*$ because

$$f_1(x_1^*,x_1^*) = x_1^* - x_1^* - 3x_1^{*2} - 2x_1^{*2} - x_1^{*2} + 6 = 6 \neq 0$$

and so $x^* = (x_1^*,x_1^*)$ cannot satisfy $f(x^*) = 0$. However, there do exist asymmetric equilibrium points and

$$\begin{aligned}f_1(2,0) &= 2 - 0 + 3*0 - 2*2^2 - 0 + 6 = 0\\ f_1(0,2) &= 0 - 2 + 3*0 - 2*0 - 2^2 + 6 = 0\end{aligned}$$

so $f(2,0) = f(0,2) = 0$ and hence $x^* = (2,0)$ and $x^* = (0,2)$ are both equilibria. So $f(x) = 0$ has no symmetric solutions, but it does have two asymmetric equilibria.

In a rough sense, this example is degenerate as illustrated in Figure 3.2. For a two-

dimensional tuned system $\dot{x}_1 = f_1(x_1, x_2), \dot{x}_2 = f_1(x_2, x_1)$ *the equilibrium points* x^* *satisfy* $f_1(x_1^*, x_2^*) = f_1(x_2^*, x_1^*) = 0$. *In the left portion of Figure 3.2 we note the curve* $f_1(x_1, x_2) = 0$ *and its reflection about the* $x_1 = x_2$ *line* $f_1(x_2, x_1) = 0$. *Since there is only one* $f_1(x_1, x_2) = 0$ *curve, any intersection (an equilibrium point) with* $f_1(x_2, x_1) = 0$ *must occur along* $x_1 = x_2$ *and all equilibria are symmetric—the "generic" case. In the right portion of Figure 3.2 there are two curves that satisfy* $f_1(x_1, x_2) = 0$, *neither one of which intersects* $x_1 = x_2$. *Now the reflection of curve two can intersect curve one and the reflection of curve one can intersect curve two. This yields two asymmetric equilibrium points which are reflections of one another. So to have only asymmetric equilibrium points in this two-dimensional system we must have a nonlinear* f *with at least two solution curves that do not intersect the 45 degree line* $x_1 = x_2$ *—the "degenerate" case as in Example 3.3.1. It is possible that families of asymmetric equilibria (as in Example 3.3.1) are degenerate in some appropriate way, but this would be hard to show rigorously for arbitrary nonlinear systems.* ■

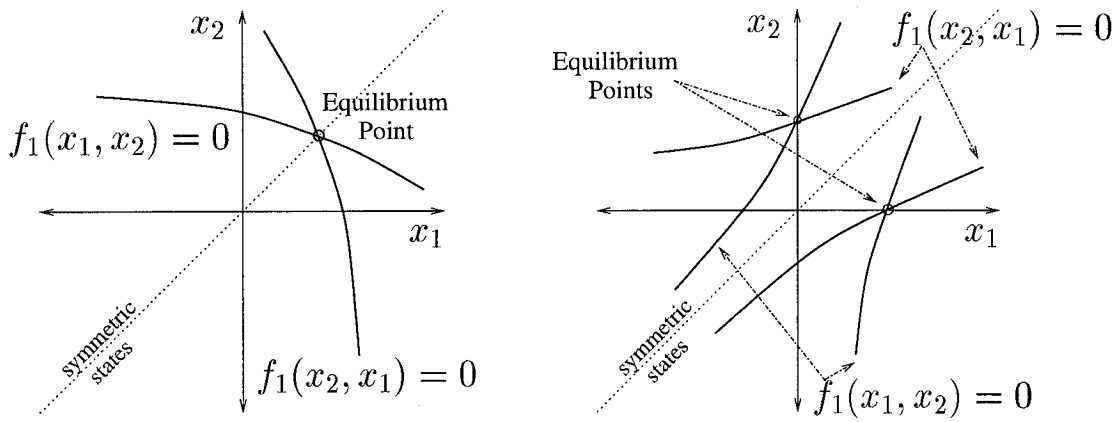

Figure 3.2: Symmetric equilibrium vs asymmetric equilibria.

Thus there are two possible cases: either there is a symmetric equilibrium $x^*(0) = \varphi x^*(0)$ or there is a family of asymmetric equilibria $x^*(0), \varphi x^*(0), \varphi^2 x^*(0), \cdots, \varphi^{r-1} x^*(0)$. Typically, families of equilibria are not observed in jet engines and so we only consider symmetric tuned equilibrium points $x^*(0) = \varphi x^*(0)$.

A mistuned equilibrium symmetry follows generically: $\varphi x^*(z) = x^*(\varphi z)$.

Lemma 3.3.2 *Consider the unforced system* $\dot{x} = \bar{f}(x, z)$, *see (4.1), with symmetry*

$$\varphi \bar{f}(x, z) = \bar{f}(\varphi x, \varphi z)$$

and equilibrium point $x^*(z)$. *If the tuned equilibrium point is symmetric* $x^*(0) = \varphi x^*(0)$ *and the Jacobian at* $x^*(0)$ *is non-singular*

$$\det \left[\frac{\partial \bar{f}}{\partial x}(x^*(0), 0) \right] \neq 0$$

(true almost always), then the equilibrium has symmetry $\varphi x^*(z) = x^*(\varphi z)$.

Proof: Let $\eta(z) = x^*(z) - x^*(0)$. Since $x^*(z)$ is an equilibrium point that varies as z changes, it satisfies $\bar{f}(x^*(z), z) = 0$ for any z, specifically

$$\bar{f}(x^*(z), z) = \bar{f}(x^*(\varphi z), \varphi z) = 0.$$

By symmetry $\varphi \bar{f}(x, z) = \bar{f}(\varphi x, \varphi z)$ of the unforced system, we have

$$\bar{f}(x^*(z), z) = \varphi \bar{f}(\varphi^{-1} x^*(\varphi z), z) = 0.$$

Substituting η and noting assumption $\varphi^{-1} x^*(0) = x^*(0)$ yields

$$\bar{f}(x^*(0) + \eta(z), z) = \varphi \bar{f}(x^*(0) + \varphi^{-1} \eta(\varphi z), z) = 0.$$

Since $\det \left[\frac{\partial \bar{f}}{\partial x}(x^*(0), 0) \right] \neq 0$ the implicit function theorem [PM77, p.354] implies that relation $\bar{f}(x^*(0) + \alpha(z), z) = 0$ uniquely defines $\alpha(z)$ locally. (Note that $\varphi \bar{f} = 0$ implies $\bar{f} = 0$.) Hence $\eta(z) = \varphi^{-1} \eta(\varphi z)$ and so

$$\varphi x^*(z) = x^*(0) + \varphi \eta(z) = x^*(0) + \eta(\varphi z) = x^*(\varphi z)$$

which is the required relation. ∎

The proof above requires that $\bar{f}(x,z) = 0$ uniquely define x as a function of z in a neighbourhood of $(x^*(0),0)$, hence the use of the implicit function theorem. So for $\varphi x^*(z) = x^*(\varphi z)$ to fail requires the degenerate case where $\bar{f}(x,z) = 0$ has multiple equilibria branching from$(x^*(0),0)$. We used the implicit function theorem to show that (generically) this is not the case in a neighbourhood of $x^*(0)$. Note that $\varphi x^*(z) = x^*(\varphi z)$ allows the equilibrium point x^* to lose symmetry as we introduce mistuning so in general $\varphi x^*(z) \neq x^*(z)$ when $z \neq 0$. Due to the arguments above, we shall assume a $\varphi x^*(z) = x^*(\varphi z)$ equilibrium symmetry in the remainder.

3.4 Unforced Linear Symmetry

We now turn to the symmetry of linear systems. Specifically, the section below deals with symmetries related to the unforced linear stability problem while Section 3.5 studies the symmetry of forced linear systems. Stability about the equilibrium point $x^*(z)$ of Section 3.3 is found by computing the eigenvalues of the linearization

$$\dot{x} = M(z)x \tag{3.11}$$

where

$$M(z) \triangleq \left[\frac{\partial \bar{f}}{\partial x}(x^*(z),z)\right] \tag{3.12}$$

and we have made the change of variables $x - x^*(z) \mapsto x$ in (3.11).

From the definition we find that M has symmetry

$$\varphi M(z) = M(\varphi z)\varphi \tag{3.13}$$

which is to be interpreted as follows: for any vector x

$$\varphi\,[M(z)x] = M(\varphi z)[\varphi x] \tag{3.14}$$

and so φ only acts on vectors as defined in (3.4).

Lemma 3.4.1 *Given unforced system $\bar{f}$ with symmetry $\bar{f}(x,z) = \varphi^{-1}\bar{f}(\varphi x, \varphi z)$ and equilibrium point x^* with symmetry $x^*(z) = \varphi^{-1}x^*(\varphi z)$, then $M(z)$ defined in (3.12) has symmetry $M(z) = \varphi^{-1}M(\varphi z)\varphi$.*

Proof: By definition of the equilibrium point x^*, $\bar{f}(x^*(z), z) = 0$. Hence a Taylor expansion yields

$$\bar{f}(x,z) = [M(z)](x - x^*(z)) + O(\|x - x^*(z)\|^2).$$

Applying symmetry of $\bar{f}$ to the linear term provides

$$\begin{aligned} \varphi\bar{f}(x,z) &= \bar{f}(\varphi x, \varphi z) \\ \Rightarrow \varphi\{[M(z)](x - x^*(z))\} &= [M(\varphi z)](\varphi x - x^*(\varphi z)). \end{aligned}$$

The crucial step is the equilibrium symmetry $\varphi x^*(z) = x^*(\varphi z)$ which allows

$$\varphi\{[M(z)](x - x^*(z))\} = [M(\varphi z)]\varphi(x - x^*(z)).$$

So for any $y = x - x^*(z)$ we have $M(z)y = \varphi^{-1}M(\varphi z)\varphi y$, the required symmetry. ∎

If we now let $z = 0$ we find that $M(0)$ must satisfy $M(0) = \varphi^{-1}M(0)\varphi$ and so it follows that the tuned linearization $M(0)$ must be block circular. Precisely, $\bar{M} = M(0)$ must have the form

$$\bar{M} = \begin{bmatrix} \bar{M}_1 & \bar{M}_2 & \bar{M}_3 & \dots & \bar{M}_{r-1} & \bar{M}_r \\ \bar{M}_r & \bar{M}_1 & \bar{M}_2 & \bar{M}_3 & \dots & \bar{M}_{r-1} \\ & \ddots & & \ddots & & \\ & & \ddots & & \ddots & \\ \bar{M}_2 & \bar{M}_3 & \dots & \bar{M}_{r-1} & \bar{M}_r & \bar{M}_1 \end{bmatrix}, \tag{3.15}$$

where $\bar{M}_j \in \mathbb{R}^{m\times m}$.

Structure (3.15) motivates Theorem 3.4.1 which is crucial in both analysis and computation. Let $p_j = \exp(2\pi ij/r)$ denote powers of the rth root of unity where $i = \sqrt{-1}$ and define

$$Q_j = \bar{M}_1 + p_j\bar{M}_2 + p_j^2\bar{M}_3 + \cdots + p_j^{r-1}\bar{M}_r \in \mathbb{C}^{m\times m}, \quad j \in (1, 2, \ldots, r). \tag{3.16}$$

Theorem 3.4.1 *For $\bar{M}$ a block circular matrix as in (3.15), let λ_j^d, u_j^d and v_j^d be the dth eigenvalue, left eigenvector and right eigenvector, respectively, of Q_j. Then λ_j^d form the eigenvalues of $\bar{M}$ with left and right eigenvectors $U_j^d = [u_j^d, p_j^{r-1}u_j^d, p_j^{r-2}u_j^d, \ldots, p_j u_j^d]$ and $V_j^d = [v_j^d, p_j v_j^d, \ldots, p_j^{r-2}v_j^d, p_j^{r-1}v_j^d]$.*

Proof: To prove the theorem we need only show $\bar{M}V_j^d = \lambda_j^d V_j^d$ and $U_j^d\bar{M} = \lambda_j^d U_j^d$. Both statements are verified by substitution. ∎

The above theorem also proves the constant inter-blade phase-angle assumption (corresponding to tuned eigenvectors above with phase angle p_j) common in flutter analysis which *only* holds when the system is tuned. In our case, Theorem 3.4.1 will be important when we begin computing eigenvalues and vectors of the tuned system in Chapter 4 because it allows us to express the eigenvalues and vectors of $\bar{M}$ as eigenvalues and vectors of Q_j's.

3.5 Forced Linear Symmetry

Below we deal with the symmetries of forced linear systems. Specifically, we analyze the system

$$\dot{x} = M(z)x + B_\ell(z)e^{i\ell\Omega t} \tag{3.17}$$

which captures forced response to leading order. Here $M(z)$ is the previously defined linearization of (3.12). Coefficient B_ℓ corresponds to the ℓth spatial mode of the disturbance in the fixed reference frame: $\zeta(\theta) = \sin(\ell\theta)$ in Figure 3.1 with resulting forcing frequency $\omega = \ell\Omega$. Transforming between the rotating and stationary frame yields a relationship

between the forcing perturbation f' in equation (3.9) and B_ℓ above

$$f'(x^*(z), z, t) = \sum_{\ell=0}^{\infty} B_\ell(z) \exp(i[\ell\Omega t + \phi_\ell]). \tag{3.18}$$

Notice that (3.18) has a complex component e^{iwt}; this is done for purposes of convenience and one can simply take the real part of the response at the close of analysis. Since we are concerned with linear systems, we can analyze each spatial mode ℓ individually.

For $M(z)$ stable, the transient response decays to zero and the steady state forced response may be written in frequency domain as

$$X(z) = [iwI - M(z)]^{-1} B_\ell(z). \tag{3.19}$$

Here steady state forced response in the time domain is given by $\bar{x}(z,t) = X(z)e^{iwt}$, while frequency w is defined as $w = \ell\Omega$. Our current concern is with resulting symmetries of X and B_ℓ. (We have already shown the linearization symmetry (3.13) of M.)

Both of the results below follow from nonlinear symmetry (3.5). The quantity p_ℓ is defined as previously: $p_\ell = \exp(2\pi i\ell/r)$.

Lemma 3.5.1 *The forcing term f' with Fourier expansion (3.18) also has symmetry (3.5), namely*

$$f'(x, z, t) = \varphi^{-1} f'(\varphi x, \varphi z, t + \tau).$$

Hence the symmetry $\varphi x^*(z) = x^*(\varphi z)$ on the equilibrium implies any vector coefficient $B_\ell(z)$ has symmetry $B_\ell(z) = p_\ell \varphi^{-1} B_\ell(\varphi z)$.

Proof: The first statement follows from symmetry (3.5). To prove the second statement, set all disturbance modes to zero except mode ℓ. Hence equation (3.18) reduces to

$$f'(x^*(z), z, t) = B_\ell(z) e^{i\ell\Omega t}. \tag{3.20}$$

By symmetry on f' and x^* we have

$$\begin{aligned} \varphi f'(x^*(z), z, t) &= f'(\varphi x^*(z), \varphi z, t+\tau) \\ &= f'(x^*(\varphi z), \varphi z, t+\tau). \end{aligned} \tag{3.21}$$

Substituting (3.20) into (3.21) yields

$$\begin{aligned} \varphi B_\ell(z) e^{i\ell\Omega t} &= B_\ell(\varphi z) e^{i\ell\Omega(t+\tau)} \\ &= p_\ell B_\ell(\varphi z) e^{i\ell\Omega t} \end{aligned} \tag{3.22}$$

since $e^{i\ell\Omega\tau} = e^{2\pi i\ell/r} \triangleq p_\ell$. Hence $B_\ell(z) = p_\ell \varphi^{-1} B_\ell(\varphi z)$. ∎

A similar result follows for frequency response $X(z)$ of (3.19).

Lemma 3.5.2 *If model f has symmetry (3.5) and equilibrium point x^* has the symmetry of Lemma 3.3.2, then the linear forced response X of (3.19) has symmetry $X(z) = p_\ell \varphi^{-1} X(\varphi z)$.*

Proof: By Theorem 3.2.1, trajectories ξ have symmetry

$$\xi(\hat{x}, s, z, t) = \varphi^{-1} \xi(\varphi\hat{x}, s+\tau, \varphi z, t+\tau).$$

For stable $M(z)$ as considered in Section 4.3, the linear steady state response is given by

$$\xi(z,t) = x^*(z) + X(z) e^{i\ell\Omega t}$$

where initial conditions $\hat{x}, s$ may be dropped because the transient decays to zero. By symmetry of ξ we have

$$\varphi\xi(z,t) = \varphi x^*(z) + \varphi X(z) e^{i\ell\Omega t} = \xi(\varphi z, t+\tau) = x^*(\varphi z) + X(\varphi z) e^{i\ell\Omega(t+\tau)}.$$

However, $\varphi x^*(z) = x^*(\varphi z)$ and so

$$\varphi X(z) = X(\varphi z)e^{i\ell\Omega\tau} \triangleq p_\ell X(\varphi z)$$

which ends the proof. ∎

Lemma 3.5.2 implies that if we know the first blade dynamics $X_1(z)$ for arbitrary mistuning z, we know the entire response by

$$\begin{aligned} X_2(z) &= p_\ell X_1(\varphi z) \\ X_3(z) &= p_\ell^2 X_1(\varphi^2 z) \\ &\vdots \qquad\quad \vdots \\ X_r(z) &= p_\ell^{r-1} X_1(\varphi^{r-1} z). \end{aligned} \tag{3.23}$$

This is true for all the symmetries (linearization M, eigenvectors V and U, eigenvalues λ, forcing vector B_ℓ and forced response X); they allow us to find the entire object for any mistuning z by computing a single blade or block as a functional form.

3.6 Eigenvalue and Eigenvector Symmetry

Given symmetry (3.13) of linearization (3.12), we can derive symmetries for eigenvalues and left, right eigenvectors of $M(z)$. First we show that eigenvalues $\lambda_i(z)$ are invariant under rotation.

Lemma 3.6.1 *If the Jacobian has symmetry $M(z) = \varphi^{-1}M(\varphi z)\varphi$, then its eigenvalues $\lambda_i(z)$ have symmetry $\lambda_i(z) = \lambda_i(\varphi z)$.*

Proof: An eigenvalue $\lambda_i(z)$ satisfies $M(z)V(z) = \lambda_i(z)V(z)$ where $V(z)$ is the corresponding right eigenvector. By symmetry

$$\begin{aligned} M(z)V(z) &= \lambda_i(z)V(z) \\ \varphi\{M(z)V(z)\} &= \lambda_i(z)\varphi V(z) \qquad \text{rotate both sides} \\ M(\varphi z)\{\varphi V(z)\} &= \lambda_i(z)\varphi V(z) \qquad \text{by symmetry of } M. \end{aligned}$$

So $\lambda_i(z)$ is also an eigenvalue of $M(\varphi z)$ with eigenvector $\varphi V(z)$, hence by definition there exists an eigenvalue $\lambda_j(\varphi z)$ of $M(\varphi z)$ with $\lambda_i(z) = \lambda_j(\varphi z)$. Setting $z = 0$ we see that these must be the same eigenvalue $i = j$. (Unless $\lambda_i(0)$ is non-distinct, in which case numbering of the repeated eigenvalues is arbitrary.) Consequently $\lambda_i(z) = \lambda_i(\varphi z)$. ∎

Using the indexing notation of Theorem 3.4.1 we relabel eigenvalues and left, right eigenvectors as $\lambda_j^d(z), U_j^d(z)$ and $V_j^d(z)$ respectively. Recall that left (row) eigenvectors and right (column) eigenvectors satisfy

$$M(z)V_j^d(z) = \lambda_j^d(z)V_j^d(z), \qquad U_j^d(z)M(z) = \lambda_j^d(z)U_j^d(z).$$

Our notation allows an elegant formulation of eigenvector symmetry.

Lemma 3.6.2 *For Jacobian with symmetry $M(z) = \varphi^{-1}M(\varphi z)\varphi$ and distinct eigenvalues, the right and left eigenvectors V_j^d, U_j^d in notation of Theorem 3.4.1 have symmetry*

$$\begin{aligned} V_j^d(z) &= p_j\varphi^{-1}V_j^d(\varphi z) \\ U_j^d(z) &= p_j^{-1}\varphi^{-1}U_j^d(\varphi z). \end{aligned}$$

Proof: By definition

$$\begin{aligned} M(z)V_j^d(z) &= \lambda_j^d(z)V_j^d(z) \\ \varphi\{M(z)V_j^d(z)\} &= \lambda_j^d(z)\varphi V_j^d(z) \qquad \text{rotate both sides} \\ M(\varphi z)\{\varphi V_j^d(z)\} &= \lambda_j^d(\varphi z)\varphi V_j^d(z) \qquad \text{by symmetry of } M \text{ and } \lambda. \end{aligned}$$

So $\varphi V_j^d(z)$ is the j,dth right eigenvector of $M(\varphi z)$. Since eigenvectors with distinct eigenvalues are unique up to a scaling constant, we have $\varphi V_j^d(z) = \alpha V_j^d(\varphi z)$. Applying this symmetry r times we find $V_j^d(z) = \alpha^r V_j^d(z)$ hence $\alpha^r = 1$ which implies $\alpha = p_i$ for some i. Alternatively, or to check that $i = j$, we set $z = 0$ and find $\alpha = p_j$ since $\varphi V_j^d(0) = p_j V_j^d(0)$ by Theorem 3.4.1. A mirror argument holds for left eigenvectors $U_j^d(z)$. ∎

3.6.1 Repeated Eigenvalues

Generically, (tuned) circulant matrices have distinct eigenvalues. This follows from theorem 3.4.1 and is easy to see for the scalar block case ($m = 1$) since the eigenvalues are simply the Q_j's. Hence for non-distinct eigenvalues we must have $Q_i = Q_j$ for $i \neq j$ —an extra condition on the $\bar{M}_i$s which will not hold in general. For matrix blocks ($m > 1$) the same condition applies, $Q_i = Q_j$ for $i \neq j$ implies non-distinct eigenvalues. However, in the latter case we can also have non-distinct eigenvalues when a particular Q_j has non-distinct eigenvalues or if an eigenvalue of Q_j equals an eigenvalue of Q_i for $Q_i \neq Q_j$. Both additional cases are also degenerate and hence circular matrices have distinct eigenvalues generically. In other words, if we generate block circulant matrices at random, then the set of matrices with non-distinct eigenvalues forms a measure zero set. However, models are not generated at random and there are various cases which can lead to indistinct eigenvalues.

Repeated Eigenvalues through Simplifying Assumptions

Simplifying model assumptions can lead to degenericity. For example, if we have a model with no blade coupling then the resulting degenerate circular Jacobian would have the form $\bar{M}_1 \neq 0$ and $\bar{M}_2 = \bar{M}_3 = \cdots = \bar{M}_r = 0$ in which case $Q_1 = Q_2 = \cdots = Q_r = \bar{M}_1$ and all the eigenvalues are non-distinct. Another example is the simple model cited in Chapter 2. This model is degenerate because it only includes coupling between adjacent blades and so $\bar{M}_1 \neq 0, -\bar{M}_2 = \bar{M}_r \neq 0$ while $\bar{M}_3 = \bar{M}_4 = \cdots = \bar{M}_{r-1} = 0$. Hence some of the Q_j's repeat and there are some non-distinct eigenvalues.

Repeated Eigenvalues via Additional Symmetries

Additional symmetries can also lead to repeated eigenvalues. Good examples are flip symmetric systems (system invariant under $\theta \mapsto -\theta$ both structurally and aerodynamicaly, see Figure 3.3). Now the Jacobian has additional symmetry $M(z) = \phi^{-1}M(\phi z)\phi$ where ϕ is the flip operator. For the mistuning vector, ϕ takes the form $\phi[z_1, z_2, \ldots, z_r] = [z_r, z_{r-1}, \ldots, z_2, z_1]$. If we had a partial differential equation description $\dot{x}(\theta) = M[x(\theta)]$ where θ is the angle along the disk as in Figure 3.3, then flip of the state vector would be given as $\phi x(\theta) = x(-\theta)$. For a finite dimensional description we write $\phi[x_1, x_2, \ldots, x_r] = [\hat{\phi}x_r, \hat{\phi}x_{r-1}, \ldots, \hat{\phi}x_2, \hat{\phi}x_1]$. The action of $\hat{\phi}$ on the state x_j of blade j depends on our choice of x_j. If x_j describes a flip symmetric state of blade j (here $x_j = [x_j^1, x_j^2, \ldots, x_j^m]$ might be the m bending modes or the deflection of m points along the centerline of blade j) then it is not necessary to change the order of x_j itself and so $\hat{\phi} = I$. However, if x_j describes asymmetric modes (for example $x_j = [x_j^1, x_j^2]$ where x_j^1 is the deflection of the clockwise tip and x_j^2 is the deflection of the counter-clockwise tip of blade j), then $\hat{\phi}[x_j^1, x_j^2] = [x_j^2, x_j^1]$ and when applying ϕ it is necessary not only to reverse the blocks x_j but also to flip each block itself via $\hat{\phi}$. If x_j contains both flip symmetric and asymmetric components, then $\hat{\phi}$ is a combination of the two cases above. In all cases $\phi^2 = I$ because two flips return the original system, hence $\phi^{-1} = \phi$ and $\hat{\phi}^{-1} = \hat{\phi}$.

Flip symmetry $M(z) = \phi^{-1}M(\phi z)$ implies a constraint on the tuned linearization $M(0) = \bar{M}$. Namely, $\hat{\phi}\bar{M}_1\hat{\phi} = \bar{M}_1, \hat{\phi}\bar{M}_2\hat{\phi} = \bar{M}_r, \hat{\phi}\bar{M}_3\hat{\phi} = \bar{M}_{r-1}, \ldots$. (This *does not* imply that $\bar{M}_1^T = \bar{M}_1, \bar{M}_2^T = \bar{M}_r, \ldots$.) Since $\hat{\phi}^{-1} = \hat{\phi}$ it follows from (3.16) that Q_j and Q_{-j} are similar, $\hat{\phi}Q_j\hat{\phi} = Q_{-j}$, and so eigenvalues repeat, $\lambda_j = \lambda_{-j}$, for $j \neq 0$ and $r/2$. This is a consequence of the fact that if $V(\theta)$ (or V_j for the finite dimensional system) is an eigenvector of a flip symmetric system with eigenvalue λ, then $V(-\theta)$ (respectively V_{-j}) is also an eigenvector with the same eigenvalue λ. When $V(\theta) \neq V(-\theta)$ then the eigenvalue is necessarily repeated. This corresponds to Q_j similar to Q_{r-j} for $j \neq 0, r/2$. When the eigenvalues are so repeated, there is still a full set of eigenvectors and so the eigenvalues are (generically) simple. Notice that practical fans and compressors have blade twist and so exhibit a preferred direction of spin; they are not flip symmetric.

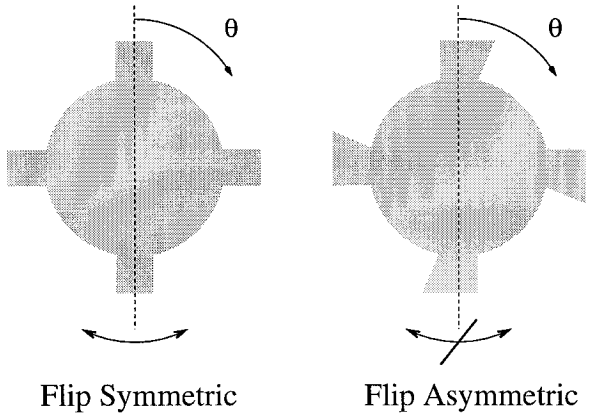

Figure 3.3: Flip symmetric and asymmetric disks.

Repeated Eigenvalues because of Simple Mechanical Structure

Simple mechanical systems have the form

$$\mathcal{M}\ddot{x} + \mathcal{K}x = 0 \tag{3.24}$$

where both the mass and stiffness matrices are symmetric and positive definite: $\mathcal{M} = \mathcal{M}^T > 0$, $\mathcal{K} = \mathcal{K}^T > 0$. For our purposes this corresponds to bladed disks with no aerodynamic forces or damping and where centrifugal forces ($\mathcal{S}\dot{x}$ term with $\mathcal{S}^T = -\mathcal{S}$) may be ignored. (When a centrifugal force is present, the eigenvalues split.) The symmetric, positive definite structure of $\mathcal{M}$ and $\mathcal{K}$ holds true even if there is no rotational symmetry. For a tuned bladed disk, we have the rotational symmetry $\varphi\mathcal{M} = \mathcal{M}\varphi$ and $\varphi\mathcal{K} = \mathcal{K}\varphi$. If, in addition, the disk is flip symmetric, we also have $\phi\mathcal{M} = \mathcal{M}\phi$ and $\phi\mathcal{K} = \mathcal{K}\phi$.

Equation (3.24) leads to the eigenvalue/vector problem

$$\lambda^2\mathcal{M}V + \mathcal{K}V = 0. \tag{3.25}$$

It follows immediately that the eigenvalues λ are purely imaginary. If λ is an eigenvalue with eigenvector V, then premultiplying equation (3.25) by $V^* = \bar{V}^T$ (the conjugate transpose)

yields

$$\lambda^2 \underbrace{V^*\mathcal{M}V}_{\geq 0} + \underbrace{V^*\mathcal{K}V}_{>0} = 0. \tag{3.26}$$

Since $\mathcal{M}, \mathcal{K}$ are positive definite, then $\lambda^2 = -V^*\mathcal{K}V/V^*\mathcal{M}V$ is real and negative. Hence λ is purely imaginary. Combining this property of mechanical systems with circular symmetry will cause the eigenvalues to repeat.

Consider the tuned system $\varphi\mathcal{M} = \mathcal{M}\varphi$ and $\varphi\mathcal{K} = \mathcal{K}\varphi$. Analogous to $M(0)$ in equation (3.15), matrices $\mathcal{M}$ and $\mathcal{K}$ have block circular form

$$\mathcal{M} = \begin{bmatrix} \mathcal{M}_1 & \mathcal{M}_2 & \dots & \mathcal{M}_r \\ \mathcal{M}_r & \mathcal{M}_1 & \mathcal{M}_2 & \dots \\ & \ddots & & \\ \mathcal{M}_2 & \mathcal{M}_3 & \dots & \mathcal{M}_1 \end{bmatrix}, \quad \mathcal{K} = \begin{bmatrix} \mathcal{K}_1 & \mathcal{K}_2 & \dots & \mathcal{K}_r \\ \mathcal{K}_r & \mathcal{K}_1 & \mathcal{K}_2 & \dots \\ & \ddots & & \\ \mathcal{K}_2 & \mathcal{K}_3 & \dots & \mathcal{K}_1 \end{bmatrix}. \tag{3.27}$$

Let $\mu = \lambda^2$ and define

$$Q_j^{\mathcal{M}} = \mathcal{M}_1 + p_j\mathcal{M}_2 + p_j^2\mathcal{M}_3 + \cdots + p_j^{r-1}\mathcal{M}_r \tag{3.28}$$

$$Q_j^{\mathcal{K}} = \mathcal{K}_1 + p_j\mathcal{K}_2 + p_j^2\mathcal{K}_3 + \cdots + p_j^{r-1}\mathcal{K}_r. \tag{3.29}$$

Then the following is a natural extension of Theorem 3.4.1 to simple mechanical systems.

Theorem 3.6.1 *For $\mathcal{M}, \mathcal{K}$ block circular matrices as in (3.27), let μ_j^d, u_j^d and v_j^d be the dth eigenvalue, left eigenvector ($-\mu_j^d u_j^d Q_j^{\mathcal{M}} = u_j^d Q_j^{\mathcal{K}}$) and right eigenvector ($-\mu_j^d Q_j^{\mathcal{M}} v_j^d = Q_j^{\mathcal{K}} v_j^d$), respectively, of the pair $Q_j^{\mathcal{M}}, Q_j^{\mathcal{K}}$. Then μ_j^d form the eigenvalues of the pair $\mathcal{M}, \mathcal{K}$ with left ($-\mu U\mathcal{M} = U\mathcal{K}$) and right ($-\mu\mathcal{M}V = \mathcal{K}V$) eigenvectors $U_j^d = [u_j^d, p_j^{r-1}u_j^d, p_j^{r-2}u_j^d, \dots, p_j u_j^d]$ and $V_j^d = [v_j^d, p_j v_j^d, \dots, p_j^{r-2}v_j^d, p_j^{r-1}v_j^d]$.*

Proof: To prove the theorem we need only show $-\mu_j^d \mathcal{M} V_j^d = \mathcal{K} V_j^d$ and $-\mu_j^d U_j^d \mathcal{M} = U_j^d \mathcal{K}$. Both statements are verified by substitution. ∎

But, $\mathcal{M}^T = \mathcal{M}$ and $\mathcal{K}^T = \mathcal{K}$ because we are dealing with a mechanical system. Hence

$$Q_j^{\mathcal{M}} = \mathcal{M}_1 + p_j\mathcal{M}_2 + p_j^2\mathcal{M}_3 + \cdots + p_j^{r-2}\mathcal{M}_3^T + p_j^{r-1}\mathcal{M}_2^T \tag{3.30}$$

$$Q_j^{\mathcal{K}} = \mathcal{K}_1 + p_j\mathcal{K}_2 + p_j^2\mathcal{K}_3 + \cdots + p_j^{r-2}\mathcal{K}_3^T + p_j^{r-1}\mathcal{K}_2^T. \tag{3.31}$$

Since $\bar{p}_j = p_{r-j}$ it follows that $\left(Q_j^{\mathcal{M}}\right)^T = Q_{-j}^{\mathcal{M}}$ and $\left(Q_j^{\mathcal{K}}\right)^T = Q_{-j}^{\mathcal{K}}$. Thus the pairs $Q_j^{\mathcal{M}}, Q_j^{\mathcal{K}}$ and $Q_{-j}^{\mathcal{M}}, Q_{-j}^{\mathcal{K}}$ have the same eigenvalues. This is a non-trivial relationship for $j \neq 0$ and $r/2$ and so all eigenvalues repeat except μ_0^d and $\mu_{r/2}^d$. This means right/left eigenvector blocks of Theorem 3.6.1 satisfy the relationship

$$v_j^d = \left(u_{-j}^d\right)^T = \bar{v}_{-j}^d \tag{3.32}$$

$$u_j^d = \left(v_{-j}^d\right)^T = \bar{u}_{-j}^d. \tag{3.33}$$

The last equality follows from $\bar{Q}_j^{\mathcal{M}} = Q_{-j}^{\mathcal{M}}, \bar{Q}_j^{\mathcal{K}} = Q_{-j}^{\mathcal{K}}$ which is true just because $\mathcal{M}$ and $\mathcal{K}$ are real, see equations (3.28) and (3.29). Hence for the real repeated eigenvalues μ_j^d $(j \neq 0, r/2)$ one can span the eigenspace by two complex eigenvectors V_j and $\bar{V}_j = V_{-j}$ or by the real and imaginary components: Re$[V_j]$, Im$[V_j]$.

If the disk is flip symmetric and we also have $\phi\mathcal{M} = \mathcal{M}\phi$, $\phi\mathcal{K} = \mathcal{K}\phi$ then $\hat{\phi}Q_j^{\mathcal{M}} = Q_{-j}^{\mathcal{M}}\hat{\phi}$ and $\hat{\phi}Q_j^{\mathcal{K}} = Q_{-j}^{\mathcal{K}}\hat{\phi}$. Thus

$$-\mu_j^d Q_j^{\mathcal{M}} v_j^d = Q_j^{\mathcal{K}} v_j^d \tag{3.34}$$

$$-\mu_j^d \hat{\phi} Q_j^{\mathcal{M}} v_j^d = \hat{\phi} Q_j^{\mathcal{K}} v_j^d \tag{3.35}$$

$$-\mu_j^d Q_{-j}^{\mathcal{M}} \left(\hat{\phi} v_j^d\right) = Q_{-j}^{\mathcal{K}} \left(\hat{\phi} v_j^d\right) \tag{3.36}$$

and so $\hat{\phi}v_j^d$ must be an eigenvector of $Q_{-j}^{\mathcal{M}}, Q_{-j}^{\mathcal{K}}$, meaning $\hat{\phi}v_j^d = \alpha v_{-j}^d$. (The constant α is necessary else the conditions on eigenvectors are over-constrained.) Recall, $\bar{v}_j^d = v_{-j}^d$ so $v_j^d = \hat{\phi}^2 v_j^d = \hat{\phi}(\alpha v_{-j}^d) = \alpha\,\hat{\phi}\bar{v}_j^d = \alpha\,\overline{\hat{\phi}v_j^d} = \alpha\bar{\alpha}\,v_j^d$ hence $\alpha\bar{\alpha} = 1$ or $\alpha = e^{i\theta}$. Equations (3.32)

and (3.33) now become

$$v_j^d = \left(u_{-j}^d\right)^T = \bar{v}_{-j}^d = e^{i\theta}\hat{\phi}v_{-j}^d \tag{3.37}$$

$$u_j^d = \left(v_{-j}^d\right)^T = \bar{u}_{-j}^d = e^{-i\theta}\hat{\phi}u_{-j}^d. \tag{3.38}$$

The constraint above ($\bar{v}_{-j}^d = e^{i\theta}\hat{\phi}v_{-j}^d$ or $\bar{v}_j^d = e^{-i\theta}\hat{\phi}v_j^d$) allows flip asymmetric eigenvectors $\hat{\phi}v_j^d \neq v_j^d$. For example $v_j^d = [a, e^{i\theta}\bar{a}]$ is valid, so long as the flip vector, here $v_{-j}^d = [\bar{a}, e^{-i\theta}a]$, also appears. So if V_j is an asymmetric eigenvector, then its flip, $\phi V_j = \beta V_{-j}$, is also an eigenvector (β turns out to be $\bar{p}_j e^{i\theta}$).

3.6.2 Eigenspaces for Repeated Eigenvalues

It is important to realize that in all the cases above the non-distinct eigenvalues are generically simple (have diagonal Jordan form) and so travel smoothly with parameters. This is because each of the Q_j's will have distinct eigenvalues generically. As a result, each Q_j will typically have a complete set of left and right eigenvectors $\{u_j^d, v_j^d\}_{d=1}^m$ and so $M(0)$ will have a complete set of left and right eigenvector $\{U_j^d, V_j^d\}_{j,d=1}^{r,m}$. (This is because unlike the block matrices Q_j, the eigenvectors U_j^d, V_j^d do not repeat.) Hence in the case where Q_j's repeat we will have non-distinct but typically simple eigenvalues which travel smoothly with parameters. (In contrast, repeated eigenvalues for non-circulant matrices are generically non-simple. In our case, if repeated eigenvalues are caused by degenericity within a single blade block, say by some very special blade shape, then the repeated eigenvalues will indeed be generically non-simple [there is no circular structure within a blade block to force a diagonal Jordan form]. However, all the degenerate cases listed above correspond to global, blade to blade, degenericities and thus the circulant matrix structure implies that when eigenvalues repeat they are generically simple.)

Nevertheless, these non-distinct simple eigenvalues can allow for some interesting behaviour. In [KMW98], a purely mechanical, flip-symmetric, tuned bladed-disk is shown to display asymmetric mode shapes (eigenvectors). This follows directly from non-distinct (doublet) eigenvalues implied by the mechanical (or flip symmetric) structure. Mimicking

the proof of Lemma 3.6.2 for tuned eigenvalue $\lambda_j^d(0)$ yields

$$\begin{aligned} M(0)V_j^d(0) &= \lambda_j^d(0)V_j^d(0) \\ \varphi\{M(0)V_j^d(0)\} &= \lambda_j^d(0)\varphi V_j^d(0) \qquad \text{rotate both sides} \\ M(0)\{\varphi V_j^d(0)\} &= \lambda_j^d(0)\varphi V_j^d(0) \qquad \text{by symmetry of } M(0). \end{aligned}$$

So $\varphi V_j^d(0)$ is also an eigenvector of $M(0)$ with eigenvalue $\lambda_j^d(0)$. If $\lambda_j^d(0)$ is *distinct* then it has a one-dimensional eigenspace spanned by $V_j^d(0)$. Hence $\varphi V_j^d(0) = \alpha V_j^d(0)$ (where $\alpha = p_j$ by Theorem 3.4.1) and so the tuned eigenvector is symmetric. However, if eigenvalue $\lambda_j^d(0)$ is repeated (say a doublet), then it has a two-dimensional eigenspace spanned by $V_j^d(0)$ and some other eigenvector $\tilde{V}$. Now $\varphi V_j^d(0)$ must lie in this subspace so $\varphi V_j^d(0) = \alpha V_j^d(0) + \beta\tilde{V}$. Hence this two-dimensional eigenspace is invariant under rotation φ. If in addition the system is flip-symmetric the eigenspace is also invariant under the flip operator ϕ. The following result is intuitive; it says a two-dimensional rotationally invariant subspace (the eigenspace above) is spanned by two symmetric vectors. (For the remainder we drop the superscript notation in eigenvectors V_j^d.)

Lemma 3.6.3 *Let X be a two-dimensional linear subspace of $\mathbb{C}^{rm}$ which is invariant under rotation $\varphi X = X$, meaning that for any $x \in X$ we have $\varphi x \in X$. Then, $X = \text{span}\{V_a, V_b\}$ where $\varphi V_a = p_a V_a$, $\varphi V_b = p_b V_b$ for some integers $a \neq b$. In other words, X is necessarily spanned by two symmetric vectors.*

Proof: Assume $X = \text{span}\{V_a, V_b\}$ with $\varphi V_a = p_a V_a$, $\varphi V_b = p_b V_b$. For any $x \in X$ we have $x = \alpha V_a + \beta V_b$ so $\varphi x = \alpha\varphi V_a + \beta\varphi V_b = \alpha p_a V_a + \beta p_b V_b$ hence $\varphi x \in X$.

Now suppose $X = \text{span}\{x, y\}$ and $\varphi X = X$, we need to show X is spanned by V_a, V_b with $\varphi V_a = p_a V_a$, $\varphi V_b = p_b V_b$ for some integers $a \neq b$. If $x = \alpha_1 V_a + \beta_1 V_b$, $y = \alpha_2 V_a + \beta_2 V_b$ with $\varphi V_a = p_a V_a$, $\varphi V_b = p_b V_b$ then we are done. Otherwise,

$$x = \alpha_1 V_a + \beta_1 V_b + \epsilon \tag{3.39}$$

$$y = \alpha_2 V_a + \beta_2 V_b + \delta \tag{3.40}$$

where ϵ and δ do not contain V_a, V_b components ($\epsilon^T V_a = \epsilon^T V_b = \delta^T V_a = \delta^T V_b = 0$). We can

let $\hat{x}, \hat{y}$ be linear combinations of x, y to eliminate V_b from $\hat{x}$ and V_a from $\hat{y}$. This yields

$$\hat{x} = V_a + \hat{\epsilon} \tag{3.41}$$

$$\hat{y} = V_b + \hat{\delta} \tag{3.42}$$

where $\hat{x}, \hat{y}$ still span X. Since $\hat{x}, \hat{y} \in X$ it follows that $\varphi\hat{x}, \varphi\hat{y} \in X$ so

$$\varphi\hat{x} = c\hat{x} + d\hat{y}. \tag{3.43}$$

By equations (3.41), (3.42) and (3.43),

$$\varphi\hat{x} = p_a V_a + \varphi\hat{\epsilon} = c(V_a + \hat{\epsilon}) + d(V_b + \hat{\delta}). \tag{3.44}$$

But $\hat{\epsilon}$ and $\hat{\delta}$ do not contain V_a, V_b components so $c = p_a$ and $d = 0$. Thus $\varphi\hat{\epsilon} = p_a\hat{\epsilon}$ which means $\hat{\epsilon} = 0$ since $\hat{\epsilon}$ has no V_a component and only V_a has symmetry $\varphi V_a = p_a V_a$. Similarly, $\hat{\delta} = 0$. Hence $\hat{x} = V_a$ and $\hat{y} = V_b$ are symmetric; they span X and the proof is complete. ■

A doublet tuned eigenvalue $\lambda(0)$ has an eigenspace X with the properties of Lemma 3.6.3. The natural choice of basis for this eigenspace is two symmetric eigenvectors $\varphi V_j^d = p_j V_j$ and $\varphi V_i^d = p_i V_i$ as above. However, one can pick asymmetric eigenvectors $V_1 = \alpha_1 V_j + \beta_1 V_i$ and $V_2 = \alpha_2 V_j + \beta_2 V_i$ so long as they are linearly independent. (Vector V_1 is asymmetric since $\varphi V_1 = \alpha_1 \varphi V_j + \beta_1 \varphi V_i = \alpha_1 p_j V_j + \beta_1 p_i V_j \neq \gamma V_1$ in general.) This explains how asymmetric tuned modes (eigenvectors) are possible in [KMW98]; they are necessarily produced by the summation of two symmetric modes. In fact, since the system is purely mechanical and flip symmetric, the two modes must be V_j and V_{-j}. This explains the "checkerboard" diagram in [KMW98].

In conclusion, repeated eigenvalues are degenerate. However, degenericity may be created by extra structure (such as flip symmetry, modeling assumptions or a simple mechanical form of the equations). In practice: flip asymmetry (direction of spin or blade twist), centrifugal forces (note spinning implies flip asymmetry since it creates a preferred direction) or presence

Object	Symbol	Symmetry	Proof
Model	f	$f(x,z,t) = \varphi^{-1} f(\varphi x, \varphi z, t+\tau)$	Section 3.1
Unforced model	$\bar{f}$	$\bar{f}(x,z) = \varphi^{-1} \bar{f}(\varphi x, \varphi z)$	Follows from above
Trajectories	ξ	$\xi(\hat{x},s,z,t) = \varphi^{-1} \xi(\varphi \hat{x}, s+\tau, \varphi z, t+\tau)$	Theorem 3.2.1
Equilibrium	x^*	$x^*(z) = \varphi^{-1} x^*(\varphi z)$	Lemma 3.3.2
Response	X	$X(z) = p_\ell \varphi^{-1} X(\varphi z)$	Lemma 3.5.2
Forcing vector	B_ℓ	$B_\ell(z) = p_\ell \varphi^{-1} B_\ell(\varphi z)$	Lemma 3.5.1
Linearization	M	$M(z) = \varphi^{-1} M(\varphi z) \varphi$	Lemma 3.4.1
Eigenvalues	λ	$\lambda(z) = \lambda(\varphi z)$	Lemma 3.6.1
R. Eigenvectors	V_j^d	$V_j^d(z) = p_j \varphi^{-1} V_j^d(\varphi z)$	Lemma 3.6.2
L. Eigenvectors	U_j^d	$U_j^d(z) = p_j^{-1} \varphi^{-1} U_j^d(\varphi z)$	Lemma 3.6.2

Table 3.1: System symmetries: $p_j = \exp(2\pi i j/r)$.

of aerodynamic forces serves to split the eigenvalues. All the models analyzed in this thesis have distinct eigenvalues. When the eigenvalues are repeated, they are still generically simple and so the eigenvalue perturbation results of Section 4.2.2 continue to hold. For the forced response results of Section 4.3.5, the eigenvector perturbation equations contain tuned eigenvectors corresponding to repeated eigenvalues which must be chosen so as to diagonalize the mistuning perturbation matrix. This makes the perturbation depend on the specific mistuning chosen (introducing the same extra degrees of freedom as the number of repeated eigenvalues) and complicates the analysis.

3.7 Symmetry Summary

We have seen that symmetry (3.5) on the full nonlinear system (3.1) implies symmetries on all subsequent objects, be they equilibrium points, forcing vectors or eigenvalues. In fact, symmetry permeates all issues associated with mistuning, from initial model formulation up to final design optimization. We shall exploit such symmetries throughout the remainder of this work. For the moment, Table 3.1 lists all symmetries developed so far.

Chapter 4 Analysis of Mistuned Stability and Forced Response

Our central aim is shown in Figure 1.5 of the introduction (repeated here as Figure 4.1). At

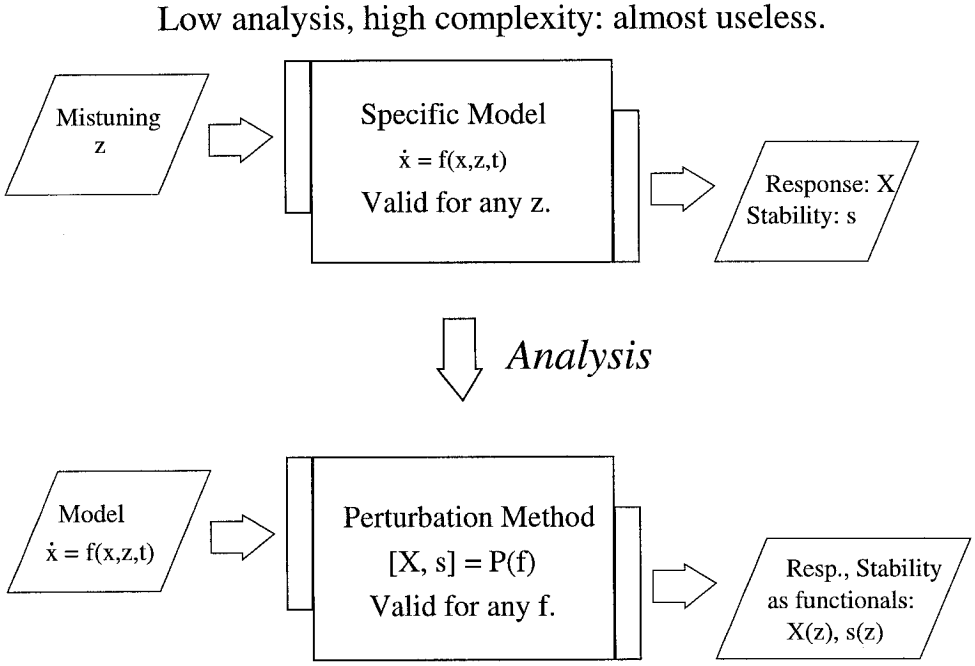

Figure 4.1: Developing a method valid for any model.

the top of Figure 4.1 we find the simplest approach: given a model f and specific mistuning z, find the stability s and forced response X. Our goal here is the analysis arrow of Figure 4.1 which achieves the approach at the bottom of Figure 1.5: given a model f find stability and forced response for all (small) mistuning. Sections 4.2 and 4.3 develop a mistuning perturbation method for stability and forced response respectively. Using the symmetry arguments of Section 3 they yield expressions for stability and forced response as a function of mistuning. This allows an in-depth understanding of mistuning tradeoffs, sensitivity, parameter dependence and robustness.

4.1 The Linear Problem

To leading order, both forced response and stability are linear problems (however, their solutions are highly nonlinear in the mistuning parameter z). These standard linear problems are derived below. Two analytic methods are required to solve them: the first is a symmetry arguments tool box as addressed in Section 3, the second is a set of linear algebra tools dealing with perturbations of eigenvalues and eigenvectors, Section 4.3.

In order to show the assumptions made, break up the full forced nonlinear system (3.1) into a forced and unforced part

$$\dot{x} = f(x, z, t) = \bar{f}(x, z) + f'(x, z, t), \tag{4.1}$$

here $\bar{f}$ is the dynamics of (3.1) if there is no disturbance and f' is defined as $f - \bar{f}$. For example, if we think of forcing due to a stationary inlet distortion, then $\bar{f}$ corresponds to the dynamics with zero distortion while f' is the additional dynamics produced by a nonzero distortion.

Now consider an equilibrium point $x^*(z)$ of the unforced system, $\bar{f}(x^*(z), z) = 0$. (It is crucial to note that x^* can vary with mistuning, for instance a change in stiffness will cause different nominal deformations in blades due to aerodynamic loading.)

It is valid to assume the equilibrium point of interest x^* for the tuned unforced system $\bar{f}(x, 0)$ is symmetric: $x^*(0) = \varphi x^*(0)$. For if this assumption does not hold then we must have a whole family of equilibria: $x_1^*(0) = x^*(0), x_2^*(0) = \varphi x^*(0), x_3^*(0) = \varphi^2 x^*(0), \cdots, x_r^*(0) = \varphi^{r-1} x^*(0)$, see Lemma 3.3.1, which is an occurrence typically not seen in jet engines. Linearization of (4.1) about $x^*(z)$ yields the time-varying linear dynamics

$$\dot{x} = \left[\underbrace{\frac{\partial \bar{f}}{\partial x}(x^*(z), z)}_{\text{time-invariant}} + \underbrace{\frac{\partial f'}{\partial x}(x^*(z), z, t)}_{\text{time-varying}} \right] \{x - x^*(z)\} + \underbrace{f'(x^*(z), z, t)}_{\text{forcing}}. \tag{4.2}$$

As an example, in simple aerodynamic model of Chapter 2 the (state dependent) force on blade i is proportional to the distance between adjacent blades times the sin of the incidence

angle: $\sin(\alpha)[x_{i+1} - x_{i-1}]$. An inlet distortion changes the incoming velocity in the fixed frame and so spinning blades see a resulting variation in incidence angle as a function of time, $\alpha(t) = \alpha + \Delta(t)$. This results in the linear time-varying perturbation term $[\sin(\alpha + \Delta(t)) - \sin(\alpha)][x_{i+1} - x_{i-1}]$. Even though such terms are physically of second order (the first order effect is clearly the time-invariant term $\sin(\alpha)[x_{i+1} - x_{i-1}]$), they are perturbing a lightly damped matrix $[\partial \bar{f}/\partial x]$ (turbomachines have lightly damped modes) and so may cause large changes. Clearly one must solve the time-invariant problem before attempting the more difficult time-varying case, and so we neglect the $[\partial f'/\partial x]$ term in the remainder. However, future work should examine the effect of the time-varying $[\partial f'(\ldots, t)/\partial x]$ term and check whether it can be ignored.

Neglecting higher order terms (including the time-varying linear term $[\partial f'(\ldots, t)/\partial x]$ as above) we get the standard linear problem

$$\dot{x} = M(z)x + B_\ell(z)e^{i\ell\Omega t}. \tag{4.3}$$

As defined previously (equation (3.12))

$$M(z) \triangleq \left[\frac{\partial \bar{f}}{\partial x}(x^*(z), z)\right] \tag{4.4}$$

and the deviation from equilibrium $x - x^*(z)$ has been relabeled as x. Coefficient B_ℓ corresponds to the ℓth spatial mode of the disturbance in the fixed reference frame: $\zeta(\theta) = \sin(\ell\theta)$ in Figure 3.1 with resulting forcing frequency $\omega = \ell\Omega$.

For $M(z)$ stable the transient response decays to zero and the steady state forced response may be written in frequency domain as

$$X(z) = [i\omega I - M(z)]^{-1} B_\ell(z). \tag{4.5}$$

Here steady state forced response in the time domain is given by $\bar{x}(z,t) = X(z)e^{i\omega t}$. Since the analysis is conducted at a fixed spatial mode ℓ, X dependence on ℓ and ω is understood but dropped in the notation.

Up to our linear time-invariant formulation, expression (4.5) provides the exact stability

and forced response for any specific mistuning z. Yet (4.5) by itself is not useful for two reasons.

1. It is computationally infeasible to re-evaluate (4.5) for each new mistuning pattern; typical cascade models have many states and require long computation times. Consequently, it is impractical to characterize response to mistuning by computing (4.5) for a large set of mistuning patterns.

2. Computing (4.5) for each new pattern z provides almost no understanding. Sensitivity and parameter dependence is not revealed by exhaustive calculation.

Instead one should find an approximation of the stability and forced response as a function of mistuning, $\lambda(z) \approx \tilde{\lambda}(z), X(z) \approx \tilde{X}(z)$, where $\tilde{\lambda}, \tilde{X}$ are tractable and provide insight. The eigenvalues $\lambda(z)$ are reduced to a simple form by symmetry and the coefficients in this form may be calculated by standard eigenvalue derivative methods. For the forced response case we must approximate the inverse of $A(z) = [i\omega I - M(z)]$ in (4.5) as a function of z. In Section 4.3.1 we find that because $A(z)$ is almost singular, its inverse is a steep nonlinear function of z. Thus approximating this inverse matrix is at once our main aim and the major difficulty.

4.2 Stability Approximation

Our first goal is to define the stability boundary change, $s(z)$, due to mistuning. Flutter boundaries are defined in terms of a performance or loading parameter U. Here $U \in \mathbb{R}$ denotes a parameter of practical interest such as engine-throttle, Mach-number, reduced-frequency or rotor speed. Typically, a cascade will lose stability at some critical loading U_{crit}, and so operation will not be possible beyond this point. The critical loading U_{crit} depends on mistuning, and so we can have a stability change $s(z)$ due to mistuning. To define the stability change, we rewrite the unforced dynamics in (4.1) with loading U,

$$\dot{x} = \bar{f}(x, U, z). \tag{4.6}$$

For any fixed U, model $\bar{f}(x, U, z)$ reduces to $\bar{f}(x, z)$ of equation (4.1) and so all previous results still hold.

For a fixed z, as we vary the loading parameter U within some operating range $[U_0, U_1]$, the system (4.6) traverses a set of equilibria $X^*(U, z)$ defined by

$$X^*(U, z) = \{x^* : \bar{f}(x^*, U, z) = 0, U \in [U_0, U_1]\}. \tag{4.7}$$

Assuming that $X^*(U, z)$ is non-empty for z in some neighbourhood of the origin and for all $U \in [U_0, U_1]$, we pick a subset $x^*(U, z) \subset X^*(U, z)$ which corresponds to the equilibrium point of interest at each U. As an example, suppose we have a model (4.6) of a (tuned) jet engine with $z = 0$, U is the throttle and it varies between U_0 and U_1, then we can think of $x^*(U, 0)$ as the design operating point which varies as a function of throttle setting. Clearly, $x^* : \mathbb{R} \times \mathbb{R}^r \to \mathbb{R}^n$ is a function of U and z, possibly discontinuous and non-smooth in both arguments. (Continuity and smoothness assumptions will be discussed shortly.)

Now consider the stability of $x^*(U, z)$ as a function of U for a fixed z. Define

$$h(U, z) = \max[\mathrm{Re}(\lambda(U, z))], \tag{4.8}$$

where $\lambda(U, z)$ are the eigenvalues of $M(U, z) = \frac{\partial \bar{f}}{\partial x}(x^*(U, z), U, z)$ (as defined in (3.12)). If $h(U, z)$ is negative (respectively positive), then the equilibrium point $x^*(U, z)$ is stable (respectively unstable). Since we are concerned with flutter boundaries it is assumed that as the loading U increases, then at some point, U_{crit}, stability is lost. Thus, define

$$U_{crit}(z) = \min_{u \in [U_0, U_1]} \{u : h(u, z) = 0\}. \tag{4.9}$$

If $h(U, z)$ does not cross the origin for $U \in [U_0, U_1]$, let $U_{crit}(z) = \pm\infty$ with appropriate choice of sign. (When the system loses stability as U decreases, the min should be replaced with a max. Also, if there is more then one stability boundary of interest, the interval $[U_0, U_1]$ may be appropriately partitioned so that only one boundary is under consideration.) Finally, the

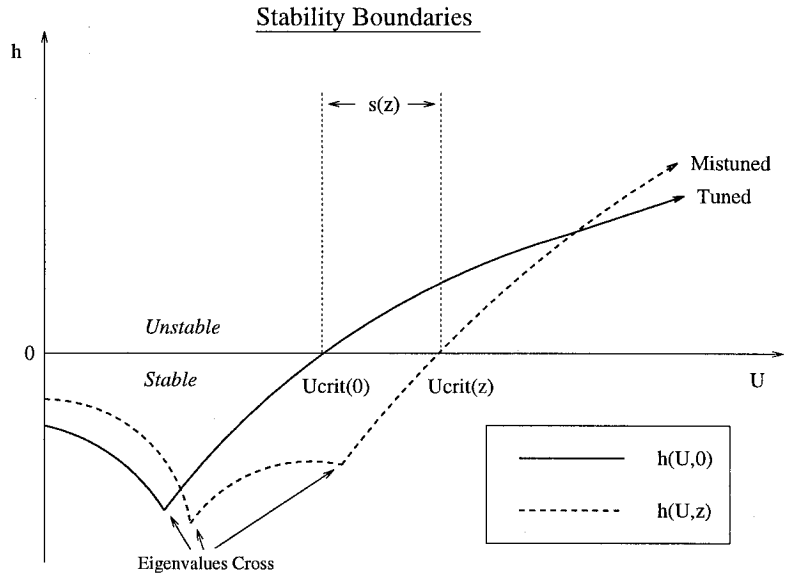

Figure 4.2: Change of stability boundary, $s(z)$.

increase in stability $s(z)$ is defined as

$$s(z) = +[U_{crit}(z) - U_{crit}(0)] \tag{4.10}$$

where the positive sign is replaced with a negative if instability occurs as U decreases. Physically, loading U may be time dependent—if we take U as Mach number it varies with outside disturbances and as blades sweep past stators and inlet guide vanes. However, we can always split a time dependent loading $U(t)$ into an averaged and perturbed part: $U(t) = U + U'(t)$. The steady part U leads to the study of stability (our current focus) while the unsteady part $U'(t)$ is exactly the forced response or mode localization problem (Section 4.3).

To summarize, $s(z)$ is simply the change in stability (at the relevant equilibrium point) as a function of mistuning. In practice, it is the change in operating range due to mistuning. The technical remarks above are appropriate because they allow us to equate assumptions on the smoothness of s with smoothness conditions on $\bar{f}$. For a graphical interpretation see Figure 4.2.

4.2.1 Stability Extension Smoothness

Smoothness of $s(z)$ is necessary so that we may take derivatives with respect to z. We will find that a leading order analysis requires derivatives up to second order (first order terms do not capture relevant behaviour); hence we need $s(z)$ to be three times differentiable in some neighbourhood Ω of the origin: $s \in C^3(\Omega)$. Since we will be approximating $s(z)$ to second order, we really care about the subset $\Theta \subset \Omega$ where $s(z)$ is accurately approximated by second order terms in z. For the analysis to be practical, this region Θ must be of a reasonable size. Typically, if $\bar{f}$, x^* are smooth and the eigenvalue of M are distinct and not too close, then both conditions above are satisfied. We briefly mention the four cases that can violate smoothness and practical size of Θ requirements.

Case one: Equilibrium point $x^*(U, z)$ does not travel smoothly with U and/or z. Typically, such problems are caused by equilibrium bifurcations and present a host of difficulties which must be dealt with before stability can be considered.

Case two: If $h(U, 0)$ has a degenerate root at $U_{crit}(0)$ as shown in Figure 4.3, then $s(z)$

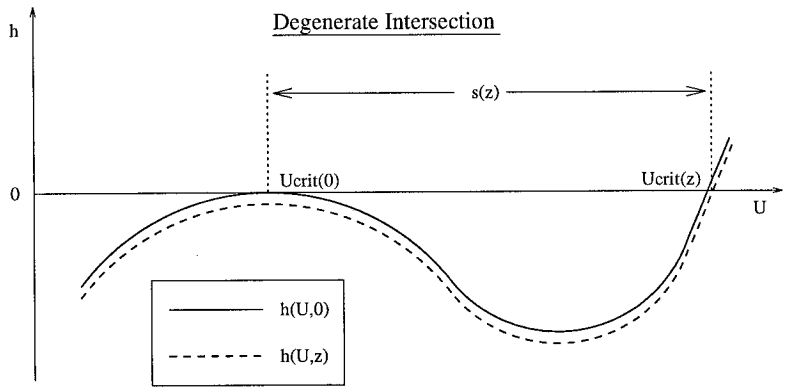

Figure 4.3: Discontinuous increase in stability boundary.

is discontinuous in z. Under such circumstances one would consider the minimum damping $h(U, z)$ at a given U instead of the stability extension $s(z)$.

Case three: If the real part of the least stable (or critical eigenvalue) in $h(U, 0)$ is very close to the real part of another eigenvalue, then it is possible that these real parts will switch as z is varied (see Figure 4.4). In this case $s(z)$ will be smooth on a very small region Ω, hence Θ (a subset) is unacceptably small. For a non-distinct least stable eigenvalue we have

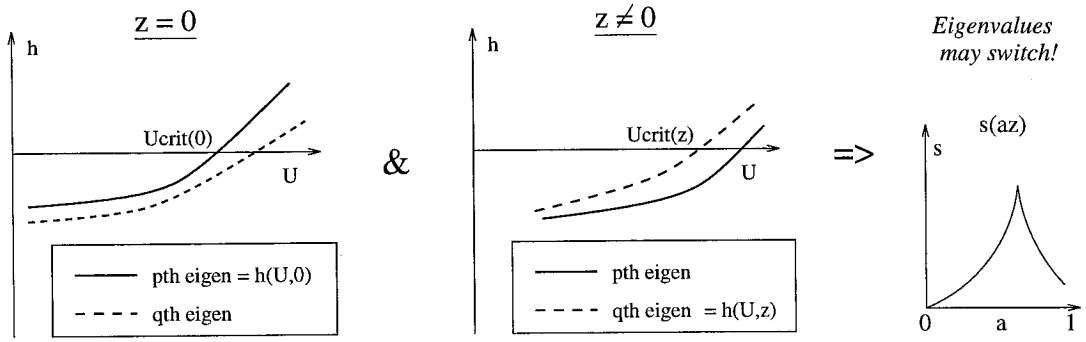

Figure 4.4: Eigenvalue switching creates a discontinuity in $s(z)$.

the special case where $s(z)$ can be discontinuous at the origin. It is possible to tackle these problems by keeping track of a number of eigenvalues during the analysis.

Case four: When eigenvalues are too close together in real and imaginary parts (almost indistinct), their motion with parameters is very complex as they veer to avoid collisions with one another. In this case, the simple leading order behaviour predicted by second order terms only applies in a tiny region Θ (see Figure 4.10). The size of region Θ essentially determines what we mean by "small" mistuning. There is no easy fix for this case within the current perturbation approach since keeping track of higher order terms in z (third, fourth, fifth, ...) quickly becomes prohibitively expensive. Notice that this case can be of practical interest (eigenvalues are nearby when the blade coupling is small) and so it should be the topic of future research. For the special case where the least stable eigenvalues is indistinct, we can have $\Theta = 0$. If this repeated eigenvalue is simple (for the circulant matrices of interest this is the generic case, see Section 3.6.2), we can track all the eigenvalues as they split and solve the problem. However, if the repeated eigenvalue is non-simple (degenerate case), its motion is fundamentally discontinuous and cannot be represented by a power series.

4.2.2 Reduction by Symmetry

Having defined the stability extension $s(z)$, our next goal is to determine its simplest form by symmetry techniques. By smoothness (see Section 4.2.1) we can expand $s(z)$ in a power

series about the origin,

$$s(z_1, \ldots, z_r) = \sum_{i=1}^{r} a_i z_i + \sum_{i,j=1}^{r} b_{ij} z_i z_j + O(\|z\|^3). \tag{4.11}$$

This power expansion is practical in the region Θ where $s(z)$ is accurately approximated by second order terms.

From Lemma 3.6.1 we know that eigenvalues have an invariance symmetry, $\lambda_i(U, z) = \lambda_i(U, \varphi z)$. It follows from (4.8) and (4.10) that h and s have the same invariance symmetry: $h(U, z) = h(U, \varphi z)$, $s(z) = s(\varphi z)$. Applying the rotation φ a total of k times we find $s(z) = s(\varphi^k[z])$ for all integers k. Taking $z = [\epsilon, 0, \ldots, 0]$ and substituting $\varphi^k[z]$ into the power expansion for all $k \in (0, 1, 2, \ldots, r-1)$, we get

$$a_1\epsilon + b_{11}\epsilon^2 = a_2\epsilon + b_{22}\epsilon^2 = \ldots = a_r\epsilon + b_{rr}\epsilon^2 \tag{4.12}$$

which holds for all ϵ up to $O(\epsilon^3)$. Consequently,

$$a_i = a_j \tag{4.13}$$

$$b_{ii} = b_{jj} \tag{4.14}$$

for all i and j. Similarly, letting $z = [0, \ldots, 0, \epsilon, 0, \ldots, 0, \epsilon, 0, \ldots, 0]$ where the ϵ's are located in the ith and jth spots, by varying i, j and k as previously we can show

$$b_{ij} + b_{ji} = b_{[i+k][j+k]} + b_{[j+k][i+k]} \tag{4.15}$$

for all i, j and k, where $[i + k] = (i + k) \mod r$. Thus symmetry yields a constraint on the power coefficients a_i, b_{ij}.

To proceed we make the following definitions,

$$
\begin{aligned}
a &\triangleq a_1 = a_2 = \cdots = a_r \\
b &\triangleq b_{11} = b_{22} = \cdots = b_{rr} \\
c_1 &\triangleq b_{12} + b_{21} = b_{23} + b_{32} = \cdots = b_{[r-1]r} + b_{r[r-1]} = b_{r1} + b_{1r} \\
c_2 &\triangleq b_{13} + b_{31} = b_{24} + b_{42} = \cdots = b_{[r-1]1} + b_{1[r-1]} = b_{r2} + b_{2r} \\
&\vdots \qquad\qquad \vdots \\
c_k &\triangleq b_{1[1+k]} + b_{[1+k]1} = \cdots = b_{rk} + b_{1k}
\end{aligned}
$$

where k is defined in the remainder as

$$
k \triangleq \begin{cases} \frac{r}{2} & r \text{ even} \\ \frac{r-1}{2} & r \text{ odd.} \end{cases}
$$

Using the definitions above, we can rewrite (4.11) as

$$
\begin{aligned}
s(z) \;=\; & a(z_1 + z_2 + \cdots + z_r) \\
& + b(z_1^2 + z_2^2 + \cdots + z_r^2) \\
& + c_1(z_1 z_2 + z_2 z_3 + \cdots + z_r z_1) \\
& + c_2(z_1 z_3 + z_2 z_4 + \cdots + z_r z_2) \\
& \vdots \qquad\qquad \vdots \\
& + c_k(z_1 z_{1+k} + z_2 z_{2+k} + \cdots + z_r z_k) + O(\|z\|^3).
\end{aligned} \tag{4.16}
$$

It is obvious by inspection that $s(z)$ is invariant under rotation as advertised. Observe that the first order term vanishes if we assume zero average mistuning, $\sum_{i=1}^{r} z_i = 0$. Equation (4.16) can be rewritten more compactly as

$$
s(z) = a \sum_{i=1}^{r} z_i + z^T S z + O(\|z\|^3) \tag{4.17}
$$

where S is defined for even and odd r, respectively,

$$S = \begin{bmatrix} b & \frac{c_1}{2} & \frac{c_2}{2} & \cdots & c_k & \cdots & \frac{c_2}{2} & \frac{c_1}{2} \\ \frac{c_1}{2} & b & \frac{c_1}{2} & \frac{c_2}{2} & \cdots & c_k & \cdots & \frac{c_2}{2} \\ \frac{c_2}{2} & \frac{c_1}{2} & b & \frac{c_1}{2} & \frac{c_2}{2} & \cdots & c_k & \cdots \\ & \ddots & & \ddots & & & & \\ & & \ddots & & \ddots & & & \\ \frac{c_1}{2} & \frac{c_2}{2} & \cdots & c_k & \cdots & \frac{c_2}{2} & \frac{c_1}{2} & b \end{bmatrix} \quad or \quad \begin{bmatrix} b & \frac{c_1}{2} & \frac{c_2}{2} & \cdots & \frac{c_k}{2} & \frac{c_k}{2} & \cdots & \frac{c_2}{2} & \frac{c_1}{2} \\ \frac{c_1}{2} & b & \frac{c_1}{2} & \frac{c_2}{2} & \cdots & \frac{c_k}{2} & \frac{c_k}{2} & \cdots & \frac{c_2}{2} \\ \frac{c_2}{2} & \frac{c_1}{2} & b & \frac{c_1}{2} & \frac{c_2}{2} & \cdots & \frac{c_k}{2} & \frac{c_k}{2} & \cdots \\ & \ddots & & \ddots & & & & & \\ & & \ddots & & \ddots & & & & \\ \frac{c_1}{2} & \frac{c_2}{2} & \cdots & \frac{c_k}{2} & \frac{c_k}{2} & \cdots & \frac{c_2}{2} & \frac{c_1}{2} & b \end{bmatrix}$$

and z^T denotes the transpose of z. Notice that S is real, symmetric and cyclic, a very special structure caused by the symmetry of the problem.

We now take a step back to consider our results thus far. By using symmetry arguments, we have reduced *"find new stability boundaries"* to *"find r/2 + 2 stability coefficients"*. Once we have found $a, b, c_1, c_2, \ldots, c_k$, the analysis problem is solved up to second order in z. This is a very useful simplification. Furthermore, we can make interesting conclusions based on equation (4.17). Some of these conclusions are listed below:

i. The structure proved above is *independent* of model type, hence it is true for *any* model including dynamical system, imposed sinusoidal motion or CFD models. The only requirement is a $2\pi/r$ rotation symmetry group.

ii. When restricted to zero average, mistuning appears as a second-order effect.

iii. To prove equation (4.17) we assumed a rotational symmetry. However, the second order term, $z^T S z$, also has a sign and reflection symmetry. In other words, $z^T S z$ is invariant under $z \mapsto -z$ and $(z_1, z_2, \ldots, z_r) \mapsto (z_r, z_{r-1}, \ldots, z_2, z_1)$. This implies that (for a zero average mistuning) sign and reflection appear as third-order effects. So there is a hierarchy of stability effects; tuned (average) terms appear in the first order, zero average mistuning is a second-order phenomenon

and mistuning reflection is of third order.

It remains to determine the stability coefficients $a, b, c_1, \ldots, c_k$; we present two methods to do so in the following subsections.

Method A: Computing Eigenvalue Derivatives

Determining $a, b, c_1, \ldots, c_k$ can be easily viewed as a derivative of eigenvalues with respect to parameters problem. The approach below has some nice properties. It only requires information at $z = 0$ (the tuned case) and is easily adjusted for different types of mistuning with a minimum of computation.

Method A is based on *any* discrete blade model (4.6) where the Jacobian

$$M(U, z) \triangleq \frac{\partial \bar{f}}{\partial x}(x_0(U, z), U, z), \tag{4.18}$$

has the property that the quantities

$$\begin{aligned} &M(U_{crit}(0), 0), \quad \frac{\partial M}{\partial z_i}(U_{crit}(0), 0), \quad \frac{\partial^2 M}{\partial z_i \partial z_j}(U_{crit}(0), 0), \\ &\frac{\partial M}{\partial U}(U_{crit}(0), 0), \quad \frac{\partial^2 M}{\partial U^2}(U_{crit}(0), 0), \quad \frac{\partial^2 M}{\partial U \partial z_i}(U_{crit}(0), 0) \end{aligned} \tag{4.19}$$

can be computed (analytically or numerically) for all i and j. Practically, the requirement above is not easily satisfied for complex models (4.6). Specifically, $M(U, z)$ cannot be computed for most computational-fluid-dynamic (CFD) models.

To define $s(z)$ in terms of eigenvalue derivatives, consider the power expansion of $h(U, z)$ (Figure 4.2) about $U_{crit}(0)$ for any z in Ω,

$$\begin{aligned} h(U, z) \;=\; & h(U_{crit}(0), z) + \left[\frac{\partial h}{\partial U}(U_{crit}(0), z)\right](U - U_{crit}(0)) \\ & + \frac{1}{2}\left[\frac{\partial^2 h}{\partial U^2}(U_{crit}(0), z)\right](U - U_{crit}(0))^2 + O(|U - U_{crit}(0)|^3). \end{aligned} \tag{4.20}$$

Figure 4.2 illustrates a case where eigenvalues cross between $U_{crit}(0)$ and $U_{crit}(z)$. However, in Section 4.2.1 we assume that $s(z)$ is smooth for all z in Ω which implies that eigenvalues

cannot cross and (4.20) holds in Ω. Denote partials with respect to U by subscripts,

$$h(z) \triangleq h(U_{crit}(0), z) \tag{4.21}$$

$$h_u(z) \triangleq \frac{\partial h}{\partial U}(U_{crit}(0), z) \tag{4.22}$$

$$h_{uu}(z) \triangleq \frac{\partial^2 h}{\partial U^2}(U_{crit}(0), z) \tag{4.23}$$

By definitions of U_{crit} and s (see equations (4.9) and (4.10)), using (4.21), (4.22), (4.23) and substituting $U = U_{crit}(z)$ into equation (4.20) we obtain

$$0 = h(U_{crit}(z), z) = h(z) + h_u(z)s(z) + \frac{1}{2}h_{uu}(z)s^2(z) + O(\|z\|^3) \tag{4.24}$$

where the error estimate is derived by noting that $s(z) = O(\|z\|)$.

We can apply identical symmetry arguments to $h(z), h_u(z), h_{uu}(z)$ as we applied to $s(z)$, thus

$$h(z) = h(0) + \bar{h}\sum_{i=1}^{r} z_i + z^T H z + O(\|z\|^3) \tag{4.25}$$

$$h_u(z) = h_u(0) + \bar{h}_u\sum_{i=1}^{r} z_i + z^T H_u z + O(\|z\|^3) \tag{4.26}$$

$$h_{uu}(z) = h_{uu}(0) + \bar{h}_{uu}\sum_{i=1}^{r} z_i + z^T H_{uu} z + O(\|z\|^3) \tag{4.27}$$

where $h(0) = 0$, $h_u(0), h_{uu}(0), \bar{h}, \bar{h}_u, \bar{h}_{uu}$ are constant and the constant matrices H, H_u, H_{uu} have the same structure as S—real, symmetric and cyclic.

Substituting (4.17), (4.25),(4.26) and (4.27) into (4.24) yields

$$\left[\bar{h} + ah_u(0)\right]\sum_{i=1}^{r} z_i + z^T\left[H + h_u(0)S + (a\bar{h}_u + a^2 h_{uu}(0)/2)E\right]z + O(\|z\|^3) = 0, \tag{4.28}$$

where E is a full matrix of unit entries which is generated by quadratic cross terms: $(\sum_{i=1}^{r} z_i)^2 =$

$z^T E z$. Equation (4.28) holds for all z in Ω hence

$$\bar{h} + a h_u(0) = 0 \tag{4.29}$$

and by Lemma 4.2.1,

$$H + h_u(0) S + (a\bar{h}_u + a^2 h_{uu}(0)/2) E = 0. \tag{4.30}$$

Lemma 4.2.1 *If $R \in \mathbb{R}^{n \times n}$ is a real symmetric matrix, Γ is any open neighbourhood in $\mathbb{R}^n$ about the origin, then $z^T R z = 0, \forall z \in \Gamma$ if and only if $R = 0$.*

Proof: Assume $P = 0$, clearly $z^T P z = 0$ for all z. Conversely, suppose $z^T P z = 0, \forall z \in \Gamma$ but $P \neq 0$. Since P is symmetric and nonzero, there must exist a real nonzero eigenvalue λ with real eigenvector V. Let $z = V$, scaled suitably so that $z \in \Gamma$. Then $z^T P z = z^T(\lambda z) = \lambda \|z\|^2 \neq 0$, a contradiction. ∎

It is assumed in Section 4.2.1 that $h(U, 0)$ intersects the origin at $U_{crit}(0)$ in a non-degenerate fashion (*not* as shown in Figure 4.3), so $h_u(0) = \partial h(U_{crit}(0), 0)/\partial u$ is non-zero. Therefore,

$$a = -\frac{\bar{h}}{h_u(0)}, \quad S = \frac{1}{h_u(0)} \left(-H + \frac{\bar{h}}{h_u(0)} \left[\bar{h}_u - \frac{\bar{h}\, h_{uu}(0)}{2 h_u(0)} \right] E \right). \tag{4.31}$$

By definition, $h(U, z) = \mathrm{Re}[\lambda_p(U, z)]$ where λ_p is the least stable (maximal real part) eigenvalue of $M(U_{crit}(0), 0)$. It remains the least stable eigenvalue for z in Θ the neighbourhood of interest—no eigenvalue switching as in Figure 4.4. Using definitions (4.21), (4.22), (4.23) and differentiating equations (4.25), (4.26) and (4.27) with respect to z and U yield

equations which hold for any j (by symmetry)

$$\bar{h} = \mathrm{Re}\left[\frac{\partial \lambda_p}{\partial z_j}(U_{crit}(0),0)\right], \tag{4.32}$$

$$\zeta = \mathrm{Re}\left[\frac{\partial^2 \lambda_p}{\partial z_j^2}(U_{crit}(0),0)\right], \tag{4.33}$$

$$\varrho_i = \mathrm{Re}\left[\frac{\partial^2 \lambda_p}{\partial z_j \partial z_{j+i}}(U_{crit}(0),0)\right], \tag{4.34}$$

$$h_u(0) = \mathrm{Re}\left[\frac{\partial \lambda_p}{\partial U}(U_{crit}(0),0)\right], \tag{4.35}$$

$$\bar{h}_u = \mathrm{Re}\left[\frac{\partial^2 \lambda_p}{\partial U \partial z_j}(U_{crit}(0),0)\right], \tag{4.36}$$

$$h_{uu}(0) = \mathrm{Re}\left[\frac{\partial^2 \lambda_p}{\partial U^2}(U_{crit}(0),0)\right], \tag{4.37}$$

where ζ and ϱ_i are the entries of H and appear in the same format as b and c_i, the entries of S in equation (4.17). In the above we can set j to unity for convenience. Substituting equations (4.32) through (4.37) into (4.31) yields expressions for the coefficients $a, b, c_1, \ldots, c_k$ in terms of eigenvalue derivatives,

$$a = -\frac{\{\partial \lambda_p/\partial z_1\}}{\{\partial \lambda_p/\partial U\}}, \tag{4.38}$$

$$b = \frac{1}{\{\partial \lambda_p/\partial U\}}\left(-\left\{\frac{\partial^2 \lambda_p}{\partial z_1^2}\right\} + \frac{\{\partial \lambda_p/\partial z_1\}}{\{\partial \lambda_p/\partial U\}}\left[\left\{\frac{\partial^2 \lambda_p}{\partial U \partial z_1}\right\} - \frac{\{\partial \lambda_p/\partial z_1\}\{\partial^2 \lambda_p/\partial U^2\}}{2\{\partial \lambda_p/\partial U\}}\right]\right), \tag{4.39}$$

$$c_i = \frac{1}{\{\partial \lambda_p/\partial U\}}\left(-\left\{\frac{\partial^2 \lambda_p}{\partial z_1 \partial z_{1+i}}\right\} + \frac{\{\partial \lambda_p/\partial z_1\}}{\{\partial \lambda_p/\partial U\}}\left[\left\{\frac{\partial^2 \lambda_p}{\partial U \partial z_1}\right\} - \frac{\{\partial \lambda_p/\partial z_1\}\{\partial^2 \lambda_p/\partial U^2\}}{2\{\partial \lambda_p/\partial U\}}\right]\right), \tag{4.40}$$

where all derivatives above are evaluated at $(U, z) = (U_{crit}(0), 0)$ and $\{x\}$ denotes the rea part of x. It only remains to actually compute the right-hand sides of equations (4.38 (4.39) and (4.40). These computations are performed using the classic results of Lancaste [Lan64] for the derivatives of eigenvalues with respect to matrix parameters. Specificall the symmetric derivatives can be written as

$$\frac{\partial \lambda_p}{\partial \mu}(U_{crit}(0),0) = \rho_{pp}, \tag{4.41}$$

$$\frac{\partial^2 \lambda_p}{\partial \mu^2}(U_{crit}(0),0) = U_p^T\left[\frac{\partial^2 M}{\partial \mu^2}(U_{crit}(0),0)\right]V_p + 2\sum_k^{\lambda_k \neq \lambda_p} \frac{\rho_{pk}\rho_{kp}}{\lambda_p - \lambda_k} \tag{4.42}$$

where

$$\rho_{ij} = U_i^T[\partial M(U_{crit}(0),0)/\partial\mu]V_j,$$

U_i, V_i are the ith left and right eigenvectors of $M(U_{crit}(0),0)$ and μ can take on the values $z_1, z_2, \ldots, z_r$ or U. Using the chain rule we can derive a formula for asymmetric derivatives,

$$\frac{\partial^2\lambda_p}{\partial\mu\partial\nu}(U_{crit}(0),0) = \frac{1}{2}\left(\frac{\partial^2\lambda_p}{\partial\eta^2}(U_{crit}(0),0) - \frac{\partial^2\lambda_p}{\partial\mu^2}(U_{crit}(0),0) - \frac{\partial^2\lambda_p}{\partial\nu^2}(U_{crit}(0),0)\right) \quad (4.43)$$

where μ and ν can take on values $z_1, z_2, \ldots, z_r$ or U and η is a variation in both μ and ν (set both ν and μ equal to η). This reduces the asymmetric partials to three symmetric partials which can be computed as in equation (4.42). For example, $\partial^2\lambda_p/\partial z_1\partial z_2$ is derived by setting μ to z_1, ν to z_2 and equating z_1 and z_2 to η, then

$$\frac{\partial^2\lambda_p}{\partial\eta^2} = \frac{\partial^2\lambda_p}{\partial z_1^2} + \frac{\partial^2\lambda_p}{\partial z_2^2} + 2\frac{\partial^2\lambda_p}{\partial z_1\partial z_2}. \quad (4.44)$$

Equations (4.41), (4.42) and (4.43) hold when the eigenvalue $\lambda_p(U_{crit}(0),0)$ is simple, meaning that its Jordan block has simple (diagonal) form. In particular, if $\lambda_p(U_{crit}(0),0)$ is distinct, then these equations are valid. We do not consider the non-distinct case since smoothness of $s(z)$ is violated when $\lambda_p(U_{crit}(0),0)$ is non-distinct.

To apply (4.41), (4.42) and (4.43) we need to compute λ_i, U_i and V_i, the eigenvalues and left, right eigenvectors of $M(U_{crit}(0),0)$ for all i. Since $M(U_{crit}(0),0)$ has a block circular structure (equation (3.15)) we can apply Theorem 3.4.1 to compute the eigenvalues and vectors. This provides a significant reduction in computational complexity: instead of solving the $rm \times rm$ eigenvalue/vector problem (m is the number of states per blade) where computation time increases as $(rm)^3$, we solve an $m \times m$ eigenvalue/vector problem r times with resulting computation time rm^3, a savings of r^2. Theorem 3.4.1 also avoids the numerical difficulties inherent in solving eigenvalue/vector problems for matrices with non-distinct eigenvalues.

Method B: Finite Difference

For some models (4.6) it is not possible to compute the quantities (4.19). In particular, it is impractical to compute $M(U,z)$ and its derivatives for computational-fluid-dynamics (CFD) models due to their complexity and large number of states. For that case we suggest the method below.

Given any model (4.6) which can accurately predict $s(z)$ for any given mistuning z, estimate the coefficients $a, b, c_1, \ldots, c_k$ by finite difference. From equation (4.16)

$$a = \frac{\partial s}{\partial z_1}(0) \approx \frac{s(\epsilon, 0, \ldots, 0)}{\epsilon} \tag{4.45}$$

$$b = \frac{1}{2}\frac{\partial^2 s}{\partial z_1^2}(0) \approx \frac{s(2\epsilon, 0, \ldots, 0) - 2s(\epsilon, 0, \ldots, 0)}{2\epsilon^2} \tag{4.46}$$

$$c_i = \frac{\partial^2 s}{\partial z_1 \partial z_{1+i}}(0) \approx \frac{s(\epsilon, 0, \ldots, 0, \epsilon, 0, \ldots, 0) - 2s(\epsilon, 0, \ldots, 0)}{\epsilon^2} \tag{4.47}$$

where in the last equation the second ϵ in $s(\epsilon, 0, \ldots, 0, \epsilon, 0, \ldots, 0)$ appears in the $(i+1)$th spot and ϵ is small. To obtain $a, b, c_1, \ldots, c_k$ we need to run model (4.6) a total of $r/2 + 2$ times so as to form the right-hand side of equations (4.45), (4.46) and (4.47). Once these runs have been completed, the analysis question is solved and the effect of all other types of mistuning is known up to second-order in z. To estimate the required coefficients we need a model that predicts $s(z)$ accurately so that meaningful second order finite differences may be formed. Consequently, the method above is susceptible to numerical noise which may cause large errors when attempting to numerically determine second-order derivatives.

4.2.3 Stability Approximation Summary

We conclude this subsection by summarizing the method of analysis.

i. Find the Jacobian matrix $M(U,z)$, equation (3.12).

ii. Compute the eigenvalues of $M(U,0)$ for $U \in [U_0, U_1]$, the range of interest, by Theorem 3.4.1.

iii. From step ii, construct $h(U,0)$ the maximal real part of eigenvalues at every $U \in [U_0, U_1]$.

iv. Find $U_{crit}(0)$, the point where $h(U,0)$ changes sign. Suggested methods to do so are a bisection algorithm or the Newton-Raphson method.

v. Compute left and right eigenvectors (U_i, V_i) of $M(U_{crit}(0),0)$ using Theorem 3.4.1.

vi. Evaluate equations (4.41),(4.42) and (4.43) as μ and ν vary over $z_1, z_2, \ldots, z_r$ and U.

vii. Substitute the results of step 6 into (4.38), (4.39) and (4.40) to compute the stability coefficients $a, b, c_1, \ldots, c_k$.

Notice that all steps above only require information at the tuned point $z = 0$.

4.3 Forced Response Approximation

To compute the forced response we use an eigenvalue/vector perturbation scheme. This method is valuable for two reasons: first it allows for a large region of method validity as in the forthcoming Example 4.3.1, second it states the forced response solution in terms of eigenvalues and eigenvectors providing a link to familiar concepts in linear systems. The basic idea is very simple: we write the response in terms of eigenvalues and eigenvectors, this allows an approximation of the mistuned response by perturbation of the eigenvalues and eigenvectors about the tuned point.

4.3.1 Perturbation Comparison

To motivate the chosen method we compare two methods of approximating the inverse matrix $A^{-1}(z) = [i\omega I - M(z)]$. Method one is a series expansion whose variations are used in much of the mode localization literature (for example [Sin86]). Method two is based on eigenvalue/vector perturbations and is developed in here.

Series approximation

If the spectral radius of matrix P is less than one, $\rho(P) < 1$, meaning that all eigenvalues of P lie within the open unit disc, $|\lambda| < 1$, then the following series converges

$$[I + P]^{-1} = I - P + P^2 - P^3 + \cdots \tag{4.48}$$

Series (4.48) may be used to approximate the inverse of matrix $A(z) = [i\omega I - M(z)]$ in equation (4.5). In shorthand, let $A_0 = A(0)$ and $\Delta A_z = A(z) - A(0)$, then

$$\begin{aligned} A^{-1}(z) &= [A_0 + \Delta A_z]^{-1} \\ &= [A_0(I + A_0^{-1}\Delta A_z)]^{-1} \\ &= [I + A_0^{-1}\Delta A_z]^{-1}A_0^{-1} \\ &= [I - A_0^{-1}\Delta A_z + (A_0^{-1}\Delta A_z)^2 - \cdots]A_0^{-1} \end{aligned} \tag{4.49}$$

which converges if and only if $\rho(A_0^{-1}\Delta A_z) < 1$. A fundamental problem is that A_0 is almost singular. Engines have light damping, $\mathrm{Re}[\lambda_j(z)] \approx 0$, and can be forced near resonance, $\omega \approx \mathrm{Im}[\lambda_j(z)]$. Hence $A(z)$ can have an almost zero eigenvalue: $i\omega - \lambda_j(z) \approx 0$. Consequently, A_0^{-1} is very large, and so $\rho(A_0^{-1}\Delta A_z) < 1$ only allows very small matrices ΔA_z and hence only a small range of z is permitted. Thus, the series method has a tiny region of validity when the system is lightly damped and forced close to resonance—as is the case in turbomachines.

Eigenvalue/vector approximation

Alternatively, the inverse matrix $A^{-1}(z)$ can be written as

$$A^{-1}(z) = [i\omega I - M(z)]^{-1} = T(z)[i\omega I - \Lambda(z)]^{-1}T^{-1}(z) \tag{4.50}$$

where

$$[i\omega I - \Lambda(z)]^{-1} = \begin{bmatrix} \frac{1}{i\omega - \lambda_1(z)} & & 0 \\ & \ddots & \\ 0 & & \frac{1}{i\omega - \lambda_n(z)} \end{bmatrix}. \tag{4.51}$$

Here $\lambda(z), T(z)$ and $T^{-1}(z)$ are the eigenvalues and right/left eigenvectors of linearization $M(z)$. By approximating eigenvalues $\lambda(z)$ we can easily capture matrix (4.51), even when $A(z)$ is almost singular: $i\omega - \lambda_j(z) \approx 0$.

A fundamental limitation of this method is eigenvalue collision. When eigenvalues are indistinct, $\lambda_j(z) = \lambda_i(z)$, eigenvectors become discontinuous and the eigenvector perturbations of Section 4.3 fail. If $M(0)$ has almost indistinct eigenvalues, then small z may cause these eigenvalues to collide on some surface which passes close to the origin and our perturbation technique (which begins at the origin $z = 0$) will not be able to see close to or past this surface. A concrete example of this phenomena is demonstrated in Example 4.3.1.

As noticed by Mignolet, Hu [MH97] and others, it is difficult to check the series convergence condition $\rho(A_0^{-1}\Delta A_z) < 1$ for general matrices A_0 as a function of mistuning z. It is even more difficult to check the distinct condition of the eigenvalue/vector method. However, this does not prevent us from checking these conditions for a simple example. We do so below and note that method limitations revealed by the example generalize to arbitrary linear systems.

Example: Series versus Eigenvalue/vector Convergence

Take the simplest possible case: two blades, $r = 2$, with one state per blade, $m = 1$. Pick the following matrix $A(z) = [i\omega I - M(z)]$ with symmetry (3.13),

$$A(z) = \begin{bmatrix} a + z_1 & b + z_2 \\ b + z_1 & a + z_2 \end{bmatrix} \tag{4.52}$$

where coefficient a may be complex (it depends on $i\omega$) but z_1, z_2 and b are real. Matrix (4.52) has eigenvalues

$$\lambda_1(z) = a - b, \qquad \lambda_2(z) = a + b + z_1 + z_2 \tag{4.53}$$

with right (column) eigenvectors

$$V_1(z) = \begin{bmatrix} b + z_2 \\ -b - z_1 \end{bmatrix} \qquad V_2(z) = \begin{bmatrix} 1 \\ 1 \end{bmatrix} \tag{4.54}$$

and left (row) eigenvectors

$$U_1(z) = \frac{[1, -1]}{2b + z_1 + z_2}, \qquad U_2(z) = \frac{[b + z_1, b + z_2]}{2b + z_1 + z_2}. \tag{4.55}$$

The inverse of $A(z)$ is given by

$$A^{-1}(z) = \frac{1}{(a - b)(a + b + z_1 + z_2)} \begin{bmatrix} a + z_2 & -b - z_2 \\ -b - z_1 & a + z_1 \end{bmatrix}. \tag{4.56}$$

We see immediately that $A^{-1}(z)$ has a steep nonlinear dependence on z if $a + b \approx 0$, precisely if $A(0)$ has an eigenvalue close to zero: $\lambda_2(0) \approx 0$.

It is simple to check convergence conditions of the series and eigenvalue/vector methods for this example. Matrix $A_0^{-1}\Delta A_z$ in (4.49) has eigenvalues

$$\zeta_1 = 0 \qquad \zeta_2 = \frac{z_1 + z_2}{a + b}.$$

Hence the condition for convergence of the series method is given by

$$\rho(A_0^{-1}\Delta A_z) < 1 \iff |z_1 + z_2| < |a + b|. \tag{4.57}$$

Expression (4.57) is a conservative guarantee that $\lambda_2(z) \neq 0$ in (4.53).

On the other hand, our eigenvalue/vector perturbation which begins at the origin, $z = 0$,

will not be able to see across the $1/(2b+z_1+z_2)$ singularity in the eigenvectors (4.55). Hence the eigenvalue/vector method only converges if

$$\begin{aligned} z_1+z_2 &> -2b \qquad \text{when } b \geq 0 \\ z_1+z_2 &< -2b \qquad \text{when } b < 0, \end{aligned} \tag{4.58}$$

where b is real. This is exactly the point where eigenvalues become indistinct,

$$\lambda_2(z) - \lambda_1(z) = 2b + z_1 + z_2 = 0.$$

If $A(0)$ is almost singular ($\lambda_2(0) = a + b \approx 0$) but the eigenvalues are far from being indistinct ($\lambda_1(0) - \lambda_2(0) = 2b \not\approx 0$), then the series approximation has a tiny sliver of convergence while the eigenvalue/vector method has a large region of convergence—Figure 4.5. (Shading denotes regions where (4.57) or (4.58) fail and methods do not converge.) This is a case we expect to see in practice: light-damping and near resonance (almost singular) with significant blade coupling (eigenvalues far apart).

For the contrary case: almost indistinct eigenvalues ($\lambda_1(0)-\lambda_2(0) = 2b \approx 0$) but far from singularity ($\lambda_1(0), \lambda_2(0) \not\approx 0$ hence $a \approx 0$) the series method is good and the eigenvalue/vector method is bad—Figure 4.6. This is not an interesting case: large-damping or no resonance (far from singularity) indicates a conservative design where mistuning will have no impact.

For the case where we have both indistinct and almost singular eigenvalues, ($\lambda_1(0) \approx \lambda_2(0) \approx 0$ or $a \approx b \approx 0$) both methods are poor—Figure 4.7. This case can be encountered practically. For example: fans with stiff hubs (small structural coupling), complex blade shapes and small aerodynamic coupling can exhibit many closely-spaced, lightly-damped modes.

It should be noted that variations and enhancements on the series method will still be poor in the almost singular case. Fundamentally it is not possible to approximate the (multi variable) discontinuous function $1/[i\omega - \lambda_j(z)]$ by a smooth polynomial expression

$$\frac{1}{i\omega - \lambda_j(z)} \approx a_0 + a_1 \cdot z + z^T A_2 z + \cdots$$

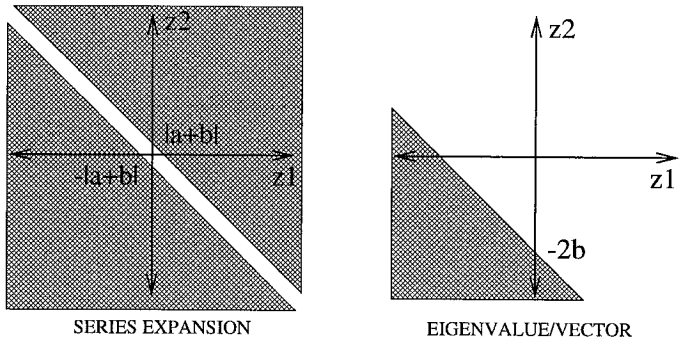

Figure 4.5: Method convergence: almost singular case.

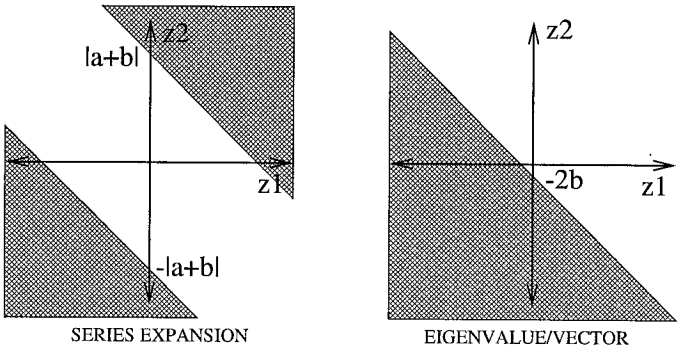

Figure 4.6: Method convergence: almost indistinct case.

in a substantial region of z space when $i\omega - \lambda_j(0)$ is small. Yet it is possible to achieve an approximation that holds over a large region with only a few terms by approximating $\lambda_j(z)$ in the denominator (matching two similar discontinuous functions). The functional form $1/[i\omega - \lambda_j(z)]$ yields the required steep nonlinear dependence on mistuning.

In summary, Table 4.1 follows from equations (4.50), (4.51) and the example. The light-damping limitation of the series method is also noted in [WP90]. By comparison, the eigenvalue/vector method holds in the lightly-damped resonant case, but fails if we have closely

	Low Damping	High Damping
Distant Eigenvalues	**Sensitive to Mistuning**	**Not Sensitive to Mistuning**
	Eigen Approx. $\surd$	Eigen Approx. $\surd$
	Series Method $\times$	Series Method $\surd$
Nearby Eigenvalues	**Sensitive to Mistuning**	**Not Sensitive to Mistuning**
	Eigen Approx. $\times$	Eigen Approx. $\times$
	Series Method $\times$	Series Method $\surd$

Table 4.1: Perturbation method validity.

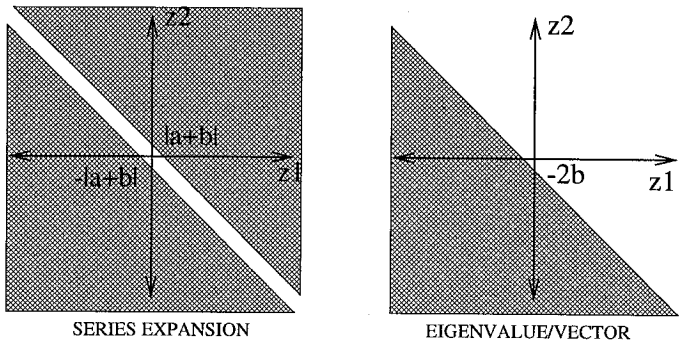

Figure 4.7: Method convergence: almost singular and indistinct.

spaced modes. Of course symmetry arguments along with equations (4.50) and (4.51) continue to hold. To extend the eigenvalue/vector method to the nearby eigenvalues case requires the tracking of sharply veering eigenvalues and eigenvectors.

4.3.2 Jordan Decomposition

Forced response X in the frequency domain is given by expression (4.5) rewritten below as

$$X(z) = A^{-1}(z)B_\ell(z) \tag{4.59}$$

where $A(z) = [i\omega I - M(z)]$. To develop a simple functional form for $X(z)$ we have to approximate the inverse matrix $A^{-1}(z)$ which we do by bringing together the symmetry tools of Section 3 together with eigenstructure perturbation concepts below.

Assume the tuned linearization matrix $\bar{M} = M(0)$ of (3.15) has distinct eigenvalues. This is true generically (almost always); as discussed in Section 3.6.1. Then $M(z)$ has a diagonal Jordan form where the eigenvalues and eigenvectors vary smoothly with z; see [Lan64],

$$M(z) = T(z)\Lambda(z)T^{-1}(z) = \begin{bmatrix} | & & | \\ V_1(z) & \cdots & V_n(z) \\ | & & | \end{bmatrix} \begin{bmatrix} \lambda_1(z) & & 0 \\ & \ddots & \\ 0 & & \lambda_n(z) \end{bmatrix} \begin{bmatrix} - & U_1(z) & - \\ & \vdots & \\ - & U_n(z) & - \end{bmatrix}. \tag{4.60}$$

Here $\Lambda(z)$ is a diagonal matrix of eigenvalues and $T(z), T^{-1}(z)$ are matrices of right and left

eigenvectors respectively. Let the right eigenvectors $V_j(z)$ be normalized as $\|V_j(0)\| = 1$ for any j. By definition $A(z) = T(z)[i\omega I - \Lambda(z)]T^{-1}(z)$, and so the inverse matrix $A^{-1}(z)$ is given by

$$A^{-1}(z) = [i\omega I - M(z)]^{-1} = T(z)[i\omega I - \Lambda(z)]^{-1}T^{-1}(z) \tag{4.61}$$

where

$$[i\omega I - \Lambda(z)]^{-1} = \begin{bmatrix} \frac{1}{i\omega - \lambda_1(z)} & & 0 \\ & \ddots & \\ 0 & & \frac{1}{i\omega - \lambda_n(z)} \end{bmatrix}. \tag{4.62}$$

Expression (4.61) may be rewritten

$$A^{-1}(z) = \sum_{q=1}^{n} \frac{1}{i\omega - \lambda_q(z)} \underbrace{\begin{bmatrix} | \\ V_q(z) \\ | \end{bmatrix} [-\ U_q(z)\ -]}_{n \times n \text{ complex matrix}} \tag{4.63}$$

where $n = rm$. Using equation (4.63) we will find an approximation for the inverse matrix $A^{-1}(z)$, and hence the forced response $X(z)$, by perturbing the eigenvalue $\lambda(z)$ and left, right eigenvectors $U(z), V(z)$ about the tuned point $z = 0$.

4.3.3 Response per Mode with Symmetry

Now consider forced response $X^{j,d}(z)$ due to a single mode j, d (numbering of Theorem 3.4.1). From equations (4.59) and (4.63) we have

$$X^{j,d}(z) = \frac{V_j^d(z)U_j^d(z)B_\ell(z)}{i\omega - \lambda_j^d(z)} \tag{4.64}$$

where the response for all modes is given by

$$X(z) = \sum_{j=0}^{r-1} \sum_{d=1}^{m} X^{j,d}(z). \tag{4.65}$$

Recall that $V_j^d(z), U_j^d(z)$ and $B_\ell(z)$ have the symmetries of Table 3.1, these imply

$$U_j^d(z) = \left[u_j^d(z),\ p_j^{-1}u_j^d(\varphi z),\ p_j^{-2}u_j^d(\varphi^2 z),\ \cdots,p_j^{-r+1}u_j^d(\varphi^{r-1}z)\right]$$

$$V_j^d(z) = \begin{bmatrix} v_j^d(z) \\ p_j v_j^d(\varphi z) \\ p_j^2 v_j^d(\varphi^2 z) \\ \vdots \\ p_j^{r-1} v_j^d(\varphi^{r-1} z) \end{bmatrix}, \qquad B_\ell(z) = \begin{bmatrix} \beta(z) \\ p_\ell \beta(\varphi z) \\ p_\ell^2 \beta(\varphi^2 z) \\ \vdots \\ p_\ell^{r-1} \beta(\varphi^{r-1} z) \end{bmatrix} \tag{4.66}$$

where $v_j^d(z), u_j^d(z)$ and $\beta(z)$ correspond to the first (m sized) block of $V_j^d(z), U_j^d(z)$ and $B_\ell(z)$, respectively.

Equation (4.66) allows us to write the response of the first blade (first block of $X^{j,d}(z)$ in (4.64)) as

$$X_1^{j,d}(z) = \frac{1}{i\omega - \lambda_j^d(z)} \left\{ \sum_{s=0}^{r-1} p_{\ell-j}^s \left(\begin{bmatrix} - & u_j^d(\varphi^s z) & - \end{bmatrix} \begin{bmatrix} | \\ \beta(\varphi^s z) \\ | \end{bmatrix} \right) \right\} \begin{bmatrix} | \\ v_j^d(z) \\ | \end{bmatrix}. \tag{4.67}$$

Equation (4.67) is a great simplification, it reduces computing the forced response $X(z)$ from an rm-sized vector problem to a first-blade m-sized problem. Response of the first blade due to all modes follows from (4.65),

$$X_1(z) = \sum_{j=0}^{r-1} \sum_{d=1}^{m} X_1^{j,d}(z). \tag{4.68}$$

Subsequent response for all blades is given by symmetry (3.23),

$$X(z) = \left[X_1(z),\ p_\ell X_1(\varphi z),\ p_\ell^2 X_1(\varphi^2 z),\ \cdots,p_\ell^{r-1} X_1(\varphi^{r-1} z)\right]. \tag{4.69}$$

Intuitively, if we want to know the response of blade three to some mistuning pattern z, we rotate z back twice ($\varphi^2 z$) and evaluate the response of blade one ($X_1(\varphi^2 z)$). Then the response of blade three is the same, modulo the required phase shift p_ℓ^2 due to the relative position of the stationary forcing.

4.3.4 Tuned Response

When the system is tuned ($z = 0$) equation (4.68) reduces to

$$X_1(0) = r \sum_{d=1}^{m} \frac{u_L^d(0)\beta(0)}{i\omega - \lambda_L^d(z)} \begin{bmatrix} | \\ v_L^d(0) \\ | \end{bmatrix} \tag{4.70}$$

where $L = \ell \bmod r$. For example: if $r = 10$ and $\ell = 12$ (meaning $\zeta(\theta) = \sin(12\,\theta)$ in Figure 3.1) then only $j = L = 2$ modes will appear in (4.70). Hence forcing modes separated by r (say $\ell = 2$ and $\ell = r + 2$) have the same spatial structure (same symmetry of forcing vector $B_\ell(z)$) but differ in forcing frequency $\omega = \Omega\ell$. In fact the modes of (4.70) are precisely the modes which are fixed in the stationary frame. Suppose we have an observer at position θ in the stationary frame. At some time t blade one travels past with amplitude

$$\bar{x}_1(0,t) = X_1(0)e^{i\ell\Omega t},$$

at the earlier time $t - \tau = t - 2\pi/r\Omega$ the second blade had arrived with equal amplitude

$$\begin{aligned}
\bar{x}_2(0, t-\tau) &= X_2(0)e^{i\ell\Omega(t-\tau)} \\
&= p_\ell X_1(0)e^{i\ell\Omega(t-\tau)} && \text{symmetry (3.23)} \\
&= p_\ell X_1(0)e^{i(\ell\Omega t - 2\pi\ell/r)} && \text{definition of } \tau \\
&= X_1(0)e^{i\ell\Omega t} && \text{definition of } p_\ell.
\end{aligned}$$

Consequently, the tuned response $\bar{x}(0,t) = X(0)e^{i\ell\Omega t}$ is stationary in the disturbance reference frame. This is true for any stationary forcing (combination of many ℓs above) and is not a surprising conclusion.

In contrast, the mistuned response, $\bar{x}(z,t) = X(z)e^{i\ell\Omega t}$ with $z \neq 0$, can display all modes (allows $j \neq \ell \bmod r$ modes) and is not stationary in the disturbance reference frame, here

$$\bar{x}_1(z,t) = X_1(z)e^{i\ell\Omega t},$$

but

$$\begin{aligned}
\bar{x}_2(z,t-\tau) &= X_2(z)e^{i\ell\Omega(t-\tau)} \\
&= p_\ell X_1(\varphi z)e^{i\ell\Omega(t-\tau)} \\
&= X_1(\varphi z)e^{i\ell\Omega t} \\
&\neq X_1(z)e^{i\ell\Omega t} = \bar{x}_1(z,t).
\end{aligned}$$

Think of a fan with all rigid blades except one flexible or mistuned blade. Since only the flexible blade may vibrate, it is clear that the response is anything but stationary in the fixed reference frame.

Geometric Interpretation

Statements above can also be seen geometrically: $y = T^{-1}(z)\,x$ is the change of coordinates which transforms equation (4.3) into diagonal form

$$\dot{y} = \Lambda(z)\,y + T^{-1}(z)B_\ell(z)e^{i\omega t}. \tag{4.71}$$

Now $T^{-1}(z)B_\ell(z)$ is the projection of the forcing vector $B_\ell(z)$ into the diagonal coordinate system. The matrix $T^{-1}(z)$ consists of left eigenvectors $U_j^d(z)$ of $M(z)$. When the system is

tuned $B_\ell(0)$ lines up with the Lth right eigenvector block $V_L^d(0)$

$$V_L^d(0) = [v,\ p_\ell\, v,\ p_\ell^2\, v,\ \cdots\ , p_\ell^{r-1}\, v] \tag{4.72}$$

$$B_\ell(0) = [\beta,\ p_\ell\, \beta,\ p_\ell^2\, \beta,\ \cdots\ , p_\ell^{r-1}\, \beta]. \tag{4.73}$$

More precisely, $B_\ell(0)$ projects onto a subspace defined by the span of $V_L^d(0)$ as d varies between 1 and m. So the only nontrivial equations in (4.71) are those corresponding to the Lth modes

$$\dot{y}_j^d = \lambda_j^d(0) y_j^d, \qquad \text{for } j \neq L, \tag{4.74}$$

$$\dot{y}_L^d = \lambda_L^d(0) y_L^d + U_L^d(0) B_\ell(0) e^{i\omega t}. \tag{4.75}$$

As z is varied away from zero, the eigenvectors $V(z), U(z)$ shift and the Lth right eigenvector subspace drops away from the forcing vector $B_\ell(z)$. For the mistuned case $B_\ell(z)$ has a projection onto all eigenvectors, the structure (4.74), (4.75) fails and all modes come into play. The amount by which any specific mode shape $V_j^d(z)$ appears is determined by the size of projection $U_j^d(z)B_\ell(z)$ scaled by the inverse eigenvalue $\mu_j^d(z) = 1/[i\omega - \lambda_j^d(z)]$, precisely the scalar term $U_j^d(z)B_\ell(z)/[i\omega - \lambda_j^d(z)]$ in equation (4.64). Consequently, lightly-damped modes close to resonance will appear far more readily with mistuning than highly-damped modes forced far from resonance.

4.3.5 Eigenstructure Approximations

So far we have not made any approximations, so the modal expression of (4.67), (4.68) and (4.69) is an exact solution to the linear forced response problem (4.5). An obvious first cut approximation is to drop all highly damped modes. In this case summation (4.68) is only taken over $j = \ell \bmod r$ (the tuned modes) plus any additional mistuned modes j, d which satisfy

$$|\,\mathrm{Re}[\lambda_j^d(0)]\,| < \delta \implies |\mu_j^d(0)| = \frac{1}{|i\omega - \lambda_j^d(0)|} > \frac{1}{\delta} \tag{4.76}$$

where $1/\delta$ is the (roughly) desired accuracy. Equation (4.76) is a useful estimate, yet it does not address our primary goal of expressing (4.67) as a simple functional form in z. To do so we turn to standard tools in eigenvalue and eigenvector perturbation.

Inverse Eigenvalue Perturbation

We need to approximate the term

$$\mu_j^d(z) = \frac{1}{i\omega - \lambda_j^d(z)} \tag{4.77}$$

in equation (4.67). Here $\mu_j^d(z)$ is an eigenvalue of $A^{-1}(z)$ and $\lambda_j^d(z)$ is an eigenvalue of $M(z)$. Eigenvalues $\lambda_j^d(z)$ are approximated by methods analogous to those of Section 4.2.2. Remember that eigenvalue $\lambda_j^d(z)$ has symmetry

$$\lambda_j^d(z) = \lambda_j^d(\varphi z)$$

and so is invariant under rotation (see Lemma 3.6.1). Invariance under rotation implies (by the same symmetry argument as used to derive equation (4.16))

$$\begin{aligned}
\lambda_j^d(z) &= \lambda_j^d(0) + \sigma_{j,d}(z_1 + z_2 + \cdots + z_r) \\
&+ \phi_{j,d}(z_1^2 + z_2^2 + \cdots + z_r^2) \\
&+ \psi_1^{j,d}(z_1 z_2 + z_2 z_3 + \cdots + z_r z_1) \\
&+ \psi_2^{j,d}(z_1 z_3 + z_2 z_4 + \cdots + z_r z_2) \\
&\vdots \qquad\qquad \vdots \\
&+ \psi_k^{j,d}(z_1 z_{1+k} + z_2 z_{2+k} + \cdots + z_r z_k) + O(\|z\|^3) \\
&= \lambda_j^d(0) + \sigma_{j,d} \sum_{i=1}^{r} z_i + z^T[\Phi_{j,d}]z + O(\|z\|^3).
\end{aligned} \tag{4.78}$$

where k is given by

$$k \triangleq \begin{cases} \frac{r}{2} & r \text{ even} \\ \frac{r-1}{2} & r \text{ odd.} \end{cases} \tag{4.79}$$

Notice that the linear term $\sigma \sum_{i=1}^{r} z_i$ does not capture mistuning dependence, it only reacts to the averaged or tuned $\sum_{i=1}^{r} z_i$ portion. It is the quadratic term $z^T \Phi z$ which really reveals eigenvalue motion as a function of mistuning and captures motion due to zero average mistuning: $\sum_{i=1}^{r} z_i = 0$. Since $\mu(z)$ in (4.77) can depend strongly on $\lambda(z)$, it is crucial to capture this second order eigenvalue dependence on mistuning given by $z^T \Phi z$.

Differentiating (4.78) shows that coefficients $\sigma, \phi, \psi_1, \cdots, \psi_k$ correspond to eigenvalue derivatives

$$\sigma_{j,d} = \frac{\partial \lambda_j^d}{\partial z_1}(0), \quad \phi_{j,d} = \frac{1}{2} \frac{\partial^2 \lambda_j^d}{\partial z_1^2}(0), \quad \psi_i^{j,d} = \frac{\partial^2 \lambda_j^d}{\partial z_1 \partial z_{1+i}}(0). \tag{4.80}$$

These eigenvalue derivatives with respect to parameters are computed as in Section 4.2.2. This yields an approximation for the $1/[i\omega - \lambda_j^d(z)]$ term in equation (4.67) by approximating eigenvalue $\lambda_j^d(z)$ in the denominator of (4.77).

Coupling Approximation

Our next goal is to approximate the remainder of expression (4.67), namely find an approximation for the coupling term

$$\Psi_j^d(z) = \left(\sum_{s=0}^{r-1} p_{\ell-j}^s u_j^d(\varphi^s z) \beta(\varphi^s z) \right) v_j^d(z). \tag{4.81}$$

Consequently, (4.67) may be rewritten as $X_1^{j,d}(z) = \mu_j^d(z) \Psi_j^d(z)$. The term Ψ varies slowly with z—eigenvectors change slowly unless eigenvalues are clustered because rate equations like (4.84) always depend on eigenvalue distance $\lambda_j - \lambda_p$ in the denominator. Consequently, it is acceptable to approximate $\Psi(z)$ as a first order function in z.

Equation (4.81) can be further split into two parts: the summation

$$g_j^d(z) = \sum_{s=0}^{r-1} p_{\ell-j}^s u_j^d(\varphi^s z)\beta(\varphi^s z) \tag{4.82}$$

and the first block $v_j^d(z)$ of right eigenvector $V_j^d(z)$. So $\Psi_j^d(z) = g_j^d(z)v_j^d(z)$ where $g_j^d(z)$ is a scalar function and $v_j^d(z) \in \mathbb{C}^m$.

Right Eigenvector Perturbation: We linearly approximate $v_j^d(z)$ found in (4.81) by

$$v_j^d(z) \approx \left[v_j^d(0)\right] + \left[\frac{\partial v_j^d}{\partial z_1}(0)\right] z_1 + \left[\frac{\partial v_j^d}{\partial z_2}(0)\right] z_2 + \cdots + \left[\frac{\partial v_j^d}{\partial z_r}(0)\right] z_r. \tag{4.83}$$

Since $v_j^d(0)$ corresponds to the first block of tuned right eigenvector $V_j^d(0)$ it may be computed from Theorem 3.4.1. The required eigenvector derivatives are given by formulas similar to those in [Lan64],

$$\frac{\partial v_j^d}{\partial z_i}(0) = \sum_{p,s \neq j,d} \left(\frac{U_p^s(0) \left[\frac{\partial M}{\partial z_i}(0)\right] V_j^d(0)}{\lambda_j^d(0) - \lambda_p^s(0)} \right) v_p^s(0). \tag{4.84}$$

As in the eigenvalue perturbation, all we need to do is compute the tuned eigenvalues and right, left eigenvectors, $\lambda(0), U(0)$ and $V(0)$, which substitute into equations (4.83) and (4.84) to yield a linear approximation for $v_j^d(z)$. If desired, one may make a further approximation by dropping from summation (4.84) any mode p, s which is far from target mode j, d, $|\lambda_j^d(0) - \lambda_p^s(0)|$ large.

Summation Approximation: It remains to approximate the summation term $g_j^d(z)$ of equation (4.82). It is easy to show that $g_j^d(z)$ has symmetry

$$g_j^d(\varphi z) = p_{j-\ell}\, g_j^d(z). \tag{4.85}$$

Symmetry (4.85) implies that $g_j^d(z)$ has the form

$$g_j^d(z) = g_j^d(0) + \bar{g}_j^d(z_1 + p_{\ell-j}\, z_2 + p_{\ell-j}^2\, z_3 + \cdots + p_{\ell-j}^{r-1}\, z_r) + O(\|z\|^2). \tag{4.86}$$

To complete a first order approximation of $g_j^d(z)$, we need only find the complex coefficients $g_j^d(0)$ and $\bar{g}_j^d$. The tuned portion $g_j^d(0)$ is computed from (4.82) and Theorem 3.4.1,

$$\begin{aligned} g_j^d(0) &= 0 \qquad \text{for } j \neq L \\ g_L^d(0) &= r u_L^d(0)\beta(0). \end{aligned} \tag{4.87}$$

Coefficient $\bar{g}_j^d$ is obtained by differentiating (4.82) and (4.86) with respect to z_1,

$$\bar{g}_j^d = \frac{\partial g_j^d}{\partial z_1}(0) = \sum_{s=0}^{r-1} p_{\ell-j}^s \left(\left[\frac{\partial u_j^d}{\partial z_{1-s}}(0) \right] [\beta(0)] + [u_j^d(0)] \left[\frac{\partial \beta}{\partial z_{1-s}}(0) \right] \right). \tag{4.88}$$

It remains to find left eigenvector derivatives with respect to parameters, $\partial u/\partial z_i$, and as in the right eigenvector case this is done by standard methods as in [Lan64]. Analogous to equation (4.84) we have

$$\frac{\partial u_j^d}{\partial z_i}(0) = \sum_{p,s \neq j,d} \left(\frac{U_j^d(0) \left[\frac{\partial M}{\partial z_i}(0) \right] V_p^s(0)}{\lambda_j^d(0) - \lambda_p^s(0)} \right) u_p^s(0). \tag{4.89}$$

and once more we need only find the tuned eigenvalue and left, right eigenvectors, $\lambda(0), U(0)$ and $V(0)$, from Theorem 3.4.1 to complete the calculation.

Combining Terms

Combining linear approximations for $v_j^d(z)$ (equations (4.83) and (4.84)) and $g_j^d(z)$ (equations (4.86), (4.87), (4.88) and (4.89)) yields a linear approximation for coupling term $\Psi_j^d(z)$ of

equation (4.81),

$$\Psi_j^d(z) = g_j^d(z)v_j^d(z) = \begin{bmatrix} | \\ \alpha_0^{j,d} \\ | \end{bmatrix} + \begin{bmatrix} | \\ \alpha_1^{j,d} \\ | \end{bmatrix} z_1 + \begin{bmatrix} | \\ \alpha_2^{j,d} \\ | \end{bmatrix} z_2 + \cdots + \begin{bmatrix} | \\ \alpha_r^{j,d} \\ | \end{bmatrix} z_r + O(\|z\|^2), \tag{4.90}$$

where $\alpha_i^{j,d}$ are known, constant, complex, m sized, column vectors. Recall that the forced response of blade one, $X_1^{j,d}(z)$, due to the j,dth mode is taken from (4.67) and (4.81),

$$X_1^{j,d}(z) = \frac{\Psi_j^d(z)}{i\omega - \lambda_j^d(z)}. \tag{4.91}$$

Here inverse eigenvalue $1/[i\omega - \lambda_j^d(z)]$ of equation (4.77) is accurately captured by approximation (4.78) of $\lambda_j^d(z)$ in the denominator. Approximation (4.90) together with the denominator approximation of eigenvalue $\lambda_j^d(z)$ as above yields the approximate forced response of blade one due to mode j,d,

$$X_1^{j,d}(z) \approx \frac{\alpha_0^{j,d} + \alpha_1^{j,d}z_1 + \alpha_2^{j,d}z_2 + \cdots + \alpha_r^{j,d}z_r}{i\omega - \lambda_j^d(0) - \sigma_{j,d}\sum_{i=1}^r z_i - z^T[\Phi_{j,d}]z}. \tag{4.92}$$

In cleaner notation (drop all j,d indexing), the approximate response of blade one due to a single mode is given by

$$X_1^{j,d}(z) \approx \frac{\alpha_0 + \alpha_1 z_1 + \alpha_2 z_2 + \cdots + \alpha_r z_r}{i\omega - \lambda(0) - \sigma\sum_{i=1}^r z_i - z^T\Phi z}. \tag{4.93}$$

Here α_i are known, constant, m sized vectors; $\omega = \ell\Omega$ is the forcing frequency; $\lambda(0)$ is an eigenvalue of tuned linearization matrix $M(0)$; a is a known complex coefficient; and Φ is a known complex matrix containing coefficients $\phi, \psi_1, \cdots, \psi_k$ as in (4.78). Further, it follows from (4.87) that $\alpha_0^{j,d} = 0$ if $j \neq \ell \bmod r$ since $\alpha_0^{j,d}$ corresponds to the tuned portion of the response. An approximation for the total response of blade one follows from (4.68) and

(4.92)

$$X_1(z) = \sum_{j=0}^{r-1}\sum_{d=1}^{m} X_1^{j,d}(z) \approx \sum_{j=0}^{r-1}\sum_{d=1}^{m} \frac{\alpha_0^{j,d} + \alpha_1^{j,d} z_1 + \alpha_2^{j,d} z_2 + \cdots + \alpha_r^{j,d} z_r}{i\omega - \lambda_j^d(0) - \sigma_{j,d}\sum_{i=1}^{r} z_i - z^T[\Phi_{j,d}]z}. \tag{4.94}$$

In addition, we can drop terms in (4.94) which correspond to highly damped modes. In that case the summation is taken over all tuned modes with $j = \ell \bmod r$ plus those that satisfy (4.76). Finally, the response for all blades is given by symmetry (4.69).

Our analysis goal has now been achieved. Equations (4.92), (4.94) and (4.69) provide a simple functional form in z for forced response $X(z)$. Once we have computed coefficients α_i, σ and $\phi, \psi_1, \cdots, \psi_k$ of matrix Φ for all desired modes, we know the forced response for arbitrary mistuning. More importantly, functional form (4.92), (4.94) and (4.69) allows for an intuitive understanding of the mode localization problem and permits sensitivity or tradeoff studies as in Section 5.2.1.

4.3.6 Forced Response Approximation Summary

To close this section we present a short summary of the forced response analysis method.

1. Start with any nonlinear model (3.1) which necessarily has symmetry (3.5).

2. Pick appropriate equilibrium point $x^*(z)$ which has symmetry of Lemma 3.3.2. (See Section 4.1 for discussion.)

3. Compute linearization matrix $M(z)$ and forcing vector $B_\ell(z)$ of (4.3) about chosen equilibrium $x^*(z)$. See Sections 4.1. Can consider one forcing mode ℓ at a time by linearity.

4. Check stability as in Section 4.2.2 to insure forced response is meaningful. Transforming to frequency domain yields the linear forced response problem (4.5) for any loading.

5. Solve for eigenvalues, $\lambda(0)$, and right, left eigenvectors, $V(0), U(0)$, of tuned matrix $\bar{M} = M(0)$ in equation (3.15) by Theorem 3.4.1.

6. Use $\lambda(0), U(0)$ and $V(0)$ as in Section 4.2.2 to compute eigenvalue perturbation for $\lambda(z)$ of equation (4.78). This approximates eigenvalues $\mu(z)$ of inverse matrix $A^{-1}(z) = [i\omega I - M(z)]^{-1}$ in the denominator through expression (4.77). Further substitute values of $\lambda(0), U(0)$ and $V(0)$ into (4.84) and (4.89) to compute (4.83), (4.86) and (4.88) which together yield $\Psi(z)$ of (4.90). Combine $\Psi(z)$ of (4.90) and $\mu(z)$ of (4.77) to find first blade approximation (4.91) and (4.92) for any given mode j, d.

7. Sum over tuned modes, $j = \ell \bmod r$, and any other modes whose amplitude is larger then desired accuracy $1/\delta$, see (4.76), to yield an approximation of first blade forced response (4.94).

8. Response for all other blades follows from symmetry (4.69).

9. Redo above for all relevant spatial modes ℓ of item 3. Summation over all such modes ℓ yields final result.

Notice that all of the above only requires information at the tuned point $z = 0$.

4.4 Mistuning Sensitivity

In the following two sections we describe some factors that create the sensitivity to mistuning. Section 4.4.1 deals with stability sensitivity, while Section 4.4.2 discusses forced response sensitivity.

4.4.1 Stability Sensitivity

The results of Section 4.2.2 present an interesting dilemma. We know experimentally [Whi64] that stability boundaries can be sensitive to (zero-average) mistuning: $s(z)$ varies sharply with z. (We can always consider zero-average mistuning because the averaged part $\sum z_i/r$ corresponds to a tuned change.) Yet equation (4.17) proves that (zero-average) mistuning appears as a second-order effect: $s(z) = O(\|z\|^2)$ when $\sum z_i = 0$. It follows that second order terms $z^T S z$ should be creating the mistuning sensitivity. Hence $\|S\|$ (leading order mistuned sensitivity) must be large compared to $|a|$ (the tuned sensitivity) in (4.17).

Thus, if we pick a random mistuning direction $\|\hat{z}\| = 1$ and vary the size of mistuning along this direction $z = \alpha\hat{z}$, we get the quadratic curve

$$s(\alpha\hat{z}) = \left[a\sum_{i=1}^{r}\hat{z}_i\right]\alpha + \left[\hat{z}^T S\hat{z}\right]\alpha^2 + O(\|\alpha\|^3) \tag{4.95}$$

with $a\sum_{i=1}^{r}\hat{z}_i$ small or zero compared to $\hat{z}^T S\hat{z}$ (see Figure 4.8). Hence the symmetry ar-

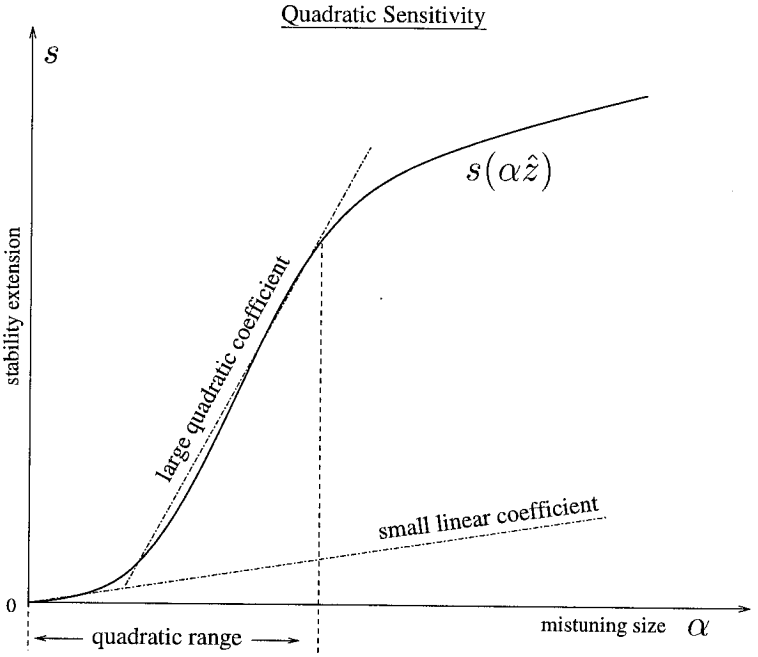

Figure 4.8: Stability sensitivity to mistuning

guments of Section 4.2.2 provide a simple explanation of stability results seen by other researchers. For example, both Bendiksen [Ben86, Figures 2 & 3] and Crawley, Hall [CH85, Figures 12 & 13] display the characteristic quadratic shape of Figure 4.8. The analysis of Section 4.2.2 reveals two factors which can cause $\|S\|$ to be large compared to $|a|$.

i) Nearby Eigenvalues

Quadratic coefficients b, c_i, which depend on second order eigenvalue motion $\partial^2\lambda/\partial z_i^2$, are inversely related to the distance between eigenvalues $|\lambda_i - \lambda_j|$ (equations (4.39), (4.40) and (4.42)). However, the linear coefficient $|a|$ is independent of $|\lambda_i - \lambda_j|$ (equation (4.38)). Consequently, nearby eigenvalues create a large $\|S\|/|a|$ ratio. Nearby eigenvalues also limit

the range where our small mistuning perturbation method is valid (see Section 4.3.1). For stability analysis, the eigenvalue/vector approximation method is aimed at the case where eigenvalues are close enough to create mistuning sensitivity ($\|S\|/|a|$ large) but are sufficiently far apart so that leading order (quadratic) terms in (4.17) provide valuable information.

The distance between eigenvalues is roughly determined by size of the blade coupling (aerodynamic or structural) divided by the number of blades (see Section 4.5). If the blade geometries are complex, there exist more structural modes per blade and so the distance between eigenvalues shrinks further. Hence compressors with stubby (rigid) blades and large (flexible) disks will have large structural coupling and the eigenvalues will be far apart. Typically, this is the case for compressors near the back of the engine where the blade passages become small. Here, our stability approximation will be accurate but the stability sensitivity will be low. On the other hand, lightly loaded fans with long blades and rigid disks will have small structural and aerodynamic coupling. Now the eigenvalues will be close together, stability sensitivity will be high and our approximation will only hold in a small region of z space.

For example, Figure 4.10 shows data from a simple Pratt and Whitney model for a compressor with no structural coupling and only small aerodynamic coupling. Here the tuned eigenvalues (denoted by *) are very close together. Now we introduce mode one mistuning $z_j = \epsilon\hat{z}_j = \epsilon\cos(2\pi j/r)$ where the size of mistuning ϵ varies between 0 and 1.485% in .033% increments. Eigenvalues approximations are given by $\lambda(z) \approx \lambda(0) + z^T\Phi z = \lambda(0) + (\hat{z}^T\Phi\hat{z})\epsilon^2$ and correspond to straight lines in Figure 4.10. True eigenvalue motion was computed by solving the mistuned $M(\epsilon\hat{z})$ eigenvalue problem directly, and this corresponds to the curved lines in Figure 4.10. The exact (grey curved) and approximate (black straight) eigenvalues paths always agree for sufficiently small ϵ where leading order quadratic terms are sufficient. However, Figure 4.10 clearly demonstrates that for small coupling, the approximation (4.78) can hold in a very small region of z space. In some cases the region of agreement is so small it cannot be distinguished in Figure 4.10. (By comparison, for the high-fidelity model of Chapter 6 the approximation holds up to about 10% mistuning for the least-stable non-colliding eigenvalues, see Figure 6.9.)

The size of coupling in this example is not realistic. For compressors with stubby blades,

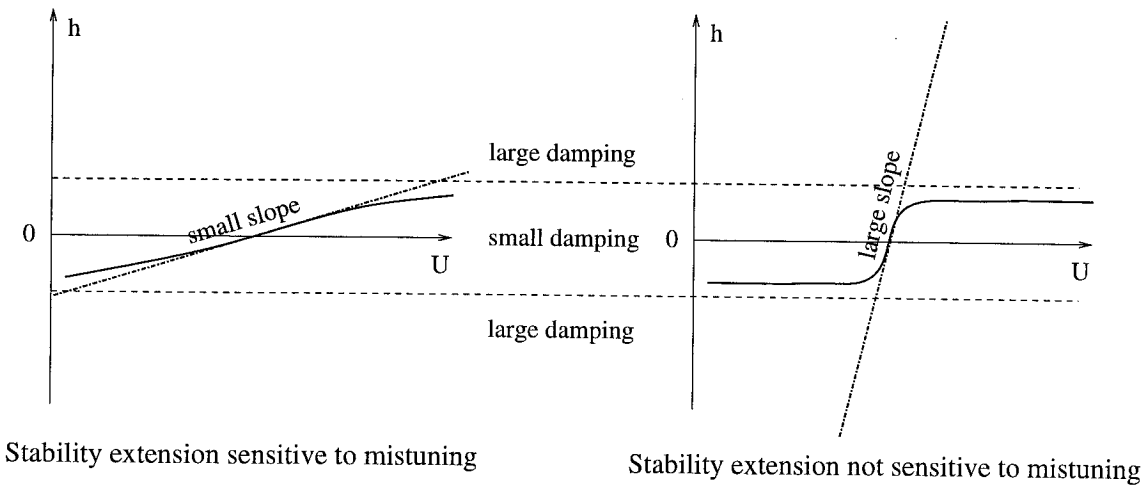

Figure 4.9: Stability sensitivity to mistuning can depend on damping slope $\partial h/\partial U$.

the aerodynamic coupling is indeed small; however the structural coupling can be quite large. The model used for Figure 4.10 includes the small aerodynamic coupling but ignores the larger structural coupling, hence the tuned eigenvalues are too close and this creates sharp eigenvalue veering.

In between the small/large blade coupling extremes (where many practical problems reside and the quadratic dependence of $s(z)$ is seen clearly [Ben86, CH85]) sensitivity will increase and the region of method validity will decrease as blade coupling decreases. This is natural; it is harder to describe more sensitive problems. In contrast, forced response sensitivity is caused primarily by light-damping. In that case we can have distant eigenvalues (so we achieve good eigenvalue tracking in our forced response analysis) together with high forced response sensitivity.

ii) Slow change in damping

The term $\partial h/\partial U = \mathrm{Re}[\partial\lambda_p/\partial U]$ in equations (4.38), (4.39) and (4.40) is the rate of change in damping $\mathrm{Re}[\lambda_p]$ with loading. This terms appears once in the denominator of (4.38) and three times in the denominators of (4.39) and (4.40). Hence a small $\mathrm{Re}[\partial\lambda_p/\partial U]$ will typically create a large $\|S\|/|a|$. (Of course other terms such as $\partial^2\lambda_p/\partial U^2$ also influence the size of $\|S\|/|a|$.) The small damping found in jet-engines typically creates a small $\mathrm{Re}[\partial\lambda_p/\partial U]$ term

(left of Figure 4.9) but this need not be the case (right of Figure 4.9).

4.4.2 Forced Response Sensitivity

There exists a simple and elegant geometric interpretation of the forced response solution. Consider a hypothetical three-blade, two-states-per-blade example as in Figure 4.11. First look at the tuned case. The tuned matrix $M(0)$ of (4.3) has six eigenvalues $\lambda_j^d(0)$. These eigenvalues are labeled by index j and plotted as crosses in the complex plane at the top-left of Figure 4.11. Here the jth tuned eigenvalues correspond to the jth nodal diameter mode. Hence each tuned eigenvalue $\lambda_j^d(0)$ has associated tuned right eigenvectors (or jth nodal diameter mode shape) $V_j^d(0)$ with constant inter-blade-phase-angle $2\pi j/r$, $j = 0, 1$ or 2. Theorem 3.4.1 implies λ_j^d has complex conjugate λ_{r-j}^d (the backwards traveling wave) so the numbering of modes in Figure 4.11 is correct.

Our forcing is taken to be purely second modal ($\ell = 2$ in (4.3), think of two upstream struts) and so only modes with $j = 2$ are active (as denoted by circled eigenvalues in top-left of Figure 4.11). In fact, this is a consequence of (4.74) and (4.75) which state that the tuned forcing vector $B_\ell(0)$ lies in the subspace $V_L^\bullet(0)$ generated by $V_L^1(0), V_L^2(0), \cdots, V_L^m(0)$. Physically, the $j = 2$ tuned nodal diameter mode shape matches the $\ell = 2$ spatial forcing. This is denoted schematically in middle-left of Figure 4.11 where $B_2(0)$ exactly lines up with subspace $V_2^\bullet(0)$. Hence forcing $B_2(0)$ can only affect $j = 2$ modes and so we write in shorthand

$$X(0) = \gamma_2 V_2^\bullet(0)$$

meaning that the response only contains $j = 2$ modes. Coefficients in γ_2 are proportional to the inverse of distance $|\lambda_j^d(0) - i\omega|$, thus lightly damped modes forced near resonance create large γs. In our example, $\lambda_2^1(0)$ has medium damping (mode $j = 2, d = 1$ in top-left of the complex plane) while lightly damped mode $\lambda_2^2(0)$ (mode $j = 2, d = 2$ at bottom-left) is far from resonance for all positive rotation speeds of the fan. Hence $j = 2$ modes generate the gentle Bode plot at bottom-left of Figure 4.11, with associated resonant frequency $w_2 = \mathrm{Im}[\lambda_2^1(0)]$.

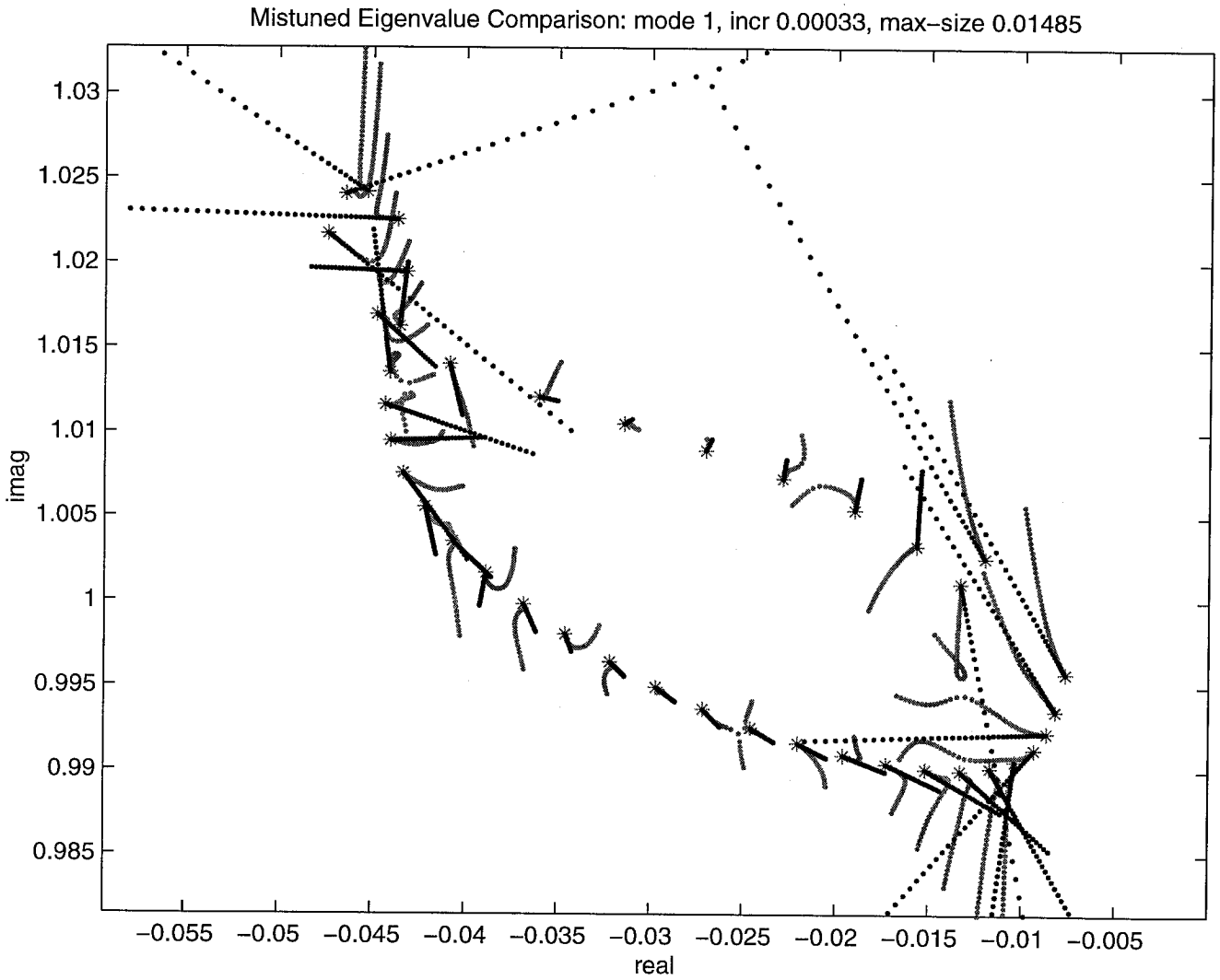

Figure 4.10: Eigenvalue veering with mistuning for P&W model: tuned eigenvalues (*), exact mistuned eigenvalues (·, grey curved paths), approximate mistuned eigenvalues (·, black straight paths).

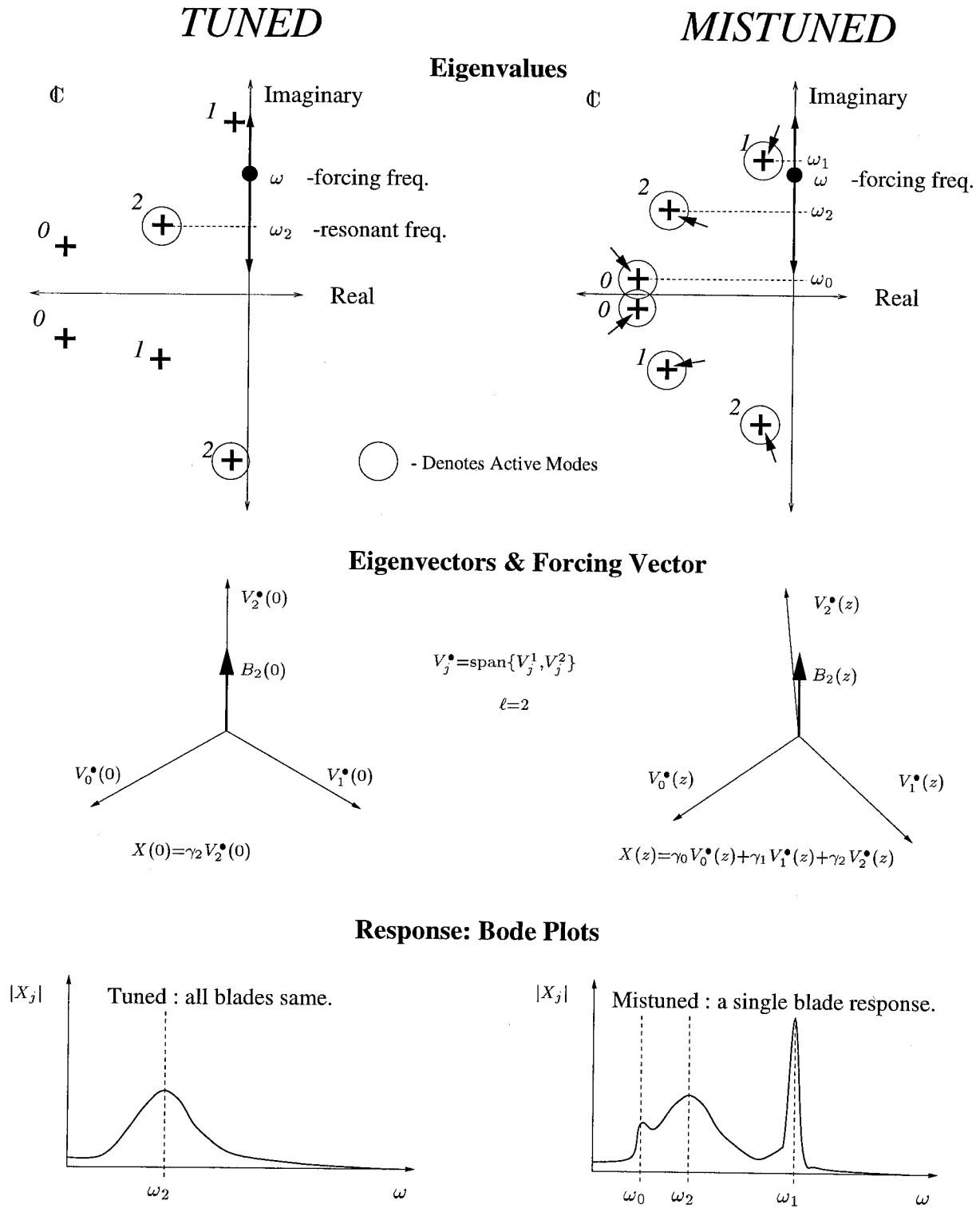

Figure 4.11: Geometric explanation of mistuning sensitivity.

Now suppose we allow mistuning. First of all, the eigenvalues shift as shown in top-right of Figure 4.11 and this movement is captured by expansion (4.78). Such motion may be either stabilizing or destabilizing, in our example we show the stabilizing case (least stable eigenvalues move left) as is often the case. Yet the eigenvalues are not perturbed alone, the eigenvectors also shift away from the tuned case as in equations (4.83), (4.84) and as shown pictorially in middle-right of Figure 4.11. By breaking the symmetry, the modes (eigenvectors) are no longer pure nodal diameter modes where each blade response is separated by a constant inter-blade-phase-angle. Now (the forcing) $B_2(z)$ no longer lines up with subspace (mode shapes) $V_2^\bullet(z)$ and so $B_2(z)$ can project onto *all* the eigenvectors. Notice that $B_2(z)$ typically retains its direction since $\ell = 2$ basically corresponds to second modal forcing (as could be caused by two upstream struts) and will not be affected by mistuning of blades. All modes are now excited and this is denoted by all modes being circled in the top-right of Figure 4.11. The associated forced response has the form

$$X(z) = \gamma_0 V_0^\bullet(z) + \gamma_1 V_1^\bullet(z) + \gamma_2 V_2^\bullet(z),$$

where the size of coefficients in γ_j is determined by the amount $B_2(z)$ projects onto eigenvector subspace $V_j^\bullet(z)$ times the inverse of $|\lambda_j^d(z) - i\omega|$ which measures the distance from resonance. Since mode one, $\lambda_1^1(z)$, has very light damping, γ_1 will be large at resonance even for very small shifts in the eigenvectors. As a result we get the Bode plot shown in bottom-right of Figure 4.11 with the severe peak at $\omega_1 = \mathrm{Im}[\lambda_1^1(z)]$. In a nutshell, this is the mode localization phenomena. Even when mistuning is stabilizing (modes shift to the left) the appearance and resonance of previously unexcited low-damped modes can cause huge peaks. Moreover, the problem is incredibly sensitive. Tiny changes in the eigenvectors, as created by small random mistuning due to machining imperfections, may create unacceptably large vibrations due to low damping found in turbomachines. Of course this extends to the case of multiple mode forcing (many values of ℓ in (4.3)). For example: we might have forcing with weak $\ell = 1$ (say a mode one inlet distortion) and strong $\ell = 2$ (our two struts) spatial decomposition, creating an acceptable tuned response in modes $j = 1$ and $j = 2$. Upon mistuning, the large $\ell = 2$ forcing component will excite an unacceptable response in the lightly damped $j = 1$ mode.

4.5 Behaviour Implied by Model Structure

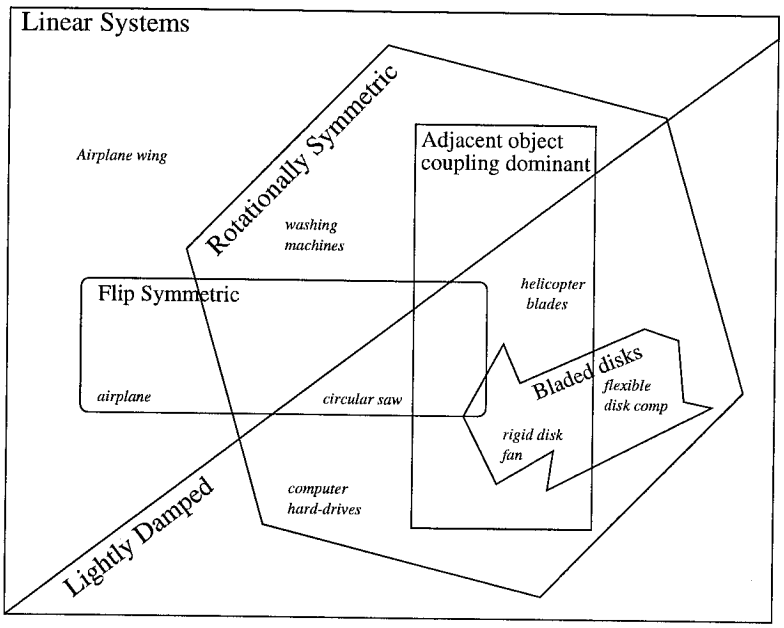

Figure 4.12: Some possible model sets with examples.

The tools developed so far are aimed at systems with circulant symmetry. This is a large class of systems that includes bladed-disks, circular saws, car brake hubs, washing-machine spindles and helicopter blade assemblies—in fact any device that has r circumferentially arranged features which can be mistuned. Hence the restricted set of behaviour derived must hold true for washing-machines, just as it does for bladed-disks. In a sense, the allowable set of behaviour is still too rich. We would like to be able to differentiate between bladed-disks and washing-machines without having to write down a specific bladed-disk or washing-machine model. To do this we can start making general observations: bladed-disks are lightly-damped, whereas washing-machines, one would guess, are not. By assuming light-damping we can show additional behaviour. This is the idea behind Figure 4.12 where we show different sets corresponding to general modeling assumptions. By making these further assumptions, we restrict the set under consideration and approach the devices of interest. Doing this top-down approach has advantages over a bottom-up (or search) approach where we would try to improve (or enlarge) the set of models under consideration. Specifically, it does not require accurate models, we can make interesting statements based solely on generic

statements such as: damping is small, coupling is dominated by adjacent-blades, or damping of the disk is higher then damping of the blades. This is what we mean by "behaviour" from "model structure." We have already done some of this informally; we considered flip symmetric and simple mechanical systems in Section 3.6.1, and lightly damped systems in Section 4.4.2. Below we study the case where coupling is dominated by adjacent blades which can be true for aerodynamic coupling.

4.5.1 Tuned Eigenvalue and Eigenvector Structure

For the block-circulant tuned linearization $\bar{M} = M(0)$ as in equation (3.15), the tuned eigenvalues are the eigenvalues of the Q_j matrices in Theorem 3.4.1,

$$Q_j = \bar{M}_1 + p_j\bar{M}_2 + p_j^2\bar{M}_3 + \cdots + p_j^{r-1}\bar{M}_r. \tag{4.96}$$

Let η_d with $d = 1, 2, \ldots, m$ be the eigenvalues of $\bar{M}_1$. These are the blade-alone eigenvalues because $\bar{M}_1$ describes how each blade affects itself. Thus η_d essentially captures the structural modes for a single blade perturbed slightly by blade-alone aerodynamic effects (no structural or aerodynamic blade-to-blade coupling yet).

If there is one state per blade ($m = 1$), the $\bar{M}_j$'s are scalars and the tuned eigenvalues are simply $\lambda_j = \bar{M}_1 + p_j\bar{M}_2 + p_j^2\bar{M}_3 + \cdots + p_j^{r-1}\bar{M}_r$. We see that each $\bar{M}_j$ creates a circular eigenvalue loop. So, for example, if all the $\bar{M}_j$'s are zero except for $\bar{M}_1 = \eta$ and $\bar{M}_5 = \epsilon$ (blade one only couples to blade five), then $\lambda_j = \eta + p_j^4\epsilon$ where $p_j = \exp[2\pi ij/r]$ and $j = 1, 2, \ldots, r$. Hence the coupled eigenvalues are arranged in a circle of radius ϵ about the blade-alone eigenvalue η.

When $m > 1$ the $\bar{M}$'s are m sized matrices. For this case suppose the blade coupling (aerodynamic or structural) is small: $\|\bar{M}_1\| \gg \|\bar{M}_j\|$ for all $j > 1$. Then we can view each Q_j as a perturbation away from $\bar{M}_1$, thus by standard eigenvalue perturbation techniques (as in equation (4.41))

$$\lambda_j^d = \eta_d + p_j[\alpha_d\bar{M}_2\beta_d] + p_j^2[\alpha_d\bar{M}_3\beta_d] + \cdots + p_j^{r-1}[\alpha_d\bar{M}_r\beta_d] + O(\|\bar{M}_j\|^2) \tag{4.97}$$

where α_d, β_d are the left, right eigenvectors of $\bar{M}_1$ (normalized as $\|\beta_d\| = 1$ and $\alpha\beta = I$). So long as the $\bar{M}_j$'s are small compared to $\bar{M}_1$ the same statement holds as above: each $\bar{M}_j$ creates an eigenvalue loop of size $|\alpha_d \bar{M}_j \beta_d|$ about the blade-alone eigenvalue η_d. This is shown graphically in Figure 4.13 for three blades. So the tuned eigenvalue spread, or the

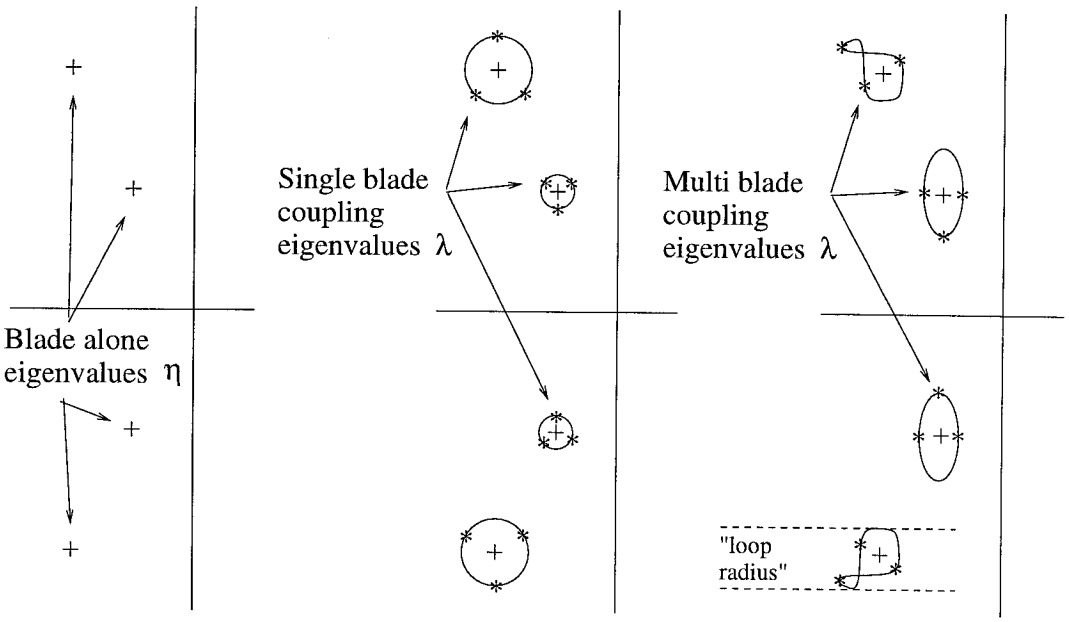

Figure 4.13: Tuned eigenvalue loops caused by blade coupling.

"loop radius," roughly measures the amount of blade coupling. If there is only adjacent blade coupling, then $\bar{M}_2$ and $\bar{M}_r$ in equation (4.97) create an ellipse centered at η: $\lambda_j^d = \eta_d + p_j\epsilon_1 + p_{-j}\epsilon_2$. When the coupling is dominated by adjacent blade terms, the eigenvalues lie close to this ellipse (this can be clearly seen in Figure 4.15).

Similar to equation (4.97), we can find a perturbation equation for the tuned left and right eigenvectors of Q_j,

$$u_j^d = \alpha_d + \sum_t^{\eta_t \neq \eta_d} \frac{\alpha_d[p_j\bar{M}_2 + \cdots + p_j^{r-1}\bar{M}_r]\beta_t}{\eta_d - \eta_t}\alpha_t + O(\|\bar{M}_j\|^2) \tag{4.98}$$

$$v_j^d = \beta_d + \sum_t^{\eta_t \neq \eta_d} \frac{\alpha_t[p_j\bar{M}_2 + \cdots + p_j^{r-1}\bar{M}_r]\beta_d}{\eta_d - \eta_t}\beta_t + O(\|\bar{M}_j\|^2). \tag{4.99}$$

The eigenvectors of the tuned matrix $\bar{M} = M(0)$ are now given by Theorem 3.4.1.

4.5.2 Adjacent Blade Coupling: Eigenvalue Motion

We can derive conditions on eigenvalue motion with mistuning based on the assumption of adjacent blade coupling. To ease computation, it is further assumed that the linearization matrix $M(z)$ can be written as

$$M(z) = \begin{bmatrix} \bar{M}_1 & \bar{M}_2 & \bar{M}_3 & \dots & \bar{M}_{r-1} & \bar{M}_r \\ \bar{M}_r & \bar{M}_1 & \bar{M}_2 & \bar{M}_3 & \dots & \bar{M}_{r-1} \\ & \ddots & & \ddots & & \\ & & \ddots & & \ddots & \\ \bar{M}_2 & \bar{M}_3 & \dots & \bar{M}_{r-1} & \bar{M}_r & \bar{M}_1 \end{bmatrix} + \begin{bmatrix} M'z_1 & 0 & 0 & \dots & 0 & 0 \\ 0 & M'z_2 & 0 & 0 & \dots & 0 \\ & \ddots & & \ddots & & \\ & & \ddots & & \ddots & \\ 0 & 0 & \dots & 0 & 0 & M'z_r \end{bmatrix}. \quad (4.100)$$

Hence it is assumed that mistuning appears along the diagonal, this is true for any individual blade property mistuning—such as blade mass, stiffness or natural frequency mistuning. It is also assumed that mistuning appears in a linear fashion which is approximately true for any small mistuning, and is always true for stiffness mistuning. Finally, assume that $|\eta_a - \eta_b| \gg \|\bar{M}_j\|$ for all $a \neq b$ and j. This means that the eigenvalue loops of Figure 4.13 are separated far apart and is consistant with the assumption that $\|\bar{M}_1\| \gg \|\bar{M}_j\|$.

Now restrict the discussion to adjacent blade coupling only, furthermore suppose the coupling due to the blade above and below is symmetric (as in the model of Chapter 2), then

$$\bar{M}_1 \neq 0, \quad \bar{M}_2 = -\bar{M}_r \neq 0. \quad (4.101)$$

All other coupling terms are zero

$$\bar{M}_3 = \bar{M}_4 = \cdots = \bar{M}_{r-1} = 0. \quad (4.102)$$

From equations (4.98) and (4.99), we find that $u_j^d \approx \alpha_d$ and $v_j^d \approx \beta_d$ since $|\eta_d - \eta_t|$ is large compared to $\|\bar{M}_j\|$. (Keep in mind that we are approximating the blocks u, v of the tuned eigenvectors U, V, see Theorem 3.4.1.) Using the above together with equations (4.80), (4.42), (4.44) and (4.97) yields coefficient $\psi_l^{j,d}$ of eigenvalue expansion (4.78) for eigenvalue

$\lambda_j^d(z)$,

$$\psi_l^{j,d} \approx R \sum_t \frac{\cos(\frac{2\pi l(j-t)}{r})}{\sin(\frac{2\pi t}{r}) - \sin(\frac{2\pi j}{r})} \tag{4.103}$$

where

$$R = \frac{i(\alpha_d M' \beta_d)^2}{r^2 \alpha_d \bar{M}_2 \beta_d} \in \mathbb{C} \tag{4.104}$$

and the summation is taken over all indexes t where the denominator is nonzero. So the arrangement of eigenvalue coefficients $\psi_l^{j,d}$ of expansion (4.78) can essentially be derived from the statement that adjacent blade coupling is dominant (the complex coefficient R merely fixes the orientation and depends on how the left, right eigenvectors of $\bar{M}_1$ pass through the mistuning perturbation M' and coupling $\bar{M}_2 = -\bar{M}_r$ terms).

For example, if we have 11 blades we know by equation (4.97) that the 3rd or 8th nodal diameter eigenvalue is least stable. (According to equation (4.97), for adjacent blade coupling as in (4.101) and (4.102) we have the eigenvalue perturbation term $(p_j - p_j^{r-1})(\alpha_d \bar{M}_2 \beta_d) = 2i(\alpha_d \bar{M}_2 \beta_d)\sin(2\pi j/r)$. This makes eigenvalue line-up in a straight line oriented with complex phase $i\alpha_d \bar{M}_2 \beta_d$. The 3rd and 8th eigenvalues are at the tips of this line.) For the model of Chapter 2, $i\alpha_d \bar{M}_2 \beta_d$ is in the right-half plane and so the $j = 3$ eigenvalue is least stable. Substituting $j = 3$ into equation (4.103) we find that the summation term increases monotonically in l (the summation term is real). Hence depending on the phase of R, the real part of the stability coefficients $\psi_l^{j,d}$ increases (or decreases) monotonically in l for the least stable eigenvalue. For the model of Chapter 2, R is in the right-half plane and so the real part of the stability coefficients increases monotonically. This means we can apply the results of Section 5.1.2 to conclude that the optimal stabilizing arrangement of blades is the "pyramid arrangement" as shown in Figure 5.2 (here we are minimizing the real part of the least stable eigenvalue so conditions (5.5), (5.6), now written for ψ_l instead of c_l, are flipped). This information is based only on the statement that coupling is dominated by adjacent blades and that R is in the right-half plane (the last part holds true for a wide range of parameters in the model of Chapter 2; if R is in the left-half plane then the "pyramid

arrangement" becomes the most destabilizing mistuning).

4.6 Example: Quasi-Steady Model

Our perturbation method is applied to a quasi-steady, inviscid, incompressible, linear model (as developed by Coller in [SC97]) with eleven blades ($r = 11$) and three states per blade ($m = 3$)). Here the structural dynamics are modeled by a linear mass-spring system

$$m_j \ddot{q}_j + k_j q_j = 2bL_j \tag{4.105}$$

where q_j is the bending displacement of blade j; b is the semi-chord length; and the mass and spring stiffness m_j, k_j can be mistuned. The aerodynamic forces L_j are computed by solving a steady, inviscid, irrotational flow through a cascade of flat-plate airfoils for arbitrary blade displacement and velocity. This involves solving a linear Fredholm equation of the first kind. Reducing the equations by intelligently choosing a finite number of spatially distributed vorticity modes, one can write and solve a reduced set of linear algebraic equations. This yields a steady lift for arbitrary blade displacement and velocity: $L = L(q, \dot{q})$. Aerodynamic unsteadiness is modeled by a simple lag equation (hence the 'quasi-steady' designation). Non-dimensionalizing in standard fashion, we get the non-dimensional quantities of time $t \mapsto Vt/(2b)$, deflection $q \mapsto q/(2b)$ and reduced velocity $U \mapsto V/(2bw_0)$ where $w_0 = \sqrt{k_0/m_0}$ is the tuned natural frequency and V is dimensional velocity. This yields the model equations

$$M(U,z) = \begin{bmatrix} A_1^1 & A_2^1 & A_3^1 & \dots & A_{r-1}^1 & A_r^1 \\ A_r^2 & A_1^2 & A_2^2 & A_3^2 & \dots & A_{r-1}^2 \\ & \ddots & & \ddots & & \\ & & \ddots & & \ddots & \\ A_2^r & A_3^r & \dots & A_{r-1}^r & A_r^r & A_1^r \end{bmatrix}. \tag{4.106}$$

In the above,

$$A_1^i(U,z_i) = \begin{bmatrix} 0 & 1 & 0 \\ \left(-\frac{1+\delta k_i}{U^2(1+\delta m_i)} + \frac{2\rho b^2 \sin(\alpha) f_1}{m_0(1+\delta m_i)}\right) & \frac{2\rho b^2 c e_1}{m_0(1+\delta m_i)} & \frac{2\rho b^2(1-c)e_1}{m_0(1+\delta m_i)} \\ 0 & \frac{2Uw_0}{\tau} & -\frac{2Uw_0}{\tau} \end{bmatrix} \tag{4.107}$$

and for $j \neq 1$

$$A_j^i(U,z_i) = \begin{bmatrix} 0 & 0 & 0 \\ \frac{2\rho b^2 \sin(\alpha) f_j}{m_0(1+\delta m_i)} & \frac{2\rho b^2 c e_j}{m_0(1+\delta m_i)} & \frac{2\rho b^2(1-c)e_j}{m_0(1+\delta m_i)} \\ 0 & 0 & 0 \end{bmatrix} \tag{4.108}$$

where mistuning can appear as $\delta k = z$ (stiffness mistuning where $k_i = k_0(1+z_i)$) or $\delta m = z$ (mass mistuning where $m_i = m_0(1+z_i)$).

4.6.1 Example Stability Analysis

We take the reduced velocity

$$U = \frac{V}{2b}\sqrt{\frac{m_0}{k_0}}$$

as the loading parameter. Within this model we can mistune two quantities, the blade stiffness k_j and mass m_j. It was noticed that both forms of mistuning result in almost identical behaviour, both in coefficients computed $a, b, c_1, \ldots, c_k$ and in optimization results. Consequently, we only discuss stiffness mistuning.

In Section 4.2.3 we outlined seven steps to compute the coefficients $a, b, c_1, \ldots, c_k$. Computing eigenvalues and vectors by Theorem 3.4.1 we can plot $h(U,0)$ of Step 3, Section 4.2.3 (Figure 4.14). Here $U_{crit}(0) = 6.818$ and evaluating steps five through seven (end of Section 4.2.3) yields the coefficients $a, b, c_1, \ldots, c_k$. Comparison with Method B of Section 4.2.2 shows that for ϵ sufficiently small in equations (4.45),(4.46) and (4.47), the coefficients computed by Methods A and B fall arbitrarily close to one another (up to machine error) hence results for Method B are not shown.

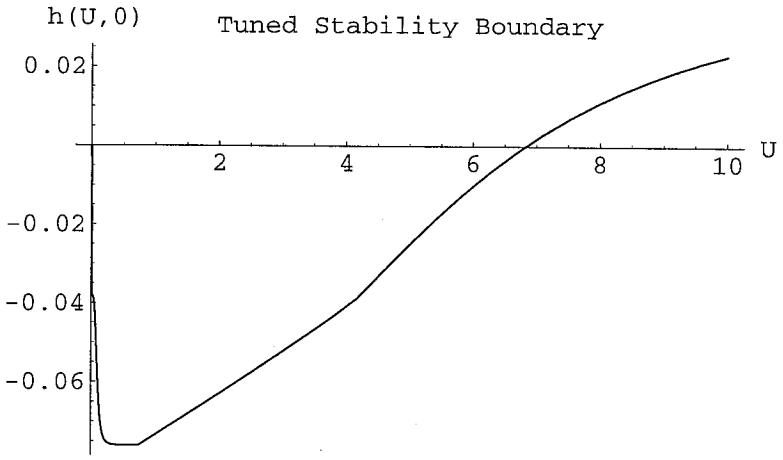

Figure 4.14: Minimum damping versus loading.

a	b	c_1	c_2	c_3	c_4	c_5
0.310	0.529	0.554	0.154	-0.205	-0.483	-0.632

Table 4.2: Analysis coefficients for stiffness mistuning.

One can see that coefficients $b, c_1, \cdots, c_5$ are not large compared to a. Hence the stability of this model is not very sensitive to mistuning (this will be verified explicitly in Section 5.1.1). This is because the distance between the tuned eigenvalues is fairly large compared to the structural natural frequency (loop radius/natural frequency ≈ 0.25 in Figure 4.15).

The coefficients a, b, c_i can provide a surprising amount of information. For example, if we consider the even simpler model discussed in Chapter 2, then we can include angle-of-attack mistuning. In that case we get a different set of a, b, c_i coefficients. Now for a range of model parameters it can be shown in closed form that S (of equation (4.17)) is negative definite. As a result, for zero-average mistuning we have $s(z) \approx z'Sz < 0$ for all $z \neq 0$ (see equation (4.17)). Hence this simpler model predicts that zero-average, angle-of-attack mistuning can only decrease stability. This is commensurate with compressor design experience. The angle-of-attack in bladed disks is carefully controlled to provide uniform flow and prevent aerodynamic losses, it is plausible that all non-uniform changes in angle-of-attack will lead to a decrease in performance.

4.6.2 Example Forced Response Analysis

To study forced response we choose a loading that creates a lightly-damped system $U \approx U_{crit}(0) = 6.818$. The resulting tuned lightly-damped eigenvalues $\lambda_j^d(0)$ are shown in Figure 4.15 labeled by index j. Eigenvalues λ_2^3 and λ_9^3 are the most lightly damped with damping ratio $-\text{Re}[\lambda]/|\lambda| = 0.0000330/0.0376 = 0.000875$, a small damping on the verge of instability.

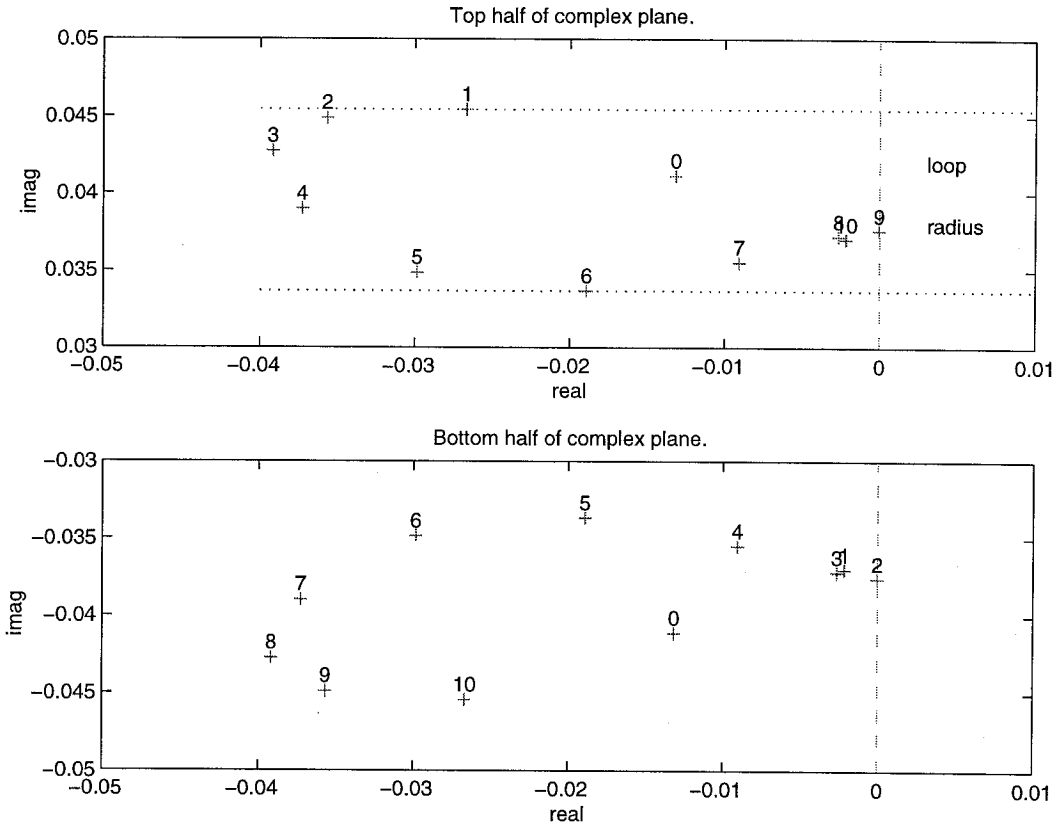

Figure 4.15: Tuned eigenvalues $\lambda_j^d(0)$ labeled by nodal diameter j.

From the tuned eigenvalues of Figure 4.15 we can predict the nature of the tuned and mistuned response. We pick spatial forcing mode $\ell = 1$. Since the tuned system only displays forced modes, only modes $\lambda_1^d(0)$ are active. From Figure 4.15 we see that for positive forcing frequencies all of the $j = 1$ modes (λ_1^1, λ_1^2 and λ_1^3) are far from resonance. (Mode $\lambda_1^1(0)$ has very high damping and is to the left of Figure 4.15 [not shown]. Mode

$\lambda_1^2(0)$ has positive frequency and medium damping. Finally, mode $\lambda_1^3(0)$ has small damping but negative frequency, thus it is not excited by the positive forcing frequency.) As a result, if we plot the amplitude of vibration as a function of forcing frequency ω we get the gentle Bode plot of Figure 4.16 with resonant peak $\mathrm{Im}[\lambda_1^2(0)] = 0.0454$ (see equations (4.64) and (4.65)).

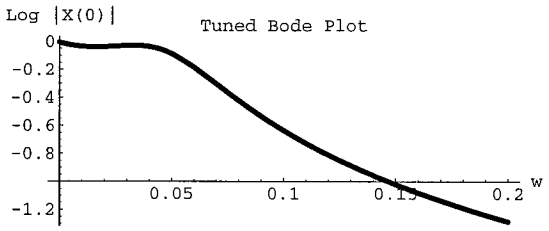

Figure 4.16: Tuned Bode plot: $z = 0$.

Such gentle behaviour is lost upon introduction of mistuning. To illustrate the point we pick a small random mistuning z_{rnd} where we have changed the stiffness of each blade by less then two percent. The system is still stable. Plotting the amplitude of response for each blade as a function of forcing frequency ω yields the Bode plot of Figure 4.17. The thick-line denotes the tuned response, while the eleven thin-lines denote the mistuned response of each blade. As demonstrated in Figure 4.11, all modes now come into play and the response is

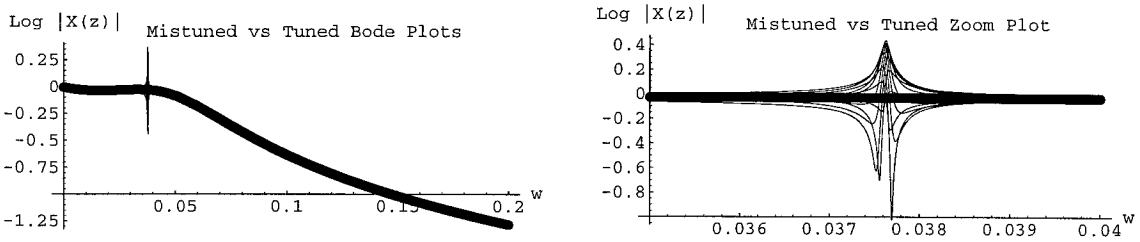

Figure 4.17: Mistuned Bode plot with zoom: $z = z_{rnd}$.

dominated by the least stable mode $\lambda_9^3(z_{rnd})$ which resonates at $\omega = 0.0376$. We can see that the mistuned response is very sharp and its peak is half an order of magnitude above the tuned response, a direct consequence of the lightly-damped mistuned $j = 9$ eigenvalue: $-\mathrm{Re}[\lambda_9^3(z_{rnd})]/|\lambda_9^3(z_{rnd})| = -0.000050/0.0376 = 0.001330$. This demonstrates numerically the sharp sensitivity to mistuning discussed in Section 4.3.1. Clearly, the performance is disastrous at λ_9^3 resonance: $\omega = 0.0376$.

Let us compare the tuned and mistuned response at two frequencies: the resonant frequency $\omega = 0.0376$ and a frequency $\omega = 0.02$ which is far from resonance. Figure 4.18 shows the response for the tuned and mistuned system at these frequencies. In both cases, solid-dots denote the amplitude and phase of each blade for the tuned response (all blades have equal amplitude and are separated by a constant-inter-blade-phase-angle) while solid-squares denote the mistuned response. For the resonant frequency we see that even a small amount of mistuning $z = z_{rnd}$ can cause a large degree of scatter due to the excitation of previously dormant $j = 9$ modes. In contrast, for $\omega = 0.02$ far from resonance, other modes are basically not excited and the mistuned response is nearly identical to the tuned response.

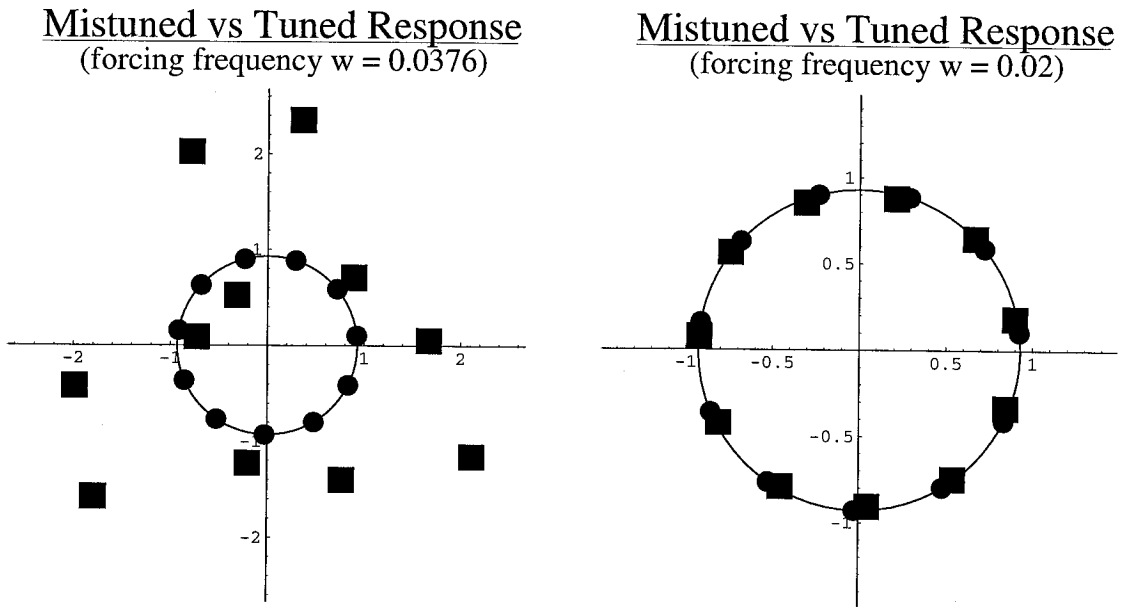

Figure 4.18: Tuned ($z = 0$) vs mistuned ($z = z_{rnd}$) response.

All of the data above is given by approximation (4.94). Figure 4.19 compares the approximation (4.94) with the exact solution of equation (4.5) for $z = z_{rnd}$ and $z = 5\,z_{rnd}$ at $\omega = 0.0376$. As in Figure 4.18, we are plotting the amplitude and phase of each blade. Here the circle at the origin denotes the size of the tuned response; open-circles denote the exact mistuned response found by solving (4.5) at $z = z_{rnd}$ or $z = 5\,z_{rnd}$ with $\omega = 0.0376$; crosses represent the series approximation of [Sin86]; solid-squares are given by the full-mode approximation (4.94) and; solid-triangles represent a partial-mode approximation with $\delta = 0.005$

in (4.76).

Our method gives excellent results for small mistuning $z = z_{rnd}$ and provides acceptable results for larger (roughly 9%) mistuning $z = 5\,z_{rnd}$. In contrast, the series method results used in the literature fail to converge (in the small mistuning case $z = z_{rnd}$ they are completely inaccurate, while in the larger case $z = 5\,z_{rnd}$ they are off the scale of the plot). This is because the series convergence criteria $\rho(A_0^{-1}\Delta A_z) < 1$ of Section 4.3.1 fails in both cases. Consequently, inclusion of additional terms in the series expansion will be of no use.

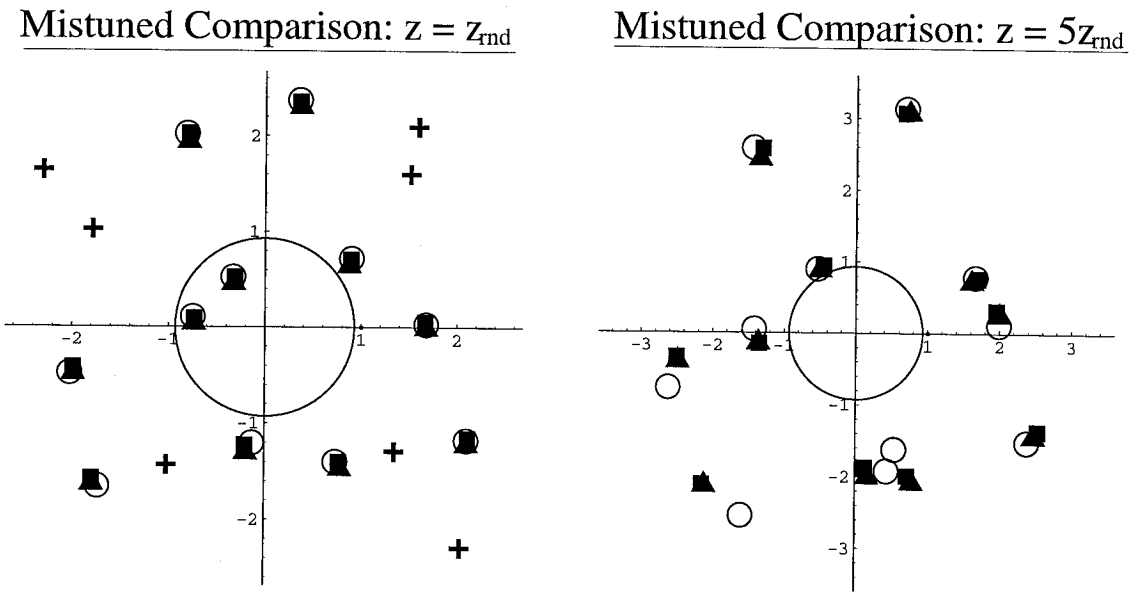

Figure 4.19: Approximation comparison at resonance frequency $\omega = 0.0376$ for small and large mistuning: Exact response of equation (4.5) = open-circle; Approximate response of equation (4.94) = filled-square; Partial-mode approximate response of equation (4.76) = filled-triangle; Series method of [Sin86] = cross.

4.7 Literature Misconceptions

At this point we can dispel two misconceptions found in the literature. One, sensitivity to mistuning is caused primarily by light-damping and the destruction of eigenvector symmetry (see Figure 4.11), not mode-veering or weak/strong blade coupling (except insofar as these cause or combine with light-damping). Look at equations (4.64) and (4.65). These equations are exact. Weak blade coupling causes eigenvalues to cluster and creates fast eigen-

value/vector motion (veering of $\lambda(z), V(z)$ and $U(z)$). However, this veering occurs in the vicinity of the clustered eigenvalues/vectors—it is confined to a small region. If the clustered eigenvalues are far into the left-half-plane (strong-damping) the net effect on response (4.64) and (4.65) is small. Mode veering without light-damping *cannot* cause mistuning sensitivity. Light-damping without mode-veering *can* cause mistuning sensitivity (see Table 4.1).

Two, there are no bifurcations in the linear forced response problem (4.5). Some past researchers [AN89] have confused the quickly varying behaviour of $X(z)$ caused by the fast, but smooth, dependence on mistuning in (4.77) with a strict definition of bifurcations. To be precise, $\hat{z}$ is a bifurcation point for dynamics (4.5) if X is not smooth at $\hat{z}$. Yes, eigenvalue/vector motion can be discontinuous. However, $\partial X(\hat{z})/\partial z$ is always well defined unless an eigenvalue of $M(\hat{z})$ lands on the imaginary axis (this follows from Theorem 4.7.1).

Theorem 4.7.1 *Consider a matrix $A(\alpha)$ dependent on real scalar α with $A(\alpha)$ smooth and invertible for all α in (α_1, α_2). So $dA(\alpha)/d\alpha$ and $A^{-1}(\alpha)$ exist for all $\alpha \in (\alpha_1, \alpha_2)$. Then $dA^{-1}(\alpha)/d\alpha$ exists for all $\alpha \in (\alpha_1, \alpha_2)$ meaning $A^{-1}(\alpha)$ is smooth for all values α in the open interval (α_1, α_2).*

Proof: The proof is standard and proceeds by construction. For any $\alpha \in (\alpha_1, \alpha_2)$ we have

$$\frac{d}{d\alpha}\left[A^{-1}(\alpha)A(\alpha)\right] = \frac{dI}{d\alpha} = 0.$$

By the product rule

$$\left[\frac{dA^{-1}}{d\alpha}(\alpha)\right]\left[A(\alpha)\right] + \left[A^{-1}(\alpha)\right]\left[\frac{dA}{d\alpha}(\alpha)\right] = 0$$

and so

$$\frac{dA^{-1}}{d\alpha}(\alpha) = -\left[A^{-1}(\alpha)\right]\left[\frac{dA}{d\alpha}(\alpha)\right]\left[A^{-1}(\alpha)\right]$$

which exists for all $\alpha \in (\alpha_1, \alpha_2)$ because $A^{-1}(\alpha)$ and $dA(\alpha)/d\alpha$ exist for all α in (α_1, α_2). ■

Theorem 4.2.1 extends to vector dependence, $\alpha \mapsto z$, by the chain rule. Hence $M(\hat{z})$

having no eigenvalues on the imaginary axis implies $A(\hat{z})$ is invertible and so $A^{-1}(z)$ is smooth at $\hat{z}$. Hence $X(z)$ is smooth at $\hat{z}$ by (4.59). No bifurcations occur unless $M(\hat{z})$ has eigenvalues on the imaginary axis. When this happens stability is lost: either the eigenvalue continues on into the right half plane, generic case, or stability is determined by the nonlinear terms we neglected in Section 4.1. Either way, (4.5) is meaningless when $M(\hat{z})$ has an eigenvalue on the imaginary axis. Thus it is meaningless to study the bifurcations of (4.5)—when a bifurcation exists (4.5) no longer applies.

4.8 Approximation Method Limitations

The eigenvalue/vector approximation method presented in this chapter is aimed at lightly damped systems because bladed-disks in turbomachines are known to have small damping. Hence the given perturbation is accurate for lightly damped systems; a case of practical importance. However, like any other perturbation technique, the method presented here will perform poorly in certain cases. Specifically, the leading order expansion of eigenvectors (to first order) and eigenvalues (to second order) captures the initial motion of eigenvalues and eigenvectors with mistuning. It does not capture subsequent eigenvalue/vector motion due to higher-order terms. Hence the method fails as eigenvalues approach one another and begin to veer sharply (see Figure 4.10 and Table 4.1). Such eigenvalue collision is more likely for close-by eigenvalues which are typically caused by small blade coupling (see Section 4.4.1). In practice, this turns out to be a significant, but not severe, restriction. For the high-fidelity model presented in Chapter 6, the blade coupling is quite small yet the perturbation of this chapter holds over a reasonable range (up to about 10% mistuning). Moreover, isolated eigenvalues are captured more accurately then grouped eigenvalues. This can be seen clearly in Figure 6.9 where most eigenvalues (including the most critical lightly-damped eigenvalues) are captured accurately up to about 10% mistuning. However, the eigenvalues that almost collide with one another veer away from their initial directions (for example at $(x, y) \approx (-0.2, 1)$ in Figure 6.9) and so for these eigenvalues the approximation fails.

A second method limitation has to do with computation size. In principle, the methods of this chapter hold for any linear system as shown in equation (4.3). In practice, it is not

possible to compute the quantities (4.19) of Section 4.2.2 for large CFD models. This means that we have to work with reduced low-order models (such as the model presented in Chapter 6) where these quantities are computable. Clearly, it is more difficult to generate such low-order models for complex fluid flows (e.g.,three-dimensional, turbulent, transonic flow) then for simpler flows (e.g., two-dimensional, inviscid, subsonic flow). Moreover, even though the framework in this thesis can deal with any type of mistuning; it is harder to generate models that include aerodynamic mistuning (such as blade-shape or angle-of-incidence) then it is to create models with structural mistuning (say mass or stiffness mistuning). Generating a model with aerodynamic mistuning requires an understanding of how each blade shape affects the flow field. So if we wanted to include blade shape mistuning in the model of Chapter 6, we would have to generate the flow field, and create the associated POD modes, for a set of mistuned cascades that would span all possible mistuned cascades. This requirement is over and above the 20 hours of runtime required to generate a low-order aerodynamic model without shape mistuning. In summary: the methods described in this thesis holds for any flow-condition and mistuning type; however, it is more difficult to generate the required low-order models for complex flow-conditions and aerodynamic mistuning than for simpler flow-conditions with structural mistuning.

Chapter 5 Passive Control of Flutter and Forced Response via Mistuning

Once the analysis question has been solved, the next concern is intentional mistuning. Here mistuning is viewed as a passive (no actuators) control scheme. Obvious questions are: when is mistuning beneficial? And, if it is beneficial what is the optimal mistuning? In order to address these questions we must define the notion of optimal mistuning.

First it is necessary to decide which "type" of mistuning will be used. Various possibilities include blade stiffness, blade angle of attack, blade shape and many other forms of mistuning. In this chapter it is assumed that the type of mistuning has been pre-determined and we will not concern ourselves with optimizing over type. We solve the stability optimization first, and then move on to tackle the combined stability/forced response optimization paying special attention to robustness considerations.

5.1 Stability Optimization

From a practical standpoint we wish to maximize the stability extension $s(z)$ while keeping the "side effects" of mistuning acceptable. Here side effects refers to everything from increased weight and manufacturing cost to a decrease in operating range [SF76] due to mistuning. To solve the true optimal problem we would quantify all the possible side effects (such as cost, weight, operating range and many others) and form a constrained optimization problem where we maximize $s(z)$ subject to the constraint that side effects remain below some practically motivated boundary. Clearly, such an approach is too ambitious. At present we do not know how to quantify increase in cost, operating range and other factors as a function of mistuning. Furthermore, there is no way to compose a complete list of all possible side effects. Consequently, an optimization problem thus obtained will almost certainly be intractable due to complexity of constraints. To start, we simply restrict the size

of mistuning and assume that resulting side effects are acceptable if z is sufficiently small. In Section 5.2 we shall include the most important side effect: the constraints due to forced response and high-cycle-fatigue.

5.1.1 Continuous Optimization

This problem is concerned with the design of optimal blades. Meaning, we place some constraints on the allowable mistuning, solve this optimization problem, and then build blades with the desired mistuning properties. For this first problem our constraint is simply mistuning size, and so we must pick an appropriate mistuning norm. To motivate the norm chosen consider a blade stiffness mistuning. Manufacturing and weight considerations would allow some small variation in each blade, so: $|z_i| \leq \epsilon$ for all i. This leads to a natural optimization problem constrained by the infinity norm on z:

1 *Optimization: Maximize* $s(z) = a\sum_{i=1}^{r} z_i + z^T S z + O(\|z\|^3)$ *subject to* $\|z\|_\infty \leq \epsilon$.

Having formulated the optimization problem, we can determine if mistuning is beneficial. Of course it is understood that we are judging the benefit based on the model chosen to represent the cascade.

We show that mistuning only makes sense if mistuning size ϵ is sufficiently large compared to a ratio of linear (a) to quadratic $(b, c_1, \ldots, c_k)$ terms in equation (4.16). Recall equation (4.17),

$$s(z) = a\sum_{i=1}^{r} z_i + z^T S z + O(\|z\|^3) \tag{5.1}$$

where S is a real, symmetric, cyclic matrix containing the quadratic coefficients $b, c_1, \ldots, c_k$ and z^T is the transpose of z. Let

$$\begin{array}{lllll} \bar{z} & \textit{solution to:} & \max \; a\sum_{i=1}^{r} z_i & \text{subject to} & \|z\|_\infty \leq 1, \\ z^* & \textit{solution to:} & \max \; z^T S z & \text{subject to} & \|z\|_\infty \leq 1, \; \sum_{i=1}^{r} z_i = 0. \end{array}$$

By inspection, $\bar{z} = (1, 1, \ldots, 1)$, and corresponds to a mean *tuned* increase in parameters (assume $a > 0$, else reverse sign of $\bar{z}$). Conversely, z^* corresponds to a zero average mistuning

which optimizes $s(z)$ up to second order (assume $S \not\leq 0$ and hence $z^* \neq 0$). If we impose a zero average restriction and truncate third-order terms, then optimization $\{1\}$ has solution ϵz^*. Furthermore, $\|z^*\|_\infty = 1$ else $z^{*T} S z^*$ may be increased by $z^* \mapsto (1+\delta)z^*$.

Now ask the following practically motivated question: given an allowable size of mistuning ϵ, is it better to apply the optimal zero average mistuning z^* or just increase parameters all around by a tuned amount $\bar{z}$? So compare

$$s(\alpha \bar{z}) = (ar)\alpha + \left(\bar{z}^T S \bar{z}\right) \alpha^2 + O(\alpha^3) \tag{5.2}$$

$$s(\alpha z^*) = 0 + \left(z^{*T} S z^*\right) \alpha^2 + O(\alpha^3) \tag{5.3}$$

where $\alpha > 0$ is the size of mistuning. For sufficiently small α the tuned stability extension $s(\alpha \bar{z})$ is always greater since it has a non-zero linear term $(ar)\alpha$. However, $z^{*T} S z^*$ is typically greater than $\bar{z}^T S \bar{z}$ because z^* is the constrained quadratic optimum (note $z^* \neq \bar{z}$) and hence $(z^{*T} S z^*)\alpha^2$ eventually overtakes $(ar)\alpha + (\bar{z}^T S \bar{z})\alpha^2$ (see Fig 5.1). Such a crossover occurs at

$$\alpha^* = \frac{ra}{z^{*T} S z^* - \bar{z}^T S \bar{z}}. \tag{5.4}$$

Based on this second order analysis: if $\alpha^* < \epsilon$ then ϵ-sized zero-average mistuning is worthwhile ($s(\epsilon z^*) > s(\epsilon \bar{z})$), otherwise it is not. Rephrasing, a zero-average mistuning is only worthwhile if it is bigger than α^*. Of course the second order approximation may fail at α^* if α^* is too large in which case we can not make any claims. Notice that α^* is small if second-order coefficients $(b, c_1, \ldots, c_k)$ dominate the first order coefficient a. Clearly α^* measures the mistuning sensitivity (as first mentioned in Section 4.4.1).

It is now clear that our results allow the reader to judge when to apply mistuning, based on the model (3.1). However, they also determine which mistuning should be applied. This is done by solving the optimization $\{1\}$ up to second order—a standard linear constraint quadratic programming problem. There exist numerical techniques [AKLV95] which can find global maximums of $a \sum_{i=1}^r z_i + z^T S z$ subject to $\|z\|_\infty \leq \epsilon$. Current software (supplied by F. Al-Khayyal, T. Van Voorhis and the company CPLEX) can usually solve problems up to $r \approx 30$. Larger optimizations take too long ($r = 60$ is projected to take years) but it is possible

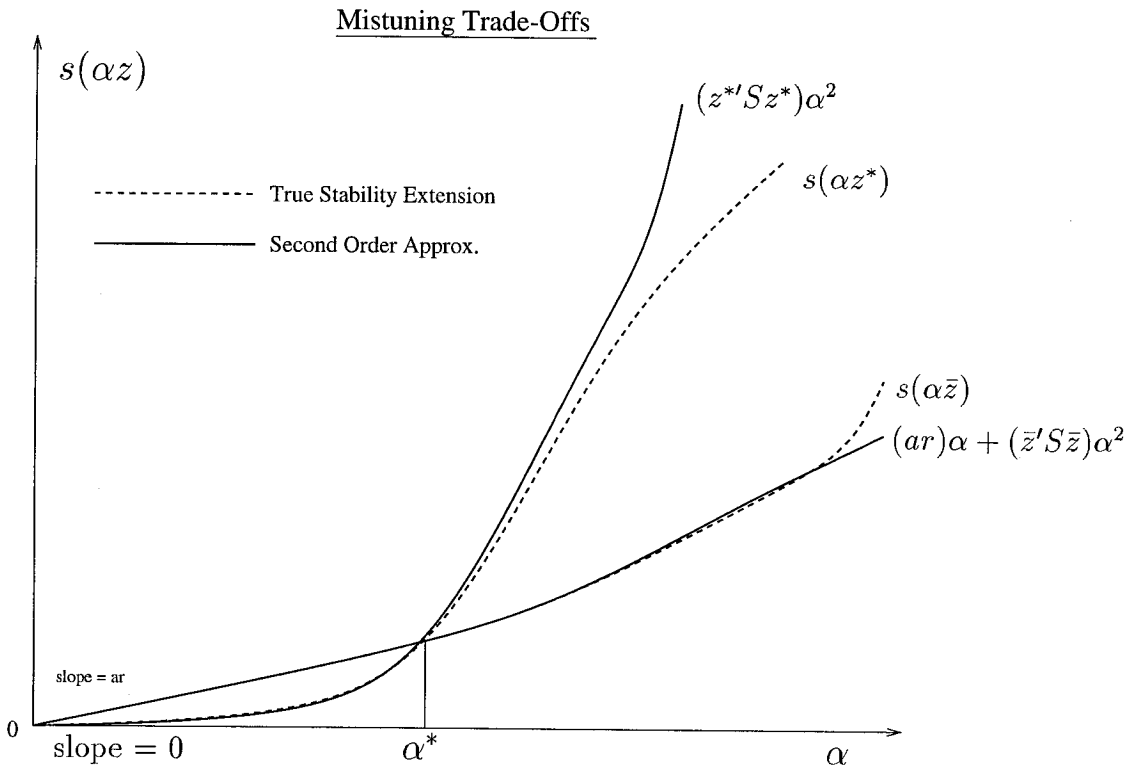

Figure 5.1: Worthwhile mistuning lower bound.

that computation time can be decreased dramatically by utilizing the special structure of S. In fact, because general quadratic programs are provably NP hard [MK87], solutions to large optimal mistuning problems will not be possible *unless* one exploits the special symmetry and structure of the mistuning problem. Such exploitation of problem structure—and the resulting dramatic decrease in computational complexity—is demonstrated in section 5.1.2.

Example: Quasi-Steady Model (continued)

For the quasi-steady model of Section 4.6, to determine the optimal zero average stiffness mistuning we numerically solve the optimization problem {1} up to second order, subject to the additional constraint $\sum_{i=1}^{r} z_i = 0$. The optimal solution ϵz^* has the form $z^* = (1, 1, 1, 1, 1, 0, -1, -1, -1, -1, -1)$. Of course all rotations, reflections and sign inversions of ϵz^* are also optimal because $z^T S z$ is invariant under rotation, reflection and sign change of z. This yields a total of $2r$ equivalent optimums. This type of mistuning differs markedly from the ad-hoc choices found in the literatures (e.g., alternate blade and random mistuning).

To answer the question of sensitivity to mistuning, we compute α^* of equation (5.4) and obtain $\alpha^* = 0.18$. So based on the quasi-steady model in Section 4.6, zero average optimal mistuning is only worthwhile if it is bigger than 18% ($\epsilon > 0.18$ in the optimal solution ϵz^*). We can increase the mistuning sensitivity by decreasing the size of the blade coupling in the model (see discussion of Section 4.4.1).

We note that the optimal mistuning problem seems to have a robust structure with respect to model parameters. Based on a limited parameter search, small changes in system parameters and/or operating conditions such as nominal rotor stiffness, blade mass, and stagger angle do not change the optimal answer. Even though the coefficients $a, b, c_1, \ldots, c_k$ change slightly, the optimal solution remains unchanged. However, changing the type of model significantly changes coefficients and optimization results.

5.1.2 Discrete Optimization

Mistuning can, at first glance, lead to computationally complex optimization problems. For example, suppose n blades are made and these blades have a set of mistuning values (say stiffness variations) $y_1, y_2, \ldots, y_n$ due to machining tolerances. Given the stability coefficients $a, b, c_1, c_2, \ldots, c_k$ and assuming y_i's are known (measurable), what is arrangement of the r blades that maximizes stability? If we wanted to solve the problem exhaustively, we would have to check n permute r or $n!/(n-r)!$ possibilities. Clearly this is not practical for large r or n; even the special case $n = r$ requires $r!$ operations. One solution can be found in random start (global) optimization techniques, such as random seed gradient descent or genetic algorithms. These techniques are fast but provide no guarantee of approaching the global optimum. Another option is to use techniques that exhaustively search the parameter space such as branch and bound methods. These methods guarantee global optimums but are not practical for large problems due to computational complexity. Neither option yields global optimums for large problems. Moreover, standard packages for both random start and exhaustive search algorithms do not exploit system symmetry. Yet, exploiting system structure can result in tremendous complexity reduction. Specifically, the circular structure of the mistuning problem *and* the additional structure of the stability coefficients c_i found

in the quasi-steady model (see Section 4.6.1, Table 4.2) allows (a globally optimal) solution of the $n = r$ combinatorial optimization in closed form.

Monotonically Decreasing Stability Coefficients

Consider the set of models where stability coefficients satisfy the relation

$$c_1 > c_2 > \cdots > c_{k-1} > c_k, \ r \text{ odd}, \tag{5.5}$$

$$c_1 > c_2 > \cdots > c_{k-1} > 2c_k, \ r \text{ even}. \tag{5.6}$$

Condition (5.5) or (5.6) holds for the quasi-steady model of Section 4.6 over a fairly broad range of parameter values. This condition is not true in general, but it does hold for a class of models. (See Section 4.5 for a discussion of the structure of coefficients c_i.) When condition (5.5) or (5.6) holds, the problem

2 *Combinatorial Optimization: Given mistuning values* $(y_1, y_2, \ldots, y_r)$*, the stability coefficients* $(a, b, c_1, \ldots, c_k)$ *that satisfy condition (5.5) or (5.6) and the resulting matrix* S *of equation (4.17); maximize* $s(z) = a\sum_{i=1}^{r} z_i + z^T S z$ *subject to* $z \in \Pi = \{z : z = (y_{l_1}, y_{l_2}, \ldots, y_{l_r}), l_i \neq l_j, \forall i \neq j\}$.

may be solved closed form. Optimization {2} is not restricted to mistuning applications. An identical optimization arises in computer science—related to optimal arrangement of records to be searched—and its statement and terse solution can be found in Knuth [Knu73, p.405, Q18 & Q20]. Optimal solutions are all rotations and reflections of the "pyramid" arrangement $z = (z_1, z_2, \ldots, z_r)$ where $z_{k+1} \geq z_k \geq z_{k+2} \geq z_{k-1} \geq \cdots \geq z_{r-1} \geq z_2 \geq z_r \geq z_1$ for r even or $z_{k+1} \geq z_k \geq z_{k+2} \geq z_{k-1} \geq \cdots \geq z_2 \geq z_{r-1} \geq z_1 \geq z_r$ for r odd (see Fig 5.2). So computational complexity drops from $r!$ to $r \log r$ which is the sorting time for r objects [Knu73].

The proof presented here follows Knuth [Knu73]. We show the r odd case but r even is almost identical, the only difference being the factor of two that multiplies c_k in (5.6). First note that the solution to {2} is independent of the coefficients a and b because the relevant terms $a\sum_{i=1}^{r} z_i$ and $b\sum_{i=1}^{r} z_i^2$ are invariant under permutations of z. So without

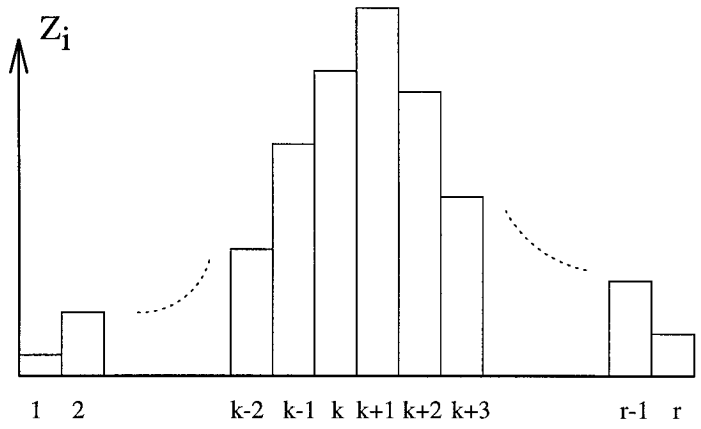

Figure 5.2: Optimal "pyramid" arrangement (r even).

loss of generality we may consider the objective function $z^TCz = z^T(S - bI)z$ which depends on coefficients c_i only. Now, for any z make one of two identifications (here β and δ are placeholder variables)

$$z = (\alpha_1, \alpha_2, \ldots, \alpha_k, \beta, \gamma_k, \ldots, \gamma_2, \gamma_1) \tag{5.7}$$

$$z = (\alpha_1, \alpha_2, \ldots, \alpha_k, \gamma_k, \ldots, \gamma_2, \gamma_1, \delta) \tag{5.8}$$

and define the sets

$$A = \{i : \alpha_i < \gamma_i, i \in (1, 2, \ldots, k)\}, \tag{5.9}$$

$$B = \{i : \alpha_i = \gamma_i, i \in (1, 2, \ldots, k)\}, \tag{5.10}$$

$$C = \{i : \alpha_i > \gamma_i, i \in (1, 2, \ldots, k)\}. \tag{5.11}$$

Consider switching α_i and γ_i when $\alpha_i > \gamma_i$, hence switch for all $i \in C$. For both (5.7) and (5.8) it can be shown that the resulting change in the objective function z^TCz is given by

$$\Delta = \sum_{i \in C, j \in A} \left(c_{|i-j|} - c_{l(i,j)}\right)(\gamma_j - \alpha_j)(\alpha_i - \gamma_i) \tag{5.12}$$

where

$$l(i,j) = \begin{cases} i+j-h & , \ i+j-h \le k \\ r-(i+j-h) & , \ i+j-h > k. \end{cases} \tag{5.13}$$

and h is 1 or 0 depending on whether we consider (5.7) or (5.8), respectively. It follows that $|i-j| < l(i,j)$ for all i,j in $(1,2,\ldots,k)$. Hence $c_{|i-j|} > c_{l(i,j)}$ by condition (5.5), and the terms $(\gamma_j - \alpha_j)$ and $(\alpha_i - \gamma_i)$ are strictly positive by definition of sets A and C. Consequently, $\Delta > 0$ unless either A or C is empty. In other words, we can improve on z in (5.7) or (5.8) if both A and C are non-empty. It turns out that only the "pyramid" arrangement of Figure 5.2 has either A or C empty for all rotations and reflections, hence it is the only arrangement that cannot be improved by the construction (5.5–5.13).

Next, recall that optimums come in sets of $2r$—if z^* is an optimum then so is any rotation or reflection of z^*. (Since a reflection about z_i^* is equivalent to a reflection about z_1^* and $2(i-1)$ rotations, we really only have one reflection and r rotations for a total of $2r$ equivalent optimums.) So suppose an optimal solution z^* of problem $\{2\}$ is not a rotation or reflection of the pyramid arrangement. Rotate z^* so that $z_p^* = \max_i z_i^*$ appears in the $(k+1)$th spot (if there is more then one maximum then pick any of these maxima) and reflect z^* about z_{k+1}^* if $z_k^* < z_{k+2}^*$. These two operations yield an equivalent optimum and imply $z_{k+1}^* \ge z_k^* \ge z_{k+2}^*$.

Since z^* is not a rotation or reflection of the "pyramid" arrangement then one of the inequalities in the top row of (5.14) must fail. The middle and bottom row correspond to the same chain of inequalities using the relabeling of (5.7) and (5.8), respectively,

$$\begin{bmatrix} z_{k+1}^* \\ \beta \\ \gamma_k \end{bmatrix} \ge \begin{bmatrix} z_k^* \\ \alpha_k \\ \alpha_k \end{bmatrix} \ge \begin{bmatrix} z_{k+2}^* \\ \gamma_k \\ \gamma_{k-1} \end{bmatrix} \ge \begin{bmatrix} z_{k-1}^* \\ \alpha_{k-1} \\ \alpha_{k-1} \end{bmatrix} \ge \cdots \ge \begin{bmatrix} z_2^* \\ \alpha_2 \\ \alpha_2 \end{bmatrix} \ge \begin{bmatrix} z_{r-1}^* \\ \gamma_2 \\ \gamma_1 \end{bmatrix} \ge \begin{bmatrix} z_1^* \\ \alpha_1 \\ \alpha_1 \end{bmatrix} \ge \begin{bmatrix} z_r^* \\ \gamma_1 \\ \delta \end{bmatrix}. \tag{5.14}$$

First consider the case where $z_{k+1}^* \ne z_k^* \ne z_{k+2}$, hence $z_{k+1}^* > z_k^* > z_{k+2}^*$. We have assumed z^* is not a "pyramid" arrangement so at least one of the inequalities in (5.14) must

fail. There are two possibilities: either $\alpha_i \geq \gamma_i$ fails in the middle row of (5.14) for some i or $\gamma_j \geq \alpha_j$ fails in the bottom row of (5.14) for some j. In the first possibility, $\gamma_i > \alpha_i$ so A is non-empty, but $z_k^* > z_{k+2}^*$ so $\alpha_k > \gamma_k$ and C must be non-empty. Hence Δ of equation (5.12) is positive, z^* can be improved by the construction of (5.5–5.13) and so z^* is not the optimum—a contradiction! Similarly, in possibility two $\alpha_j > \gamma_j$ so C is non-empty, but $\gamma_k > \alpha_k$ and hence A is non-empty. This also contradicts the assumption that z^* is optimal.

Now consider the cases where $z_{k+1}^* \neq z_k^* \neq z_{k+2}$ does not hold. When $z_{k+1}^* = z_k^*$ but $z_k^* \neq z_{k+2}^* \neq z_{k-1}^*$, then $z_k^* > z_{k+2}^*$ because z_k^* is a maximum of z^* and we may reflect so that $z_{k+2}^* > z_{k-1}^*$. Now we apply the same arguments as above except $\gamma_k > \alpha_k$ gets replaced by $\gamma_{k-1} > \alpha_{k-1}$ to ensure A is non-empty for the bottom inequality chain. The same reflection and right shift applies for the next case where $z_{k+1}^* = z_k^* = z_{k+2}^* \neq z_{k-1}^* \neq z_{k+3}^*$ and so on. Notice that we need at least two values of z^* different from the maximal value $z_p^* = \max_i z_i^*$, otherwise all arrangement are optimal. For example, if the mistuning values are $y_1 = y_2 = \cdots = y_{r-1} \neq y_r$ then all arrangements are equivalent by circular symmetry.

Arbitrary Stability Coefficients

When the stability coefficients $c_1, \ldots, c_k$ do not satisfy condition (5.5) or (5.6) the discrete optimization task {2} becomes much harder. There is no obvious way to extend the methods above to the arbitrary coefficients case because it is the coefficient monotonicity which enforces $\Delta > 0$ in equation (5.12) and allows an analytic solution. This leaves three choices:

1. Develop discrete optimization tools that exploit symmetry but do not require coefficient monotonicity (for the approximate or exact stability increase).

2. Optimize on the exact stability extension by standard discrete optimization techniques.

3. Optimize the approximate stability extension $s(z) \approx z^T S z$ by using standard discrete optimization techniques.

Clearly, choice one is the most challenging and desirable (at this time there are no techniques which allow this option). Choice two is the next best solution and is acceptable for low complexity models. Choice three must be used when computation in two is prohibitive.

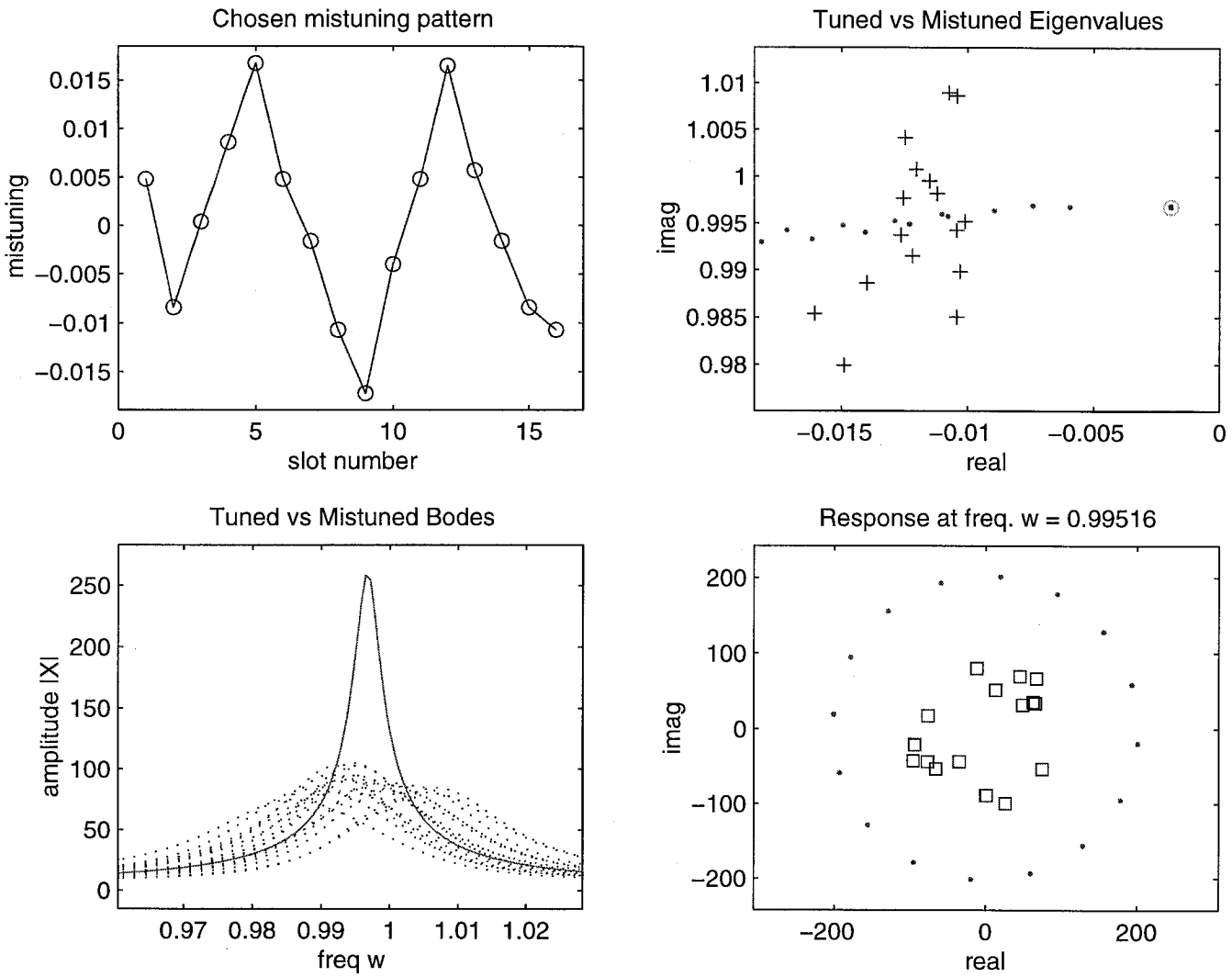

Figure 5.3: Optimal combinatorial mistuning of UTRC fan. Top left: the mistuning pattern. Top right: tuned eigenvalues (dots), mistuned eigenvalues (crosses) [circle denotes $\ell = 1$ spatial forcing]. Bottom left: tuned response (solid), mistuned response (dashed—all 16 blades). Bottom right: at fixed forcing frequency the tuned response (dots), mistuned response (squares).

As a demonstration, technique two was applied to a United Technologies Research Center (UTRC) fan with 16 blades. The model used was a linear, imposed periodic-motion model with two states per blade and structural dynamics modeled by a mass/spring system. Since the aerodynamic coefficients are only known at one loading (air-speed) the stability extension $s(z)$ is not defined. Instead all eigenvalues were pushed as far left as possible—an optimal damping increase.

Specifically, the deviation of each blade from the average natural frequency was measured and this provided the allowable mistuning values $y_1, y_2, \ldots, y_{16}$. Maximum mistuning size was 1.7%. The cost function used was the maximum real part of the eigenvalues: $c(z) = \max(\mathrm{Re}[\lambda(z)])$. Hence minimizing this function pushes all eigenvalues to the left. A random seed was used to start the optimization, and then the program would optimally switch neighbouring blades until a local optimum was found. The random seed would reset and a new search would commence. The best local optimum after twenty thousand iterations is shown in Figure 5.3.

Notice that the blade coupling here is very small, so even a small amount of mistuning will cause a very large change in eigenvalues. Hence the mistuning pattern shown is outside the $O(\|z\|^2)$ range where our eigenvalue/vector approximation applies.

5.2 Combined Forced Response/Stability Optimization

Of all the mistuning "side-effects," forced-response with its associated high-cycle-fatigue is most important. Our current step is to consider optimization for both stability and forced response. To do so we must first consider some engineering tradeoffs.

5.2.1 Engineering Tradeoffs

Engineering design tradeoffs are summarized below. These tradeoffs are based on symmetry arguments (Section 3) and hold for any model. Figure 5.4 show a schematic of the mistuning space $\mathbb{R}^r$ for a fixed forcing frequency ω and spatial forcing mode ℓ: light-gray regions correspond to an acceptable forced response, medium-gray denotes unacceptable response

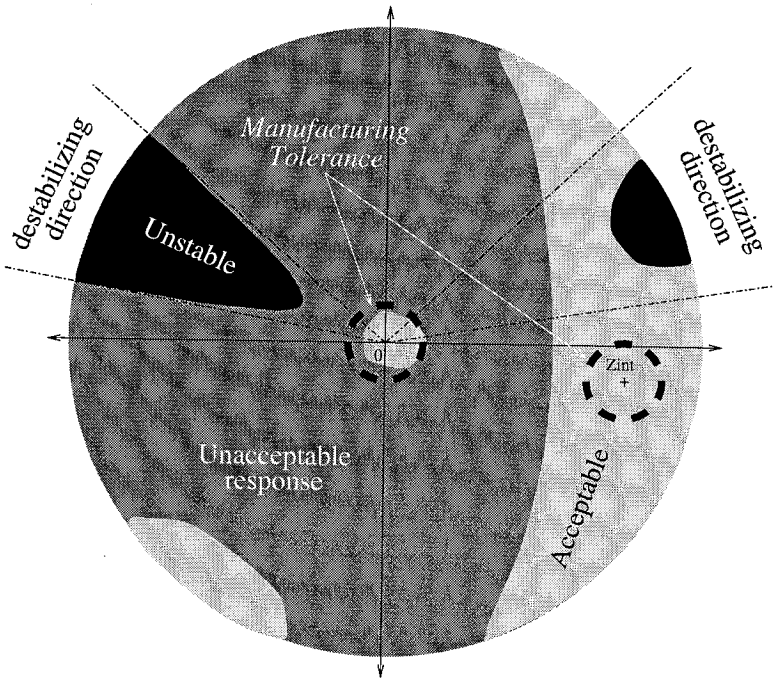

Figure 5.4: Intentional mistuning for robustness under manufacturing uncertainty.

and black regions show instability. (We shall prove this figure shortly.)

There is a small region of acceptable response about the origin. Blades are produced within some manufacturing tolerance (dotted black circle). For simplicity, lets assume blades are distributed uniformly within this manufacturing region. (For a non-uniform distribution, the results are essentially the same except that factors must be normalized by the relevant distribution.) In Figure 5.4 there is a sliver of unacceptable response inside the manufacturing tolerance region. Hence, the probability of unacceptable response is given by:

$$\text{probability of failure} = \frac{\text{area of unacceptable sliver inside tolerance}}{\text{area of manufacturing tolerance}}. \tag{5.15}$$

This probability increase if:

1. Manufacturing tolerance increases.

2. Damping decreases: leads to smaller acceptable response region.

3. Allowable blade amplitude decreases: again smaller acceptable region.

Basically, there exist competing tradeoffs. Engine manufacturers cannot decrease cost (loosen manufacturing tolerances) *and* increase performance (decrease damping) *and* lengthen blade-life (lower blade response amplitudes). In fact, if we fix the allowable failure probability there exists a linear constraint between tolerance, damping and vibration amplitude:

$$K \times \text{manufacturing tolerance} \leq \text{damping} \times \text{allowable blade response} \tag{5.16}$$

(K is a computable constant). Hence, it is not possible to reduce cost and prolong engine life and increase performance all at the same time if one designs around the tuned point.

5.2.2 Robust Optimization

Fortunately, mistuning itself may be used to combat mistuning sensitivity. If we introduce the intentional mistuning z_{int} shown in Figure 5.4 we can guarantee acceptable response under the same manufacturing tolerance. Here z_{int} could be continuous or discrete, the only requirement is that it push all lightly damped eigenvalues to the left. (Or less conservatively, if we know the forcing frequencies appear in some range $w_l < w < w_u$, we need to ensure all eigenvalues with imaginary part in this range $w_l < \text{Im}[\lambda(z)] < w_u$ have been moved sufficiently far to the left.) Since eigenvalues move quadratically with mistuning, we must jump across the linear range where eigenvectors are breaking symmetry and increasing the forced response before we see a benefit due to improved damping. Hence intentional mistuning z_{int} essentially creates robust damping. Figure 5.4 is derived up to quadratic terms $O(\|z\|^2)$ but of course the concept holds more generally. If there exists a large region in z space that pushes all lightly-damped eigenvalues to the left, then the mistuning value at its center (for small or large mistuning) will create robust improved stability and forced-response.

To demonstrate the tradeoffs above we use the specific model of Section 4.6. However, these tradeoffs are based on symmetry arguments and hold in general. Suppose our conceptual factory produces blades whose stiffnesses vary uniformly between $0.98\,k_0$ and $1.02\,k_0$. Blade life is deemed acceptable if blades vibrate less then ten times the tuned amount: $\|X(z)\| \leq 10\,\|X(0)\|$. We consider the resonance forcing frequency $\omega = 0.0376$ (see Figure 4.17). By Monte Carlo simulation we find that there is a 9.5% probability of instability and a

4.6% probability of unacceptable response. This means that both the black unstable regions and dark-grey unacceptable response regions penetrate the manufacturing tolerance circle of Figure 5.4. Together, there is a 14.1% probability system behaviour is unacceptable.

For simplicity, let us consider how zero average mistuning, $\sum z_i = 0$, effects stability and forced response. We want to understand dependence on the magnitude of mistuning. Consider a mistuning direction $\hat{z}$ with $\sum \hat{z}_i = 0$ on the unit ball $\|\hat{z}\| = 1$ and let mistuning z vary along this direction as $z = \epsilon\hat{z}$ (along a ray from the origin in Figure 5.4). From (4.78), each eigenvalue $\lambda_j^d(\epsilon\,\hat{z})$ varies as

$$\mathrm{Re}[\lambda_j^d(\epsilon\hat{z})] \approx -\eta - k_1\epsilon^2. \tag{5.17}$$

with $\eta = -\mathrm{Re}[\lambda_j^d(0)]$ the tuned damping. If $\hat{z}$ is stabilizing then $k_1 = k_1(\hat{z}) > 0$, else $k_1 \leq 0$. Destabilizing directions $\hat{z}$ yield the black quadratic regions in Figure 5.4 where ϵ becomes sufficiently large to move $\lambda_j^d(z)$ into the right-half-plane.

At resonance frequency $\omega = 0.0376$ the mistuned forced response is dominated by the least damped mode $\lambda_9^3(z)$ (see Figure 4.15). Hence equation (4.92) implies

$$\|X(\epsilon\hat{z})\| \approx \frac{k_0\epsilon}{\eta + k_1\epsilon^2}. \tag{5.18}$$

For $\hat{z}$ stabilizing ($k_1 > 0$) tradeoff (5.18) is shown in Figure 5.5. This curve has been determined numerically in [KP96] and [CP97] by extensive computations. However, both papers have not been able to explain its shape. In our case, symmetry provides a straightforward explanation. Rotation invariance (Lemma 3.6.1) implies eigenvalues vary quadratically with mistuning (the $\eta + k_1\epsilon^2$ term in the denominator of (5.18)) while eigenvectors are permitted to vary linearly (the $k_0\epsilon$ term in the numerator). In the $\hat{z}$ stabilizing case, the response first climbs linearly as k_0/η (mistuned modes appear as in Figure 4.11) and then sinks quadratically as eigenvalues move into the left-half-plane. Light damping (small η) causes a fast linear growth.

If we choose A as the acceptable blade vibration, then the leftmost estimate of Figure

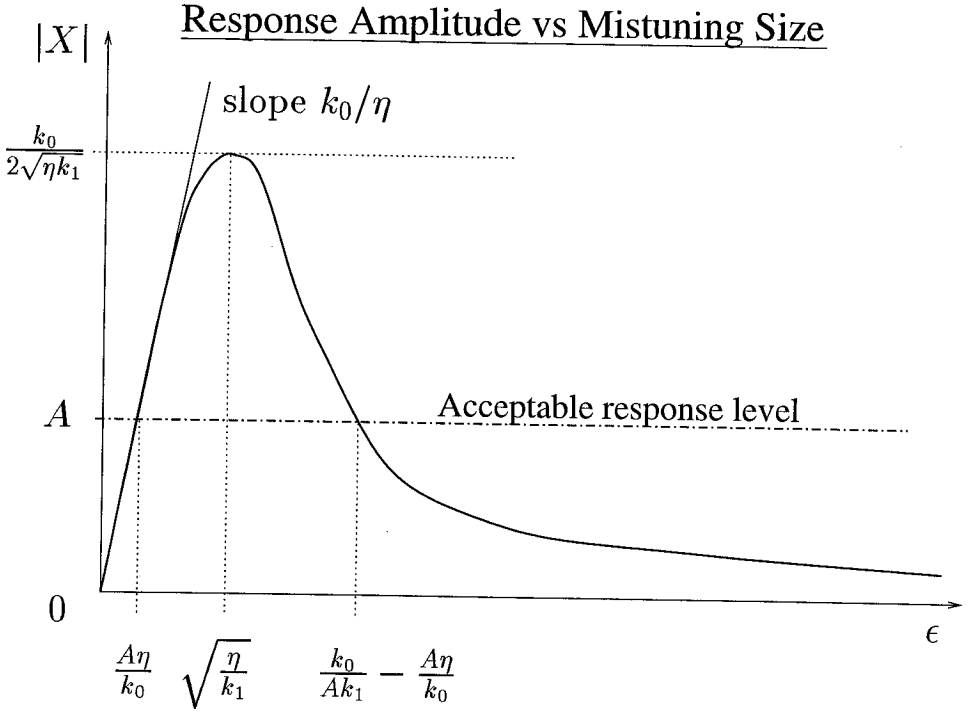

Figure 5.5: Response sensitivity to mistuning size (5.18).

5.5 yields the allowable manufacturing tolerance

$$\|z_{\text{manuf}}\| \leq \frac{A\eta}{k_0}. \tag{5.19}$$

We could find the minimum estimate (using $\max k_0(\hat{z})$) by varying $\hat{z}$ over the unit ball $\|\hat{z}\| = 1$. This would yield the radius of the biggest ball that can be contained within the acceptable region at the origin in Figure 5.4. Equation (5.19) is equivalent to tradeoff (5.16).

Varying $\hat{z}$ and ϵ together recovers Figure 5.4. Coefficients k_0 and k_1 vary with $\hat{z}$ so that different directions have different sections of acceptable and unacceptable response. To pick an intentional mistuning z_{int} we must find a stabilizing direction $\hat{z}$ (see Section 5.1) and pick ϵ beyond the right-hand intersection

$$\epsilon^* = \frac{k_0}{Ak_1} - \frac{A\eta}{k_0} \tag{5.20}$$

of Figure 5.5: $z_{\text{int}} = \epsilon\hat{z}$ with $\epsilon > \epsilon^*$. Now an additional small random mistuning $z = z_{\text{int}} + z_{\text{manuf}}$ will shift us along the gentle right-hand portion of (5.18).

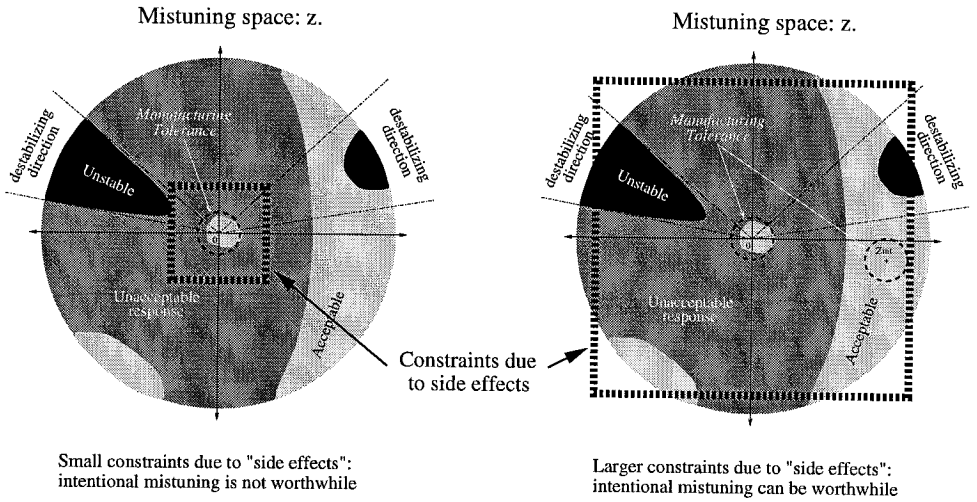

Figure 5.6: Constraints must be large enough to allow robust intentional mistuning.

Suppose, as in Section 5.1, that we have additional "side-effects" that limit the size of our mistuning. Then if the allowable mistuning size is large enough to permit an intentional mistuning within one of the acceptable regions outside the origin in Figure 5.4, we can introduce a sensible intentional mistuning. Otherwise, we are restricted to the small acceptable region about the origin (see Figure 5.6). We must have enough allowable mistuning size to be able to jump outside the linear range (where eigenvectors have broken symmetry but eigenvalues have not moved left substantially) into the quadratic or higher range (where we can introduce appreciable damping through eigenvalue motion).

Example: Quasi-Steady Model (continued)

Numerical results for the model of Section 4.6 are shown graphically in Figure 5.7. Here we have fixed the spatial forcing to $\ell = 1$. Recall, for a 2% manufacturing tolerance there is a 4.6% probability of unacceptable response. We choose a specific manufacturing mistuning $\|z_{spec}\| \leq 2\%$ such that $X(z_{spec})$ is unacceptable. (Hence z_{spec} lies in the unacceptable sliver inside the manufacturing tolerance region of Figure 5.4.) Resulting amplitude of all the blades $|X_i(z_{spec})|$ is plotted as thin-lines in Figure 5.7. The mistuned response is far above the acceptable limit A (dashed-line)

$$\|X(z_{spec})\|_\infty = \max_i |X_i(z_{spec})| \gg 10\,\|X(0)\|_\infty = A. \tag{5.21}$$

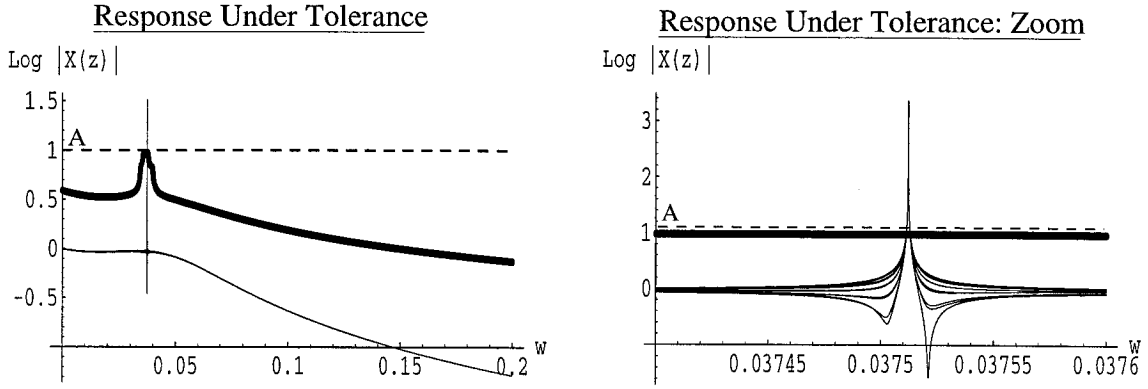

Figure 5.7: Response under manufacturing tolerance: acceptable level A - dashed-line; bound for $|X(z_{\text{int}} + z_{\text{manuf}})|$ - thick-line; amplitude $|X(z_{spec})|$ of all blades - thin-lines.

Now pick the intentional mistuning

$$z_{\text{int}} = \epsilon \hat{z} = 0.1(1, 1, 1, 1, 1, 0, -1, -1, -1, -1, -1).$$

Here $\hat{z}$ is chosen by an eigenvalue optimization as in Section 5.1.1 while $\epsilon = 0.1$ is larger then ϵ^* of equation (5.20). Using the triangle inequality it is possible to find a rigorous and very conservative bound for the intentionally mistuned response $X(z_{\text{int}} + z_{\text{manuf}})$ under manufacturing uncertainty $\|z_{\text{manuf}}\| \leq \Delta = 2\%$, namely

$$|X(z_{\text{int}} + z_{\text{manuf}})| \leq \sum_{j=0}^{r-1} \sum_{d=1}^{m} \frac{\mathcal{N}_j^d(z_{\text{int}}, \Delta)}{\mathcal{D}_j^d(z_{\text{int}}, \Delta)}, \quad \text{for any } \|z_{\text{manuf}}\| \leq \Delta \tag{5.22}$$

where

$$\mathcal{N}_j^d(z_{\text{int}}, \Delta) = \max_i \left| \alpha_0^{j,d} + \left[\alpha_1^{j,d}, \cdots, \alpha_r^{j,d} \right] \varphi^i z_{\text{int}} \right| + \Delta \left(|\alpha_1^{j,d}| + \cdots + |\alpha_r^{j,d}| \right)$$

and

$$\begin{aligned} \mathcal{D}_j^d(z_{\text{int}}, \Delta) \;=\; & \left| \left(-\text{Re}[\lambda_j^d(z_{\text{int}})] - \left[r\Delta |\text{Re}[\sigma_{j,d}]| + r\Delta^2(2N+1)|\text{Re}[\Phi_{j,d}]| \right] \right) \right. \\ & \left. + i \left| \, |\omega - \text{Im}[\lambda_j^d(z_{\text{int}})]| - \left| \left(r\Delta \text{Im}[\sigma_{j,d}] + r(2N+1)\Delta^2 |\text{Im}[\Phi_{j,d}]| \right) \right| \right| \end{aligned}$$

with $|\mathrm{Re}[\Phi]| = |\mathrm{Re}[\phi]| + |\mathrm{Re}[\psi_1]| + \cdots + |\mathrm{Re}[\psi_k]|$ or take imaginary part as appropriate. Here, bounds on $\lambda(z_{\mathrm{int}})$ are given by (4.78). Equation (5.22) bounds the forced response under intentional mistuning z_{int} with manufacturing uncertainty. (Note that the bound only holds if the second order mistuning perturbation is accurate.) This forced response bound is shown as the thick-line in Figure 5.7. Clearly it falls below A for all forcing frequencies ω. Thus, the introduction of intentional mistuning z_{int} guarantees stability and acceptable response under manufacturing tolerance.

Chapter 6 Application to a High-Fidelity Low-Order (HFLO) Model

All the mistuning techniques presented so far have been applied to simple, and correspondingly low-fidelity, test models. In this chapter the mistuning analysis methods are used to analyze a high-fidelity model derived from CFD data [WPP99] by proper orthogonal decomposition (POD) [Sir87]. Methods derived in Chapters 3, 4 and 5 are applied to this model. The mistuning behaviour and sensitivity predicted analytically in Chapter 4 is demonstrated numerically. Moreover, based on the results of Chapter 5 we show that there exists an intentional mistuning that robustly improves both stability and worst-case forced response under manufacturing tolerances. This chapter is a joint work: modeling results are due to Karen Willcox at MIT while the mistuning analysis and optimization results are based on the mistuning framework in this thesis.

6.1 Generating a HFLO Aerodynamic Model

In the modeling of bladed-disks, resolution of the aerodynamics presents a significant challenge. One approach is to use high-fidelity computational-fluid-dynamic (CFD) solvers to resolve the unsteady Euler or Navier Stokes equations directly. Even though the methods of Chapter 3 hold for CFD models, it is not possible to compute the quantities of Chapter 4 for these complex models. The size of CFD models makes them unsuitable for mistuning analysis. A second approach is to use exploit simplifying fluid dynamic assumptions (two-dimensional, inviscid, incompressible flow, flat-plate blades, etc.) or to develop models based on phenomenological intuition (as blade passage size increases, blade force should increase—see Chapter 2 model). Such methods provide limited information at low-fidelity and are typically not useful in complex flow conditions such as transonic, stalled or off-design flows. An intermediate approach is to project the high-fidelity CFD model onto a set of basis

vectors so as to create low-order high-fidelity model amenable to mistuning analysis.

This intermediate approach is developed in [WPP99]. Here, the unsteady aerodynamic equations (Euler or Navier Stokes) are written as

$$\dot{U} + R(U, X) = 0, \tag{6.1}$$

with U, X representing the large aerodynamic state and boundary conditions respectively. Assuming the aerodynamic state and boundary conditions are given by small variations from a steady solution, $(U, X) = (\tilde{U} + U', \tilde{X} + X')$, equation (6.1) is linearized about a steady-state solution of the CFD code: $R(\tilde{U}, \tilde{X}) = 0$. This yields a linear system of equations for the perturbations U' and X'

$$\dot{U}' + PU' = -\frac{\partial R}{\partial X} X' \tag{6.2}$$

where $P = \partial R / \partial U$ evaluated at $\tilde{U}, \tilde{X}$.

The boundary perturbation $X'(t)$ captures both the the time-varying domain geometry (such as blade deflection) and time-varying inlet/outlet flow conditions (such as inlet flow distortions or pressure disturbances). For example, if we consider blade plunge h and blade twist α as the allowable blade deflections, and we further allow the ℓth spatial fourier mode pressure disturbance $p(\theta, t) = \cos(\ell\theta + w_f t) = \mathrm{Re}[e^{i\ell\theta} e^{iw_f t}]$ then

$$-\frac{\partial R}{\partial X} X'(t) = f_h h(t) + f_{\dot{h}} \dot{h}(t) + f_\alpha \alpha(t) + f_{\dot{\alpha}} \dot{\alpha}(t) + f_\ell \cos(w_f t). \tag{6.3}$$

By combining fourier modes, any arbitrary disturbance in space and time may be represented. In general we have

$$\dot{U}' + PU' = f(H, D) = f_H H(t) + f_D D(t) \tag{6.4}$$

where $H(t)$ captures allowable blade deflections while $D(t)$ denotes outside forcing modes.

Equation (6.2) is transformed into the frequency domain via $U' = \bar{U} e^{iwt}$ and $f = \bar{f} e^{iwt}$. Both spatial blade deflections and outside forcing $\bar{f}$ can be decomposed into components

which contain a single spatial frequency $\bar{f}_j = [\hat{f}, p_j\hat{f}, \ldots, p_j^{r-1}\hat{f}]$. This allows the computational domain to be reduce to a single blade passage for each spatial frequency. Resulting solutions of the linearized, unsteady, CFD equations in the frequency domain

$$[P + iw]\bar{U} = \bar{f} \tag{6.5}$$

provide an image of the flow at each temporal frequency w, for each spatial frequency $\bar{f}_j$. Images are calculated over all possible spatial modes ($j = 1, 2, \cdots, r$), for a set of frequencies w within some range $w_L < w < w_U$. POD is used to convert these images (or snap-shots) into the most efficient set of basis-vectors—these basis vectors are optimal in the sense that they contain the most average "kinetic energy" ($U^T U$) per vector. Galerkin projection is now used to project the linearized fluid equations (6.4) onto the first rp basis vectors. Since the chosen basis vectors are optimal, even a small model (small p) will capture most of the energy of the original CFD code and so provide a low-order, high-fidelity aerodynamic description.

The final set of aerodynamic equations so developed in [WPP99] has the form

$$\dot{x} = Ax + Bu + E\dot{d} \tag{6.6}$$

$$y = Cx + Du + Fd. \tag{6.7}$$

Here $x \in \mathbb{R}^{rp}$ is the aerodynamic state with p POD modes per blade, $u \in \mathbb{R}^{rq}$ describes the instantaneous blade deflection (such as blade bending and torsion) with q deflection states per blade, $y \in \mathbb{R}^{rs}$ are the aerodynamic forces (such as lift and moment) with s forces per blade. Finally, $d(t)$ and $\dot{d}(t)$ capture the time-varying outside disturbance (for example pressure or velocity distortion at inlet) and E, F describe the spatial extent of this disturbance. If we consider g spatial disturbance frequencies, then $d, \dot{d} \in \mathbb{R}^g$.

It takes a significant amount of time to generate these aerodynamic models. For example, in the 20 blade model introduced in Section 6.4 with 6 POD modes per blade, the POD snapshots were sampled at 10 frequencies with 2 snapshots per frequency. This gave 20 snapshots per inter-blade phase angle, with one additional snapshot per angle to account

for a static correction. Hence a total of $21 \times 20 = 420$ POD snapshots were computed. This took approximately 20 hours of runtime on a DEC alpha 433MHz machine. The POD modes themselves were computed by generating a correlation matrix (here 40×40) and computing its eigenvalues and eigenvectors for each inter-blade phase angle. This portion took approximately 3 hours of runtime. Finally, the projection onto the $20 \times 6 = 120$ basis vectors took about 15 minutes and gave the final aerodynamic equations (6.6) and (6.7).

Coupling this aerodynamic model with a structural model

$$\dot{u} = P(z)u + Q(z)y. \tag{6.8}$$

provides the final set of system equations

$$\dot{u} = [P(z) + Q(z)D]u + Q(z)Cx + Q(z)Fd \tag{6.9}$$

$$\dot{x} = Ax + Bu + E\dot{d}. \tag{6.10}$$

(In Section 6.3, equations (6.9) and (6.10) have a slightly more complex form because the structural input u of equations (6.6) and (6.7) has more states then the structural model vector u of equation (6.8). Hence some components in equation (6.6) must be eliminated. See Section 6.3 for details.)

Since the CFD snapshots are taken within some frequency range $w_L < w < w_U$, the model described by equations (6.9) and (6.10) only holds within this range. Moreover, the above analysis assumes tuned aerodynamics—all the blades have the same shape. It does allow for a mistuned structural model as in equation (6.8). Finally, the fluid modeling limitations are inherited from the CFD code. So if the CFD code is two-dimensional and inviscid, the low-order model will not capture viscous, three-dimensional effects. However, the methodology of [WPP99] allows for a generation of low-order aerodynamic models from any (linearized) CFD code.

6.2 HFLO Model Validation

The low-order model generated in [WPP99] is based on an inviscid two-dimensional Euler CFD code. It was validated in three steps. First, the nonlinear steady-state CFD solver was validated against experimental data. Experimental steady-state pressure coefficients along the blade surface from a transonic cascade [SS84] were compared against pressure coefficients predicted by a nonlinear steady-state CFD calculation (Mach number 0.82, incidence angle 58.5 degrees). The blade shape and resulting data is shown in Figure 6.1. It can be seen

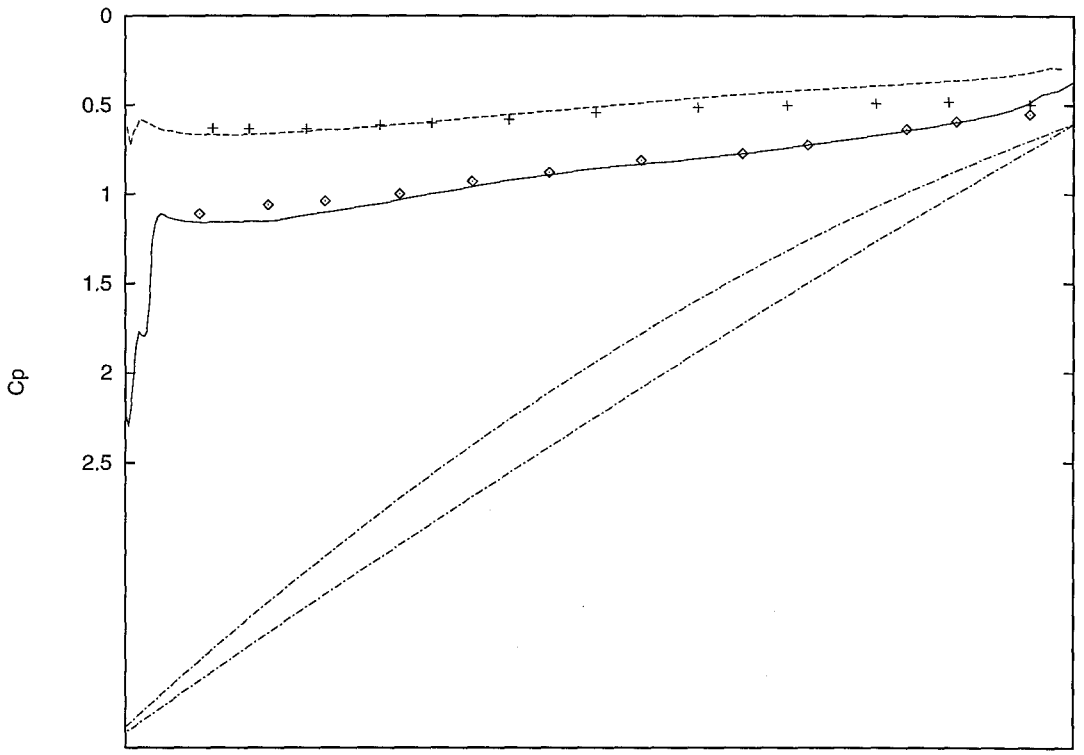

Figure 6.1: Steady pressure distribution along the DFVLR transonic blade: experimental (0,+) vs CFD (curves). (Figure courtesy K. Willcox)

that there is good agreement between experiment and computation. Figure 6.2 shows the corresponding steady-state pressure contours for the DFVLR transonic blade passage, the shock wave just past the leading edge can be seen clearly.

Second, the linearized unsteady CFD solver was compared against experimental data found in [BF86] which contains a database of well documented experimental cases for aeroelastic analysis of turbomachines. Data from a subsonic compressor stage was compared

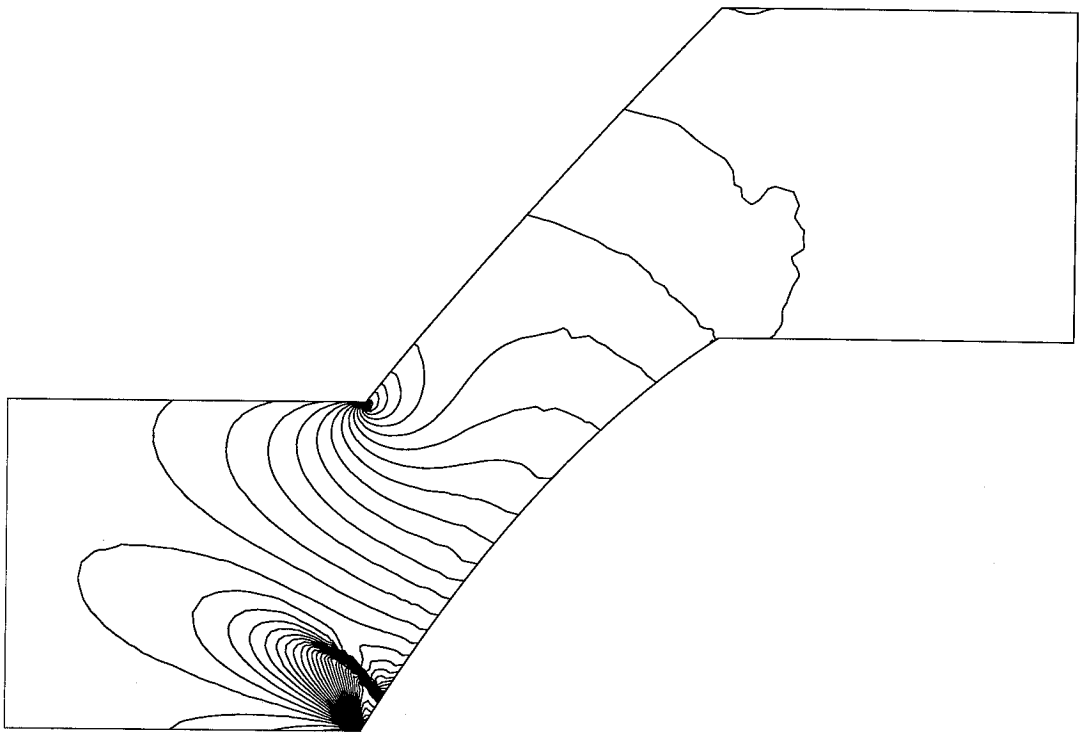

Figure 6.2: Blade passage pressure contours for the DFVLR blade. (Figure courtesy K. Willcox)

against simulation (inlet Mach number of 0.18, −66 degree angle of incidence). This cascade was analyzed in unsteady pitching motion at a reduced frequency of 0.122. Damping coefficients predicted by a work-per-cycle calculation using the inviscid, linearized, unsteady CFD code are shown versus experimental data in Figure 6.3. There is good agreement between experiment and computation. The agreement obtained using the linearized CFD solver is much better then that shown in [BF86] for other analytic methods. Numerical results for transonic, single airfoils were also compared against experiment and there was good agreement.

Third, the reduced aerodynamic POD model was compared against the linearized unsteady CFD solver. The comparison between the linearized CFD code and the low-order model determines if enough sample frequencies have been chosen for the POD snapshots. A comparison was performed for a four blade case. Here all four blades were displaced in a plunge pulse. Figure 6.4 shows the resulting lift versus time on all four blades computed by the linearized CFD code and derived from the low-order POD model. It was found

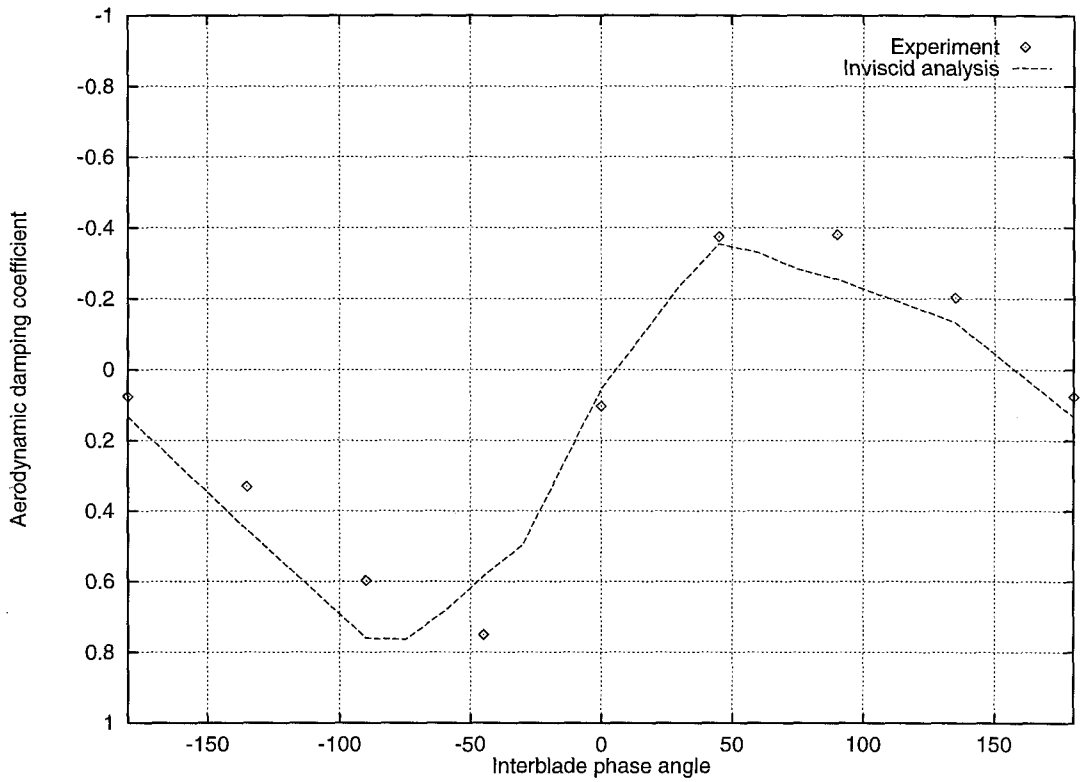

Figure 6.3: Experimental and numeric aerodynamic damping coefficients. (Figure courtesy K. Willcox)

that doing the same pulse comparison for four different blade motions (non-zero inter-blade phase angles) was not practical with the linearized CFD code due to large computations times. However, results for nonzero inter-blade phase angle for imposed blade sinusoidal motion showed excellent agreement between the linearized CFD solver and the low-order POD model.

6.3 Converting the HFLO Model into the Mistuning Framework

In [WPP99], some quantities are written in inter-blade phase angle coordinates. However, the formulation used here, starting with equation (3.1), is expressed only in blade coordinates. In order to be within the current framework, the HFLO model of [WPP99] is transformed into blade coordinates only. As a result, the block diagonal matrices A, B, C and D of equations

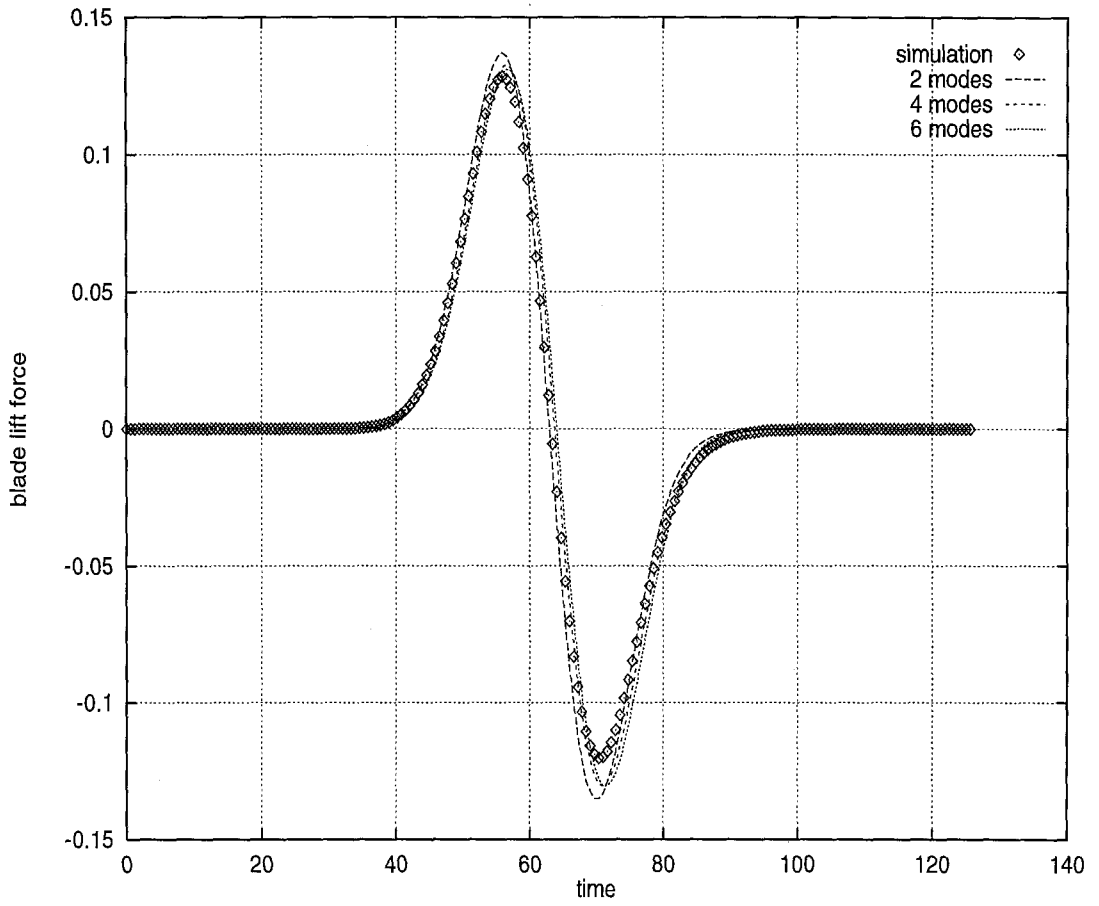

Figure 6.4: Pulse response for linearized CFD vs low-order model. (Figure courtesy K. Willcox)

(6.6) and (6.7) become block circular. So for a fixed spatial forcing mode ℓ, the aerodynamic equations have the form

$$\begin{bmatrix} \dot{x}_1 \\ x_2 \\ \vdots \\ x_r \end{bmatrix} = \begin{bmatrix} A_1 & A_2 & \dots & A_r \\ A_r & A_1 & A_2 & \dots \\ & \ddots & & \\ A_2 & A_3 & \dots & A_1 \end{bmatrix} \begin{bmatrix} x_1 \\ x_2 \\ \vdots \\ x_r \end{bmatrix} + \begin{bmatrix} B_1 & B_2 & \dots & B_r \\ B_r & B_1 & B_2 & \dots \\ & \ddots & & \\ B_2 & B_3 & \dots & B_1 \end{bmatrix} \begin{bmatrix} u_1 \\ u_2 \\ \vdots \\ u_r \end{bmatrix} + \begin{bmatrix} \bar{e} \\ p_\ell \bar{e} \\ \vdots \\ p_\ell^{r-1} \bar{e} \end{bmatrix} \dot{d}(t) \quad (6.11)$$

and

$$\begin{bmatrix} y_1 \\ y_2 \\ \vdots \\ y_r \end{bmatrix} = \begin{bmatrix} C_1 & C_2 & \dots & C_r \\ C_r & C_1 & C_2 & \dots \\ & \ddots & & \\ C_2 & C_3 & \dots & C_1 \end{bmatrix} \begin{bmatrix} x_1 \\ x_2 \\ \vdots \\ x_r \end{bmatrix} + \begin{bmatrix} D_1 & D_2 & \dots & D_r \\ D_r & D_1 & D_2 & \dots \\ & \ddots & & \\ D_2 & D_3 & \dots & D_1 \end{bmatrix} \begin{bmatrix} u_1 \\ u_2 \\ \vdots \\ u_r \end{bmatrix} + \begin{bmatrix} \bar{f} \\ p_\ell \bar{f} \\ \vdots \\ p_\ell^{r-1} \bar{f} \end{bmatrix} d(t). \quad (6.12)$$

Here $x_j \in \mathbb{R}^p, u_j \in \mathbb{R}^q$ and $y_j \in \mathbb{R}^s$ correspond to the aerodynamic states, blade deflections and aerodynamic forces on blade j. Block matrices $A_i \in \mathbb{R}^{p\times p}, B_i \in \mathbb{R}^{p\times q}, C_i \in \mathbb{R}^{s\times p}$ and $D_i \in \mathbb{R}^{s\times q}$ are commensurate with the dimensions of x, u and y. The component blocks $\bar{e} \in \mathbb{R}^p$ and $\bar{f} \in \mathbb{R}^s$ of the ℓth spatial mode disturbance vectors E and F depend on the type of disturbance considered and the spatial mode ℓ. Finally, $d \in \mathbb{R}$ and its time derivative $\dot{d}$ capture the time-dependence of the ℓth mode spatial disturbance. For the current model, y_j is simply the normalized lift on blade j and so $s = 1$. Vector $u_j = [h_j, \dot{h}_j, \ddot{h}_j]$ where h_j is the normalized plunge (down) of blade j. Hence u_j consists of blade displacement, velocity and acceleration and so $q = 3$. Finally, there are six aerodynamic states per blade hence $p = 6$.

Now that the aerodynamic results are in blade coordinates, or in block circular form, they can be coupled with a mistuned structural model to provide a closed set of equations that fits the current mistuning framework. The structural non-dimensional model is given by

$$\ddot{h}_j + 2\zeta\dot{h}_j + (1 + z_j)h_j = -\frac{2}{\pi\mu k^2} y_j. \quad (6.13)$$

Here $\mu = m/(\pi\rho b^2)$ is the mass ratio, ζ is the non-dimensional damping while $k = 2bw/U$ is the reduced frequency (m is blade effective mass, ρ is density of air, b is semi-chord, w is the tuned natural frequency and U is the free stream velocity). The non-dimensionalization is standard; plunge is normalized by the blade chord ($h \mapsto h/c$) while time is normalized by the reduced frequency, airspeed and chord ($t \mapsto kUt/c$). This normalization implies that $A \mapsto A/(kM)$; the columns of B which correspond to h and $\ddot{h}$ are transformed as $B_h \mapsto B_h/(kM)$ and $B_{\ddot{h}} \mapsto (kM)B_{\ddot{h}}$ respectively; the columns of D which correspond to $\dot{h}$ and $\ddot{h}$ are transformed as $D_{\dot{h}} \mapsto (kM)D_{\dot{h}}$ and $D_{\ddot{h}} \mapsto (kM)^2 D_{\ddot{h}}$ respectively. Finally,

structural mistuning is represented by z_j, the percent change in the natural frequency of blade j.

Aerodynamic description (6.11), (6.12) has a structural input of $u_j = [h_j, \dot{h}_j, \ddot{h}_j]$ while the structural equation (6.13) has a state of $v_j = [h_j, \dot{h}_j]$. Hence it is necessary to eliminate $\ddot{h}_j$ from equation (6.11) in order to provide a closed model (the terms $\ddot{h}_j$ do not appear in (6.12) since the third column of each D_j is zero). Let $v_j = [h_j, \dot{h}_j]$ and denote the first two (of three) columns of D_j by $\tilde{D}_j$. Combining equations (6.12) and (6.13) yields

$$\begin{aligned} \ddot{h}_j = -2\zeta\dot{h}_j - (1+z_j)h_j \; & +K[C_1x_j + C_2x_{j+1} + \cdots + C_rx_{j-1}] \\ & +K[\tilde{D}_1v_j + \tilde{D}_2v_{j+1} + \cdots + \tilde{D}_rv_{j-1}] \\ & +K[p_\ell^{j-1}\bar{f}]d(t) \end{aligned} \tag{6.14}$$

where $K = -2/(\pi\mu k^2)$. Combining (6.11) and (6.14) and setting the disturbance to be periodic in time $d(t) = e^{iwt}$ yields the following dynamics for blade one

$$\frac{d}{dt}\left[\begin{array}{c} v_1 \\ \hline x_1 \end{array}\right] = \left[\begin{array}{c|c} \mathcal{S}_1 & 0 \\ \hline 0 & 0 \end{array}\right]\left[\begin{array}{c} v_1 \\ \hline x_1 \end{array}\right] + \left(\sum_{j=1}^{r}\left[\begin{array}{c|c} \mathcal{A}_a^j & \mathcal{A}_b^j \\ \hline \mathcal{A}_c^j & \mathcal{A}_d^j \end{array}\right]\left[\begin{array}{c} v_j \\ \hline x_j \end{array}\right]\right) + \left[\begin{array}{c} \mathcal{B}_a \\ \hline \mathcal{B}_b + iw\bar{e} \end{array}\right]e^{iwt}, \tag{6.15}$$

where the structural and disturbance terms are

$$\mathcal{S}_j(z_j) = \begin{bmatrix} 0 & 1 \\ -(1+z_j) & -2\zeta \end{bmatrix}, \quad \mathcal{B}_a = \begin{bmatrix} 0 \\ K\bar{f} \end{bmatrix}, \quad \mathcal{B}_b = K\bar{f}\sum_{j=1}^{r} p_\ell^{j-1}\hat{B}_j \tag{6.16}$$

with $B_j = [\tilde{B}_j, \hat{B}_j]$ so $\tilde{B}_j$ captures the first two columns of B_j while $\hat{B}_j$ captures the third and last column of B_j. Aerodynamic coupling is given by the terms

$$\mathcal{A}_a^j = \begin{bmatrix} 0 \\ K\tilde{D}_j \end{bmatrix}, \quad \mathcal{A}_b^j = \begin{bmatrix} 0 \\ KC_j \end{bmatrix}, \tag{6.17}$$

and

$$\mathcal{A}_c^j(z_j) = \tilde{B}_j + \hat{B}_j\,[0,\ 1]\,\mathcal{S}_j(z_j) + KH_j, \tag{6.18}$$

$$\mathcal{A}_d^j = A_j + KG_j \tag{6.19}$$

where

$$G_i = \hat{B}_1 C_i + \hat{B}_2 C_{i-1} + \cdots + \hat{B}_r C_{i+1} \tag{6.20}$$

$$H_i = \hat{B}_1 \tilde{D}_i + \hat{B}_2 \tilde{D}_{i-1} + \cdots + \hat{B}_r \tilde{D}_{i+1}. \tag{6.21}$$

This completes the dynamics for blade one. All other blades follow by symmetry of $M(z)$ (equation (3.13)) and $B(z)$ (Lemma 3.5.1). Specifically, rename $[v_j, x_j]$ as x_j and let

$$M_1(z) = \left[\begin{array}{c|c} \mathcal{S}_1(z_1) + \mathcal{A}_a^1 & \mathcal{A}_b^1 \\ \hline \mathcal{A}_c^1(z_1) & \mathcal{A}_d^1 \end{array}\right],\ M_j(z) = \left[\begin{array}{c|c} \mathcal{A}_a^j & \mathcal{A}_b^j \\ \hline \mathcal{A}_c^j(z_j) & \mathcal{A}_d^j \end{array}\right],\ \beta(w) = \left[\begin{array}{c} \mathcal{B}_a \\ \hline \mathcal{B}_b + iw\bar{e} \end{array}\right] \tag{6.22}$$

for j between 2 and r. Then

$$\begin{bmatrix} \dot{x}_1 \\ x_2 \\ \vdots \\ x_r \end{bmatrix} = \underbrace{\begin{bmatrix} M_1(z) & M_2(z) & \cdots & M_r(z) \\ M_r(\varphi z) & M_1(\varphi z) & M_2(\varphi z) & \cdots \\ & \ddots & & \\ M_2(\varphi^{r-1}z) & M_3(\varphi^{r-1}z) & \cdots & M_1(\varphi^{r-1}z) \end{bmatrix}}_{M(z)} \begin{bmatrix} x_1 \\ x_2 \\ \vdots \\ x_r \end{bmatrix} + \underbrace{\begin{bmatrix} \beta(w) \\ p_\ell \beta(w) \\ \vdots \\ p_\ell^{r-1}\beta(w) \end{bmatrix}}_{B(w)} e^{iwt}. \tag{6.23}$$

Due to the form of the aerodynamic forcing in equations (6.6) and (6.7), the forcing vector B depends on the forcing frequency w. The required extension is straight forward. Forcing vector B in equations (4.3) now depends on forcing frequency ($B = B(w)$); this w dependence continues on through $\beta = \beta(w)$ in equation (4.67) till the final response approximation in equation (4.94) where α now depends on w.

6.4 Tuned Eigenvalues for the DFVLR Bladed Disk

The DFVLR cascade is an experimental setup designed to study transonic two-dimensional flow [SS84]. It consists of an array of blades (cascade) in a transonic wind-tunnel, there is no spinning disk. Since there exist accurate experimental results for this setup which permit reliable model validation, and because the CFD code used to generate the model is also two-dimensional, the DFVLR blade shape was chosen to generate the current low-order (rotating) bladed-disk model. The case selected for analysis has a steady state inlet flow with Mach number 0.82 at a relative flow angle of 58.5 degrees. Figure 6.2 shows the resulting steady state pressure contours within the blade passage. Structural parameters were chosen to represent a (realistic) compressor bladed disk on the verge of instability, to this end we chose a mass ratio of $\mu = 100$, a reduced frequency of $k = 0.125$ and a damping of $\zeta = 0.25$ which represents both the structural damping and any viscous aerodynamic damping not captured by the inviscid CFD model.

The resulting tuned system eigenvalues are shown in Figures 6.5 and 6.6. There are $r = 20$ blades and $m = 8$ states per blade, hence there are a total of $rm = 160$ eigenvalues. Figure 6.5 shows all 160 eigenvalues. Notice how the uncoupled aerodynamic eigenvalues ($\diamond$) are perturbed slightly by the structural/aerodynamic coupling, and how the structural blade-alone mode at $[-\zeta, \pm i]$ is split into the 20 nodal diameter coupled eigenvalues (the clustered of crosses at $[-0.25, \pm i]$). Figure 6.6 shows a zoom of these clustered "structural" modes, here each eigenvalue is numbered by its associated nodal diameter. Notice the lightly-damped 10th nodal diameter mode $\lambda_{10} = -0.00025 + 0.94164i$. It is this eigenvalue that will go unstable if we further decrease the reduced frequency, and its behaviour creates the sharp mistuning sensitivity.

6.5 Mistuning Results for the DFVLR Bladed Disk

This section discusses the mistuned behaviour of the DFVLR bladed disk model. As shown in equation (6.13), mistuning appears as the percent change in the blade structural frequency. Figure 6.7 shows the bladed disk behaviour for a random mistuning (generated by a normal

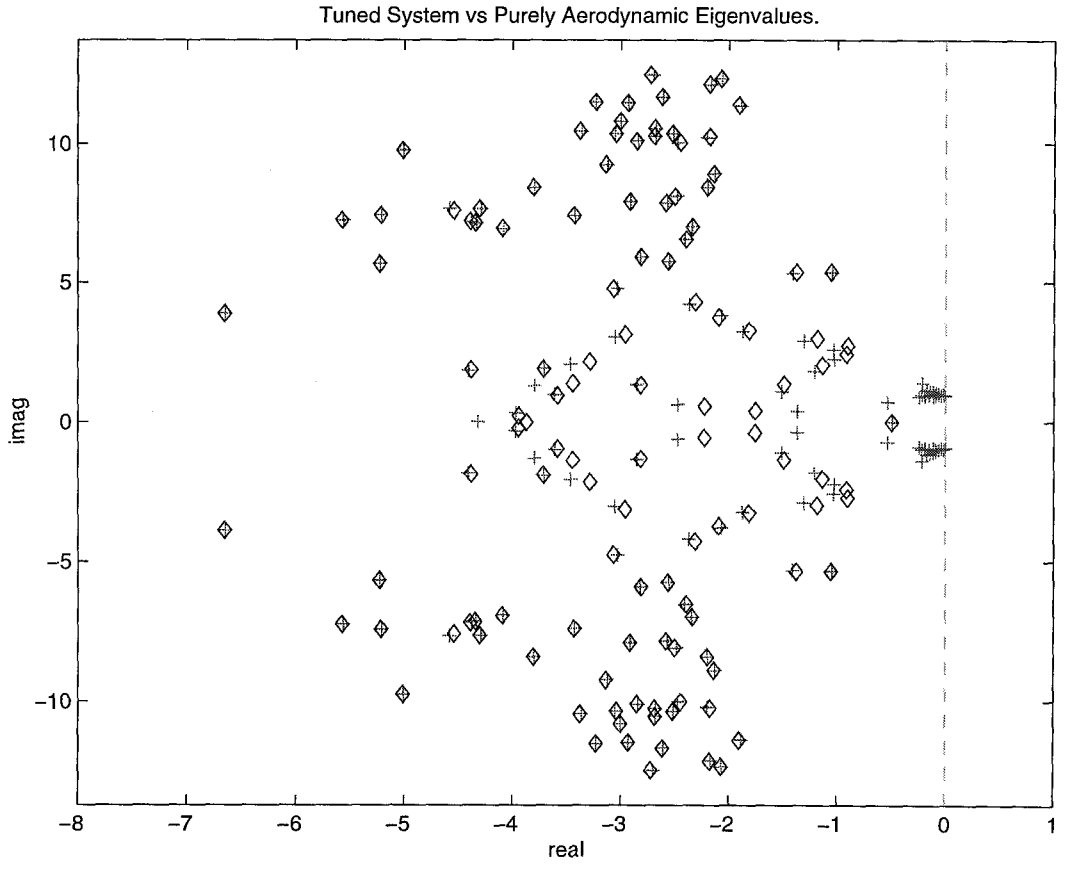

Figure 6.5: Tuned eigenvalues for the DFVLR cascade. Coupled structural/aerodynamic system eigenvalues (+), the uncoupled aerodynamic eigenvalues ($\diamond$).

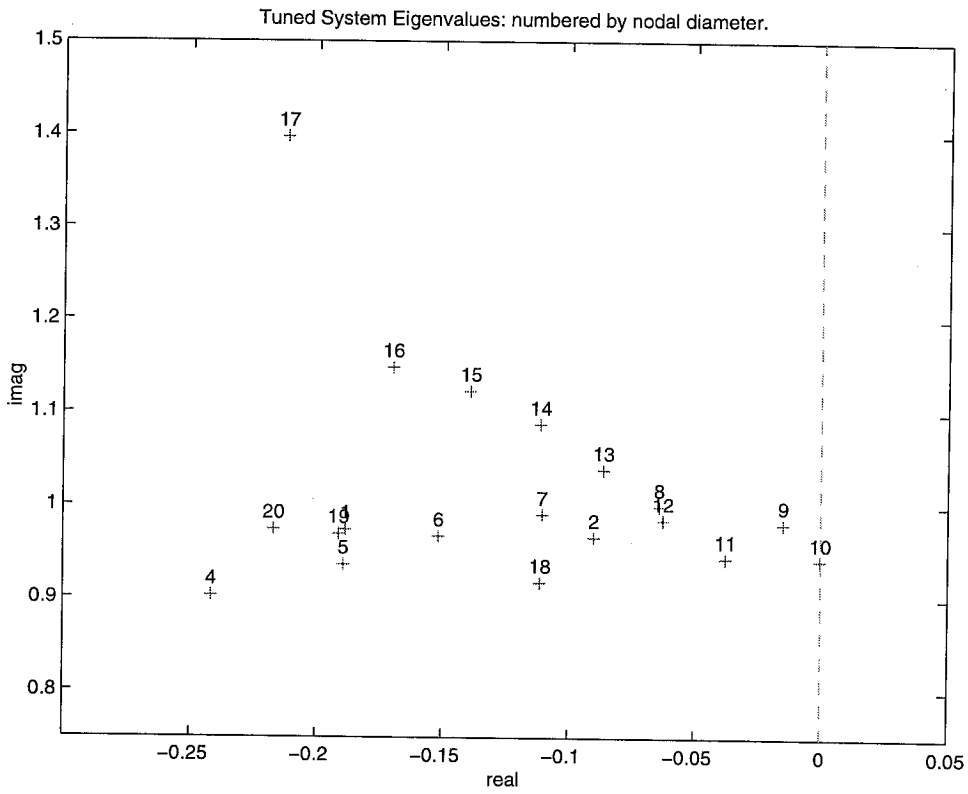

Figure 6.6: Zoom of tuned eigenvalues for the DFVLR cascade, eigenvalues numbered by their nodal diameter.

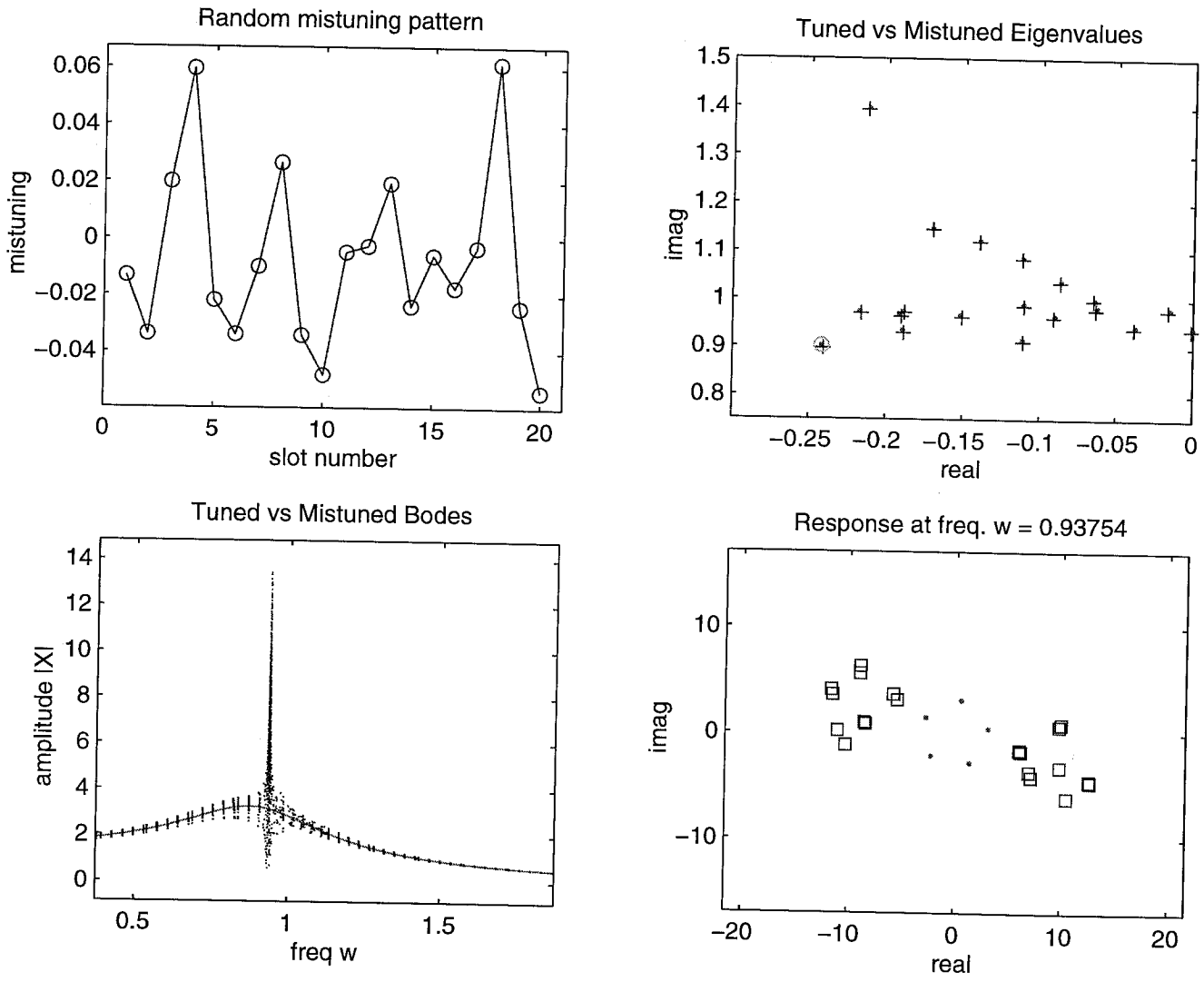

Figure 6.7: Random mistuning of DFVLR bladed disk. Top left: the mistuning pattern. Top right: tuned eigenvalues (dots), mistuned eigenvalues (crosses) [circle denotes $\ell = 4$ spatial forcing]. Bottom left: tuned response (solid), mistuned response (dashed—all 20 blades). Bottom right: at resonant forcing frequency the tuned response (dots), mistuned response (squares).

distribution with a 4% variance). To demonstrate mistuning sensitivity, we choose forcing in the fourth spatial mode ($\ell = 4$) because this corresponds to the most damped tuned eigenvalue in Figure 6.6. When the system is tuned, only the damped fourth nodal diameter eigenvalues are excited (denoted by the circled eigenvalue in the top right of Figure 6.7), and this yields a gentle tuned Bode plot (solid line, bottom left of Figure 6.7). However, when the system is mistuned, the lightly-damped 10th nodal diameter mistuned eigenvalue is excited, and this creates the sharp peak at the mistuned resonant frequency $w = 0.93754$ (dashed lines, bottom left of Figure 6.7; bottom right plot shows the complex amplitude and phase for all the blades at resonance). So the sensitivity mechanism for the DFVLR bladed-disk high-fidelity model is exactly the one described in Section 4.4.2 and Figure 4.11.

Moreover, Figure 6.7 shows that this specific random mistuning serves to stabilize the system; the mistuned eigenvalues are to the left of the tuned eigenvalues. In general, the eigenvalue perturbation of Chapter 4, equation (4.78), reveals which mistuning vectors are stabilizing for each eigenvalue. Plot 6.8 shows the number of destabilizing mistuning directions per eigenvalue. (For example, the eigenvalue third from the right has 2 destabilizing modes. Hence for a mistuning of the form $z = [1, \cos(2\pi j/r), \cos(4\pi j/r), \ldots, \cos(2\pi[r-1]j/r)]$, this eigenvalue is only destabilized by $j = 1$ and 2. This information is based on the eigenvalues of matrix $\mathrm{Re}[\Phi]$ in equation (4.78). Since Φ is symmetric and circulant, all eigenvalue of $\mathrm{Re}[\Phi]$ are real with eigenvectors of the form $v_j = [1, \cos(2\pi j/r), \cos(4\pi j/r), \ldots, \cos(2\pi[r-1]j/r)]$. Positive eigenvalues, $\rho > 0$, correspond to destabilizing directions: $v_j^T \mathrm{Re}[\Phi] v_j = \rho_j \|v_j\|^2 > 0$. Since Φ is invariant under the flip operator, mode j and $-j$ are equivalent (have the same eigenvalues) and so only $r/2$ directions need to be checked.) Since the mistuning vectors ($z = [1, \cos(2\pi j/r), \cos(4\pi j/r), \ldots, \cos(2\pi[r-1]j/r)]$, $j = 1, 2, \ldots, r$) span the mistuning space, Figure 6.8 reveals that some eigenvalues are always stabilized (or always destabilized) by mistuning. For example, the two most lightly damped eigenvalues in Figure 6.8 are always stabilized by mistuning, while the most highly damped eigenvalue is always destabilized. Hence mistuning tends to move the eigenvalues of Figure 6.8 closer to one another (least stable eigenvalues move left, most stable move right). The corresponding intuition is that since the model here is inviscid, there is no energy loss except through structural damping. Hence mistuning serves to exchange and spread the energy between different aerodynamic

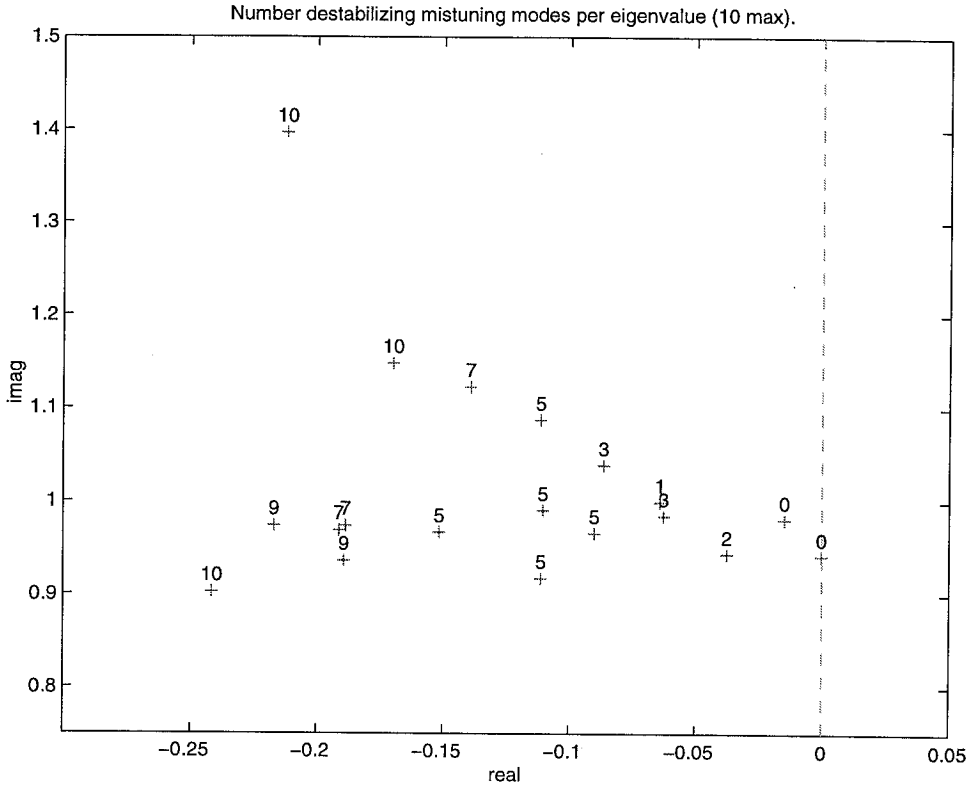

Figure 6.8: Number of destabilizing mistuning directions per eigenvalue.

modes and the eigenvalues move closer to one another.

Figure 6.8 above is based on the leading order eigenvalue approximation (4.78). Figure 6.9 addresses the region of validity for this perturbation. Here the chosen mistuning direction is in the first mode: $\hat{z} = [1, \cos(2\pi/r), \cos(4\pi/r), \ldots, \cos(2\pi[r-1]/r)]$. Mistuning is varied along this direction as$z = \epsilon\hat{z}$ up to a 15% mistuning ($0 \leq \epsilon \leq 0.15$). The resulting exact and approximately computed mistuned eigenvalues are shown in Figure 6.9. It can be seen that the eigenvalue approximation of equation (4.78) predicts the leading order trends. When eigenvalues do not veer (as in the most critical least stable eigenvalue) the approximation holds up to about a 10% mistuning size. However, when eigenvalues come close to collision and veer away from one another they no longer follow the leading order trends. This is true for the eigenvalues clustered near the point $[-0.2, 0.98]$ in Figure 6.9. It can be seen that the exact eigenvalues (curved paths) veer away from one another; whereas the approximate

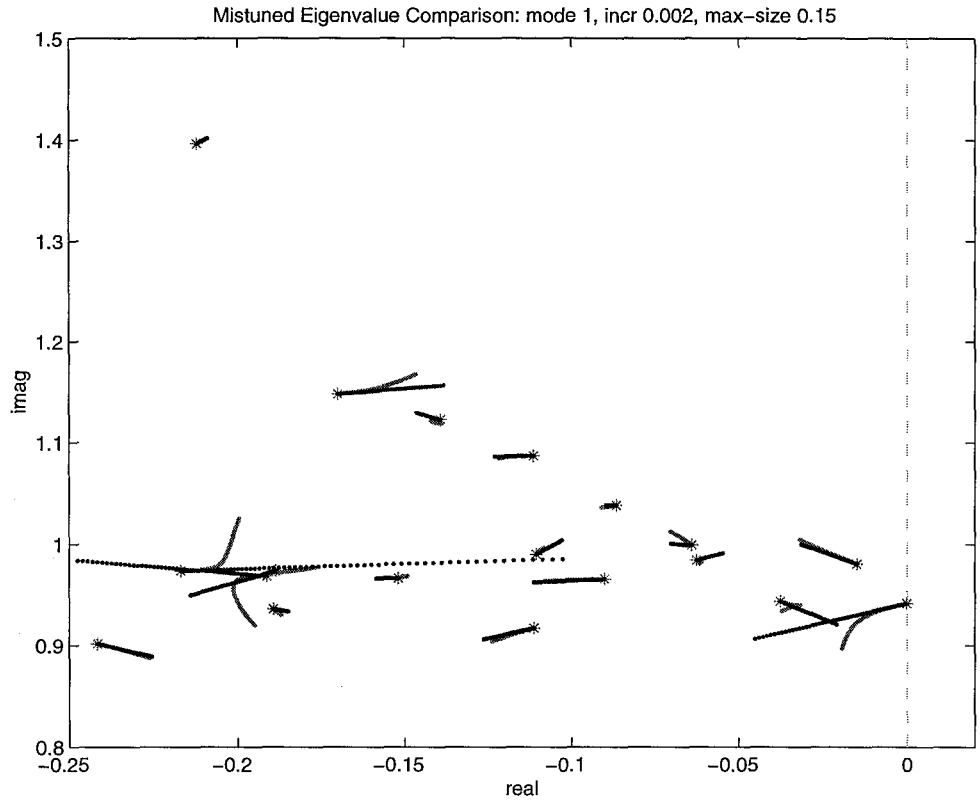

Figure 6.9: Eigenvalue motion with mistuning for the DFVLR model: tuned eigenvalues (*), exact mistuned eigenvalues (·, grey curved paths), approximate mistuned eigenvalues (·, black straight paths). (Note: eigenvalues move quadratically with mistuning size, so the least stable eigenvalue approximation is accurate up to about 10% mistuning.)

eigenvalue paths (straight lines) continue in their initial directions. Since forced response and stability are dominated by the least stable eigenvalues, the approximation scheme derived in Chapter 4 is quantitatively useful up to about a 10% mistuning size.

6.6 Mistuning Tradeoffs for the DFVLR Bladed Disk

Our purpose in this section is to compare the mistuning tradeoffs and sensitivities of the DFVLR high-fidelity model against the analytical results in Sections 5.2.1 and 5.2.2. Consider Figure 6.10, here we picked a random mistuning z_{rnd} and varied mistuning along this direction as $z = \epsilon z_{\text{rnd}}$ up to a 15% mistuning size ($0 \leq \epsilon \leq 0.15$). For each mistuning value z, a frequency sweep was performed over $0.9 \leq w \leq 1.1$ and the worst-case maximal-blade

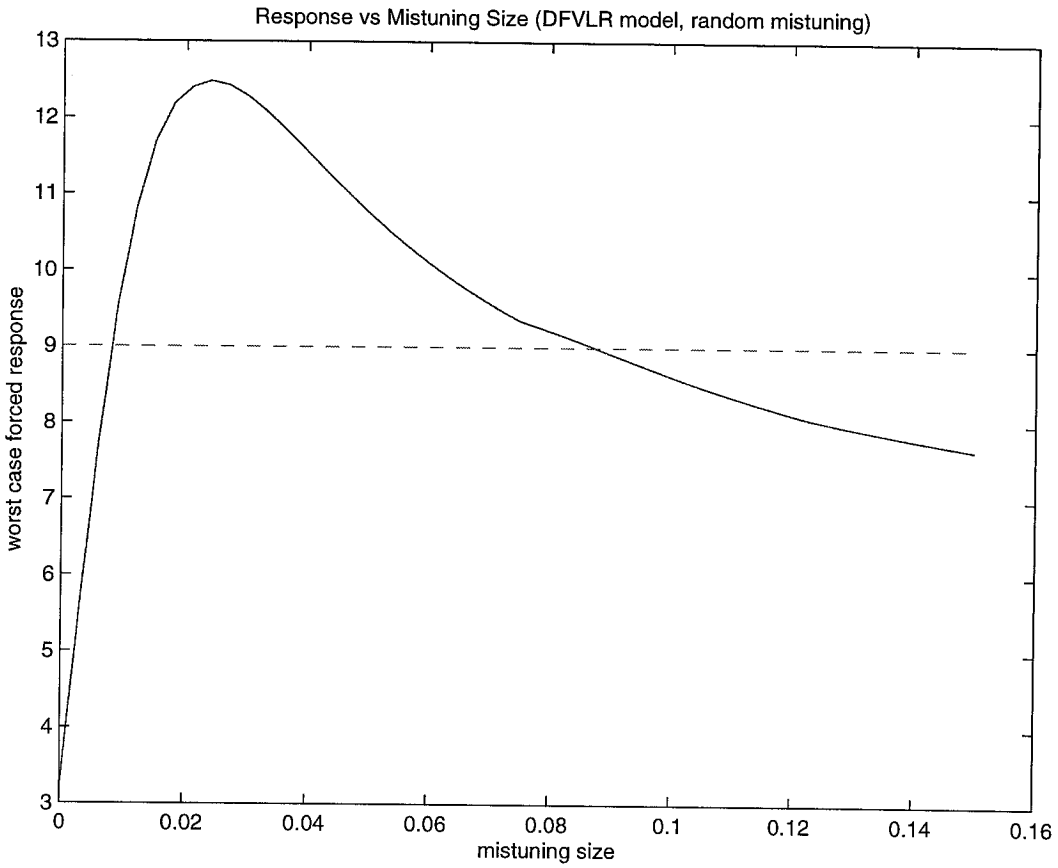

Figure 6.10: Exact worst case forced response vs mistuning size. Dashed line denotes the acceptable response level. (Compare with Figure 5.5 of Section 5.2.2.)

deflection was recorded: $\|X(z,\cdot)\|_\infty = \max_{(i,w)} |X_i(z,w)|$. (Hence this is the worst case over blades and frequencies.) This worst-case response $\|X(z,\cdot)\|_\infty$ is plotted against mistuning size in Figure 6.10. Notice that Figure 6.10 looks exactly like Figure 5.5 derived analytically in Section 5.2.2 from symmetry considerations. Its shape follows from equation (5.18) where the eigenvectors vary linearly in the numerator (initial response grows linearly as mistuned modes appear) but the increased damping due to the stabilizing mistuning appears quadratically in the denominator (the gradual response decrease). So the behaviour shown in Figure 6.10 follows directly from symmetry arguments which imply that eigenvalues vary quadratically with mistuning while eigenvectors vary linearly (see Sections 4.3.5, 4.4.2, 5.2.1 and 5.2.2).

Moreover, we can replicated the behaviour of Figure 5.4 in Section 5.2.1. To do so we pick two random mistuning directions z_{rnd1} and z_{rnd2}, and let the mistuning vary as $z =$

$\alpha z_{\text{rnd1}} + \beta z_{\text{rnd2}}$ where α and β range between -0.15 and 0.15. This creates a two-dimensional slice of the mistuning space shown schematically in Figure 5.4. For each mistuning value z, we check the worst-case (exact) response $\|X(z,\cdot)\|_\infty$. If this response is below the acceptable limit ($\|X(z,\cdot)\|_\infty < 9$ as shown in Figure 6.10) then the response is deemed acceptable and marked by a point ($\cdot$); otherwise the response is deemed unacceptable and marked by a bullet ($\bullet$). The resulting plot is shown in Figure 6.11 (there are no unstable regions because all mistuning values serve to stabilize the two least-stable eigenvalues—see Figure 6.8). Notice that just as in Figure 5.4, Figure 6.11 has a small acceptable region about the

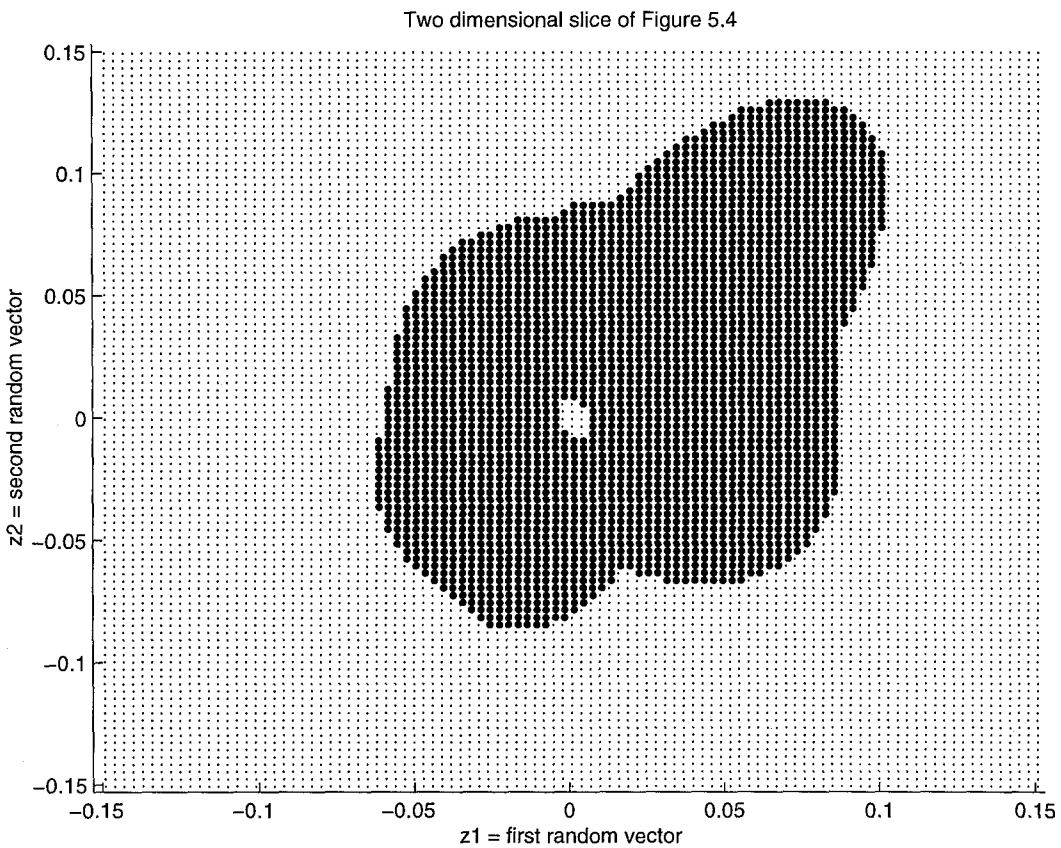

Figure 6.11: Acceptable/unacceptable forced response for a two-dimensional mistuning slice. Dots ($\cdot$) denote an acceptable response, bullets ($\bullet$) denote an unacceptable response. All points are stable. (Compare with Figure 5.4 of Section 5.2.1.)

origin surrounded by an unacceptable region (corresponding to the unacceptable peak of Figure 6.10) which is in turn surrounded by another acceptable region (corresponding to the tail of Figure 6.10). Consequently, as in Figure 5.4 the origin is not robust; even a small

random mistuning will lead to unacceptable response. However, there might exist a robust intentional mistuning outside the unacceptable region that will guarantee acceptable forced response even under manufacturing uncertainty. Such an intentional mistuning is derived in the next section.

6.7 Robust Intentional Mistuning for the DFVLR Bladed Disk

Since the mistuned forced response of the DFVLR model is dominated by the least stable 10th nodal diameter eigenvalue pair (see Figure 6.6), we can use the optimization results of Sections 5.1.1 and 5.2.2 to drive this eigenvalue pair to the left and improve both stability and worst-case forced response in a robust manner. To do so we solve the maximal-damping linear-constraint quadratic-cost optimization problem

3 *Optimization: Maximize* $\Delta\zeta(z) = -z^T \mathrm{Re}[\Phi] z$ *subject to* $\|z\|_\infty \leq 0.1$ *and* $\sum z_i = 0$.

which is analogous to optimization {1} in Section 5.1.1. Here we are finding the mistuning z that drives the least stable eigenvalue pair most effectively to the left, subject to a zero-average and infinity norm less than 10% constraint.

We can find the global optimals of problem {3} by using the branch and bound techniques described in [AKLV95]. The resulting global optimals are found to be

$$z^* = 0.1\,[1,1,1,1,1,1,1,1,1,1,1,-1,-1,-1,-1,-1,-1,-1,-1,-1,-1] \tag{6.24}$$

and any rotation $\varphi^j z^*$ thereof. Based on this optimum we can compute the quantity

$$\alpha^* = \mathrm{Re}\left[\frac{r\sigma}{\tilde{z}^T\Phi\tilde{z} - \bar{z}^T\Phi\bar{z}}\right] = 0.004 \tag{6.25}$$

which is analogous to equation (5.4) in Section 5.1.1. (Here $\tilde{z} = 10z^*$ is the optimal size one mistuning while $\bar{z} = [1,1,\ldots,1]$ corresponds to a tuned increase.) So purely from a stability viewpoint, intentional mistuning is worthwhile if its bigger then 0.4%.

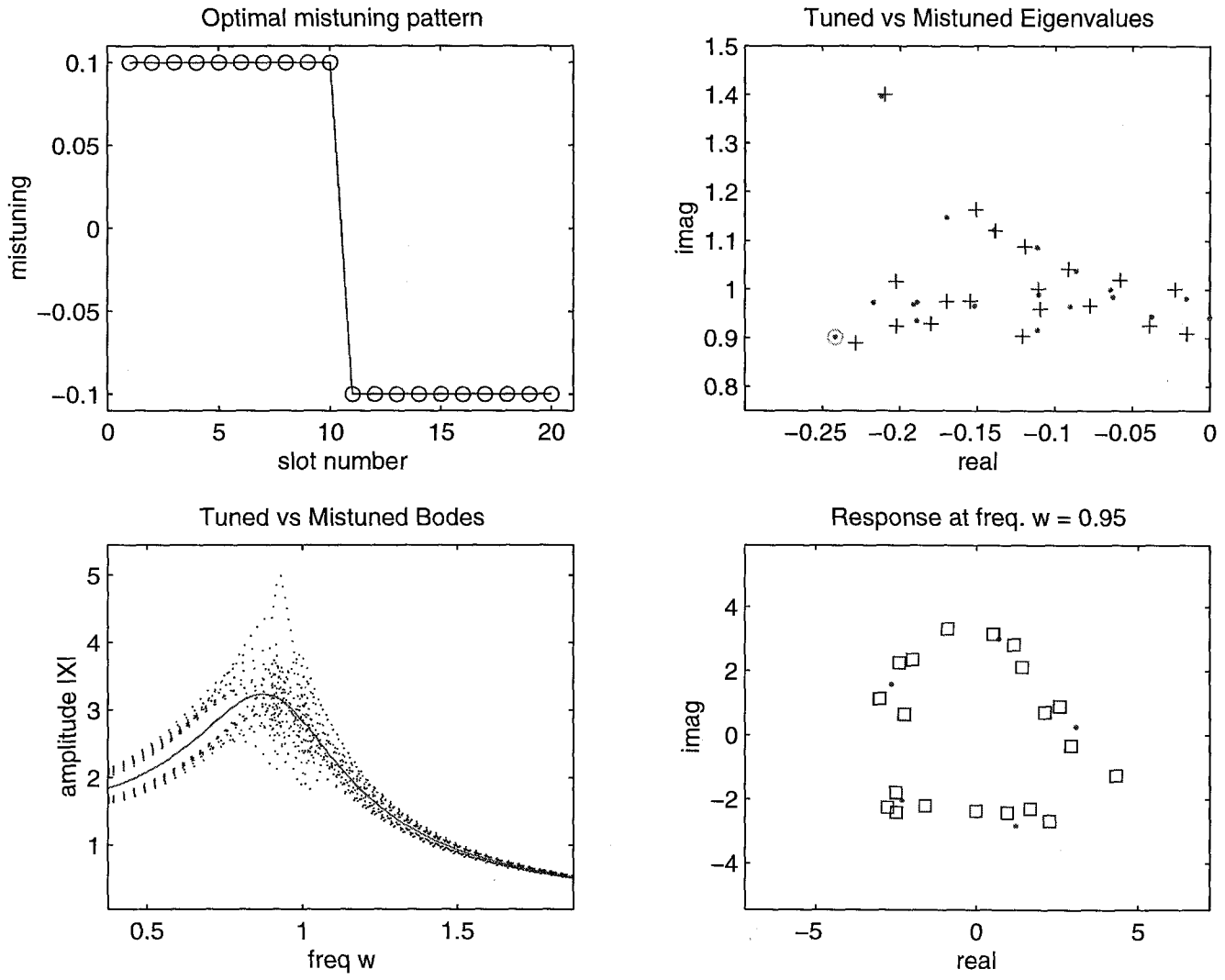

Figure 6.12: Optimal mistuning of DFVLR bladed disk. Top left: the optimal mistuning pattern. Top right: tuned eigenvalues (dots), mistuned eigenvalues (crosses) [circle denotes $\ell = 4$ spatial forcing]. Bottom left: tuned response (solid), mistuned response (dashed—all 20 blades). Bottom right: at fixed forcing frequency the tuned response (dots), mistuned response (squares).

Mistuning behaviour for the optimal mistuning (6.24) is shown in Figure 6.12. Notice how the mistuned eigenvalues have been pushed left; much more so than in the random mistuning of Figure 6.7. This creates a smaller mistuned forced response in Figure 6.12 as compared to Figure 6.7.

It remains to see if the improved response and stability behaviour created by the optimal mistuning (6.24) is robust to manufacturing tolerances. Suppose blades are produced with a random mistuning variation of 2%, meaning z_i varies uniformly between -0.02 and 0.02. Based on a Monte Carlo simulation, there is a 64% chances of unacceptable response about the origin: $\text{Prob}[\|X(\hat{z},\cdot)\|_\infty > 9,\ \hat{z}_i \in (-.02,.02)] = 0.64$. This is intuitively clear from Figure 6.11, within the 2% box about the origin there is a large probability of landing in the unacceptable region. For the case of intentional mistuning, robustness was not checked rigorously because the approximation (4.94) begins to break down at about 10% mistuning and so it is not possible to create a bound as in equation (5.22) and Figure 5.7. However, a Monte Carlo simulation was performed about the intentionally mistuned point and the worst-case forced response was acceptable over all points sampled. Specifically, it was shown that $\text{Prob}[\|X(z^* + \hat{z},\cdot)\|_\infty > 9,\ \hat{z}_i \in (-.02,.02)] < 0.001$. (A rigorous deterministic bound could be achieved by standard μ robust analysis techniques.) Figure 6.13 shows the behaviour for a typical optimal plus random mistuning: $z = z^* + z_{\text{rnd}}$ for $\|z_{\text{rnd}}\|_\infty \leq 0.02$. Notice that the forced response is well below the acceptable limit: $\|X(z^* + \hat{z},\cdot)\|_\infty < 9$. In conclusion, the introduction of the optimal intentional mistuning robustly improves both stability (the minimum damping) and the worst-case forced response.

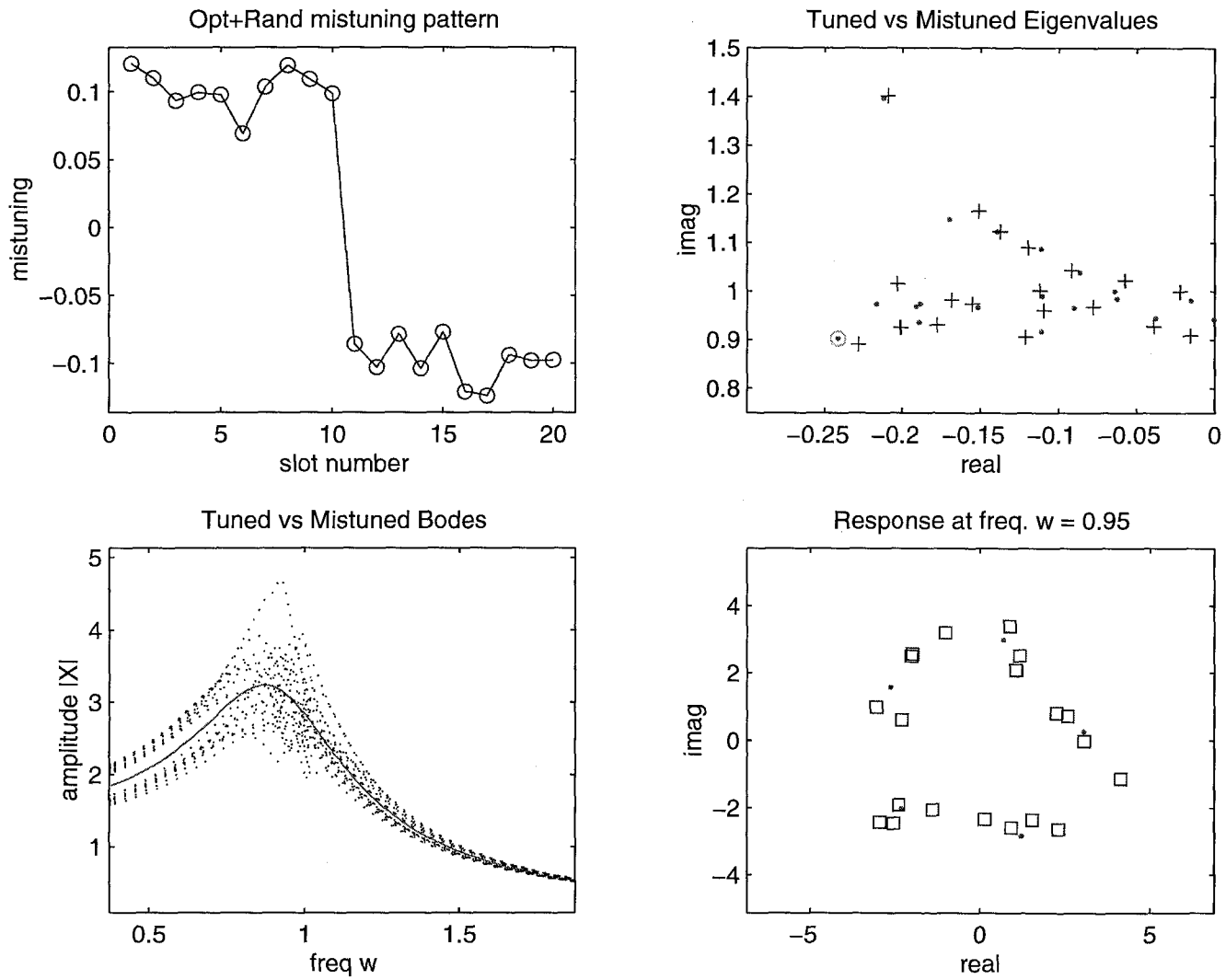

Figure 6.13: Optimal plus random mistuning of DFVLR bladed disk. Top left: the optimal plus random mistuning pattern. Top right: tuned eigenvalues (dots), mistuned eigenvalues (crosses) [circle denotes $\ell = 4$ spatial forcing]. Bottom left: tuned response (solid), mistuned response (dashed—all 20 blades). Bottom right: at fixed forcing frequency the tuned response (dots), mistuned response (squares).

Chapter 7 Summary and Future Work

This thesis addresses how mistuning affects bladed-disk performance, and examines the possibility of using mistuning as a robust passive control strategy to improve both stability and forced response. As a result, two basic questions are posed. The analysis question: given any mistuning, what is the new performance? And the optimization question: does there exist, and if so what is the best, intentional mistuning that robustly improves performance?

The analysis question is addressed in Chapters 3 and 4. Two basic techniques are used: symmetry arguments and an eigenvalue/vector perturbation. Chapter 3 covers symmetry arguments which are exact and hold for any model (linear, nonlinear, analytic or computational). Symmetry essentially says that if we take any mistuning pattern z and observe the resulting disk performance $P(z)$, then any rotation of the same mistuning pattern φz must yield identical performance $P(z) = P(\varphi z)$ because the two disks so mistuned are actually the same disk up to a rotation. The constraint $P(z) = P(\varphi z)$ must hold for all aspects of the mistuning problem (stability, response, eigenvalue/vector motion, optimization) and so greatly restricts the allowable behaviour. Exploiting this constraint allows a great simplifications of many mistuning issues.

Chapter 4 covers the eigenvalue/vector perturbation. This approximation method is aimed at the standard linear stability/response problem. An eigenvalue/vector approximation was chosen because bladed-disks are known to be lightly-damped. This means the eigenvalues can be very close to the imaginary axis and their motion, although small, can produce very strong nonlinear effects. By perturbing eigenvectors in the numerator and the inverse of eigenvalues in the denominator, we can accurately predict the forced response even in the lightly-damped, strongly-nonlinear case. Moreover, eigenvalues (the modes) and eigenvectors (the mode shapes) are fundamental quantities for linear systems, understanding their variation with mistuning is crucial. Throughout the eigenvalue/vector perturbation we exploit the symmetry results of Chapter 3. This not only eases the computational burden,

but also reveals underlying tradeoffs and aids in understanding the mistuning problem. (For example, symmetry implies eigenvalues vary quadratically with mistuning while eigenvectors vary linearly. This explains why the mistuned forced response first rises and then falls as mistuning size increases, see Figures 5.5 and 6.10 with associated discussion.)

Like any approximation technique, there are cases where the eigenvalue/vector perturbation performs poorly. When eigenvalues are close together, the eigenvalue motion is very abrupt and the eigenvectors may suffer motion discontinuities as eigenvalues collide. In this case the eigenvalue/vector perturbation method is only valid for very small mistuning (see Section 4.3.1, Table 4.1, for a comparison of the eigenvalue/vector method with a standard perturbation method in the literature). In practice this is a significant, but not severe, restriction. The high-fidelity model used in Chapter 6 has nearby eigenvalues yet the eigenvalue/vector approximation of Chapter 4 holds over a reasonable range, up to about 10% mistuning for the critical (least stable, non-colliding) eigenvalues, and certainly provides the correct leading order trends.

The passive control, or optimization, question is dealt with in Chapter 5. Due to the analysis of Chapters 3 and 4 we find that in order to have an intentional mistuning which increases stability and decreases forced response robustly, we must jump across an unacceptable region in the mistuning space to a point where significant damping has been introduced (see Figures 5.4 and 6.11). To do this, all eigenvalues (or at least eigenvalues within the frequency range of interest) must be moved left. If only a single eigenvalue pair is lightly-damped and within the range of frequencies being forced, than the relevant optimization reduces to the single eigenvalue problem of Section 5.1. The associated example in Section 5.2.2 shows that a robust intentional mistuning may be found that improves both stability and forced response. This has been demonstrated for the high-fidelity low-order aerodynamic model of Chapter 6. Here there is only one critical lightly-damped eigenvalue pair (this is because there is only a single structural mode per blade). Using the methods of Section 5.1, we find an intentional mistuning that robustly improves both stability and forced response for this high-fidelity model.

When multiple lightly-damped eigenvalues are important, it is necessary to push them all left. For a simple solution, one can examine all the relevant eigenvalue perturbations and

search for a mistuning mode p (i.e., $z_j = \cos(2\pi pj/r)$) that pushes all the relevant eigenvalue left. A better solution is to perform an optimization that always pushes the least stable eigenvalue left (such an optimization was performed to generate Figures 5.3).

In both single and multiple eigenvalue optimization cases there are two types of optimizations. Continuous optimizations are covered in Section 5.1.1, here one solves an optimization so as to build a disk with the optimal blade mistuning values. Section 5.1.2 covers discrete optimizations where one is choosing the optimal arrangement from a given set of blades. Once again, symmetry techniques can provide a great deal of simplification. For example, in Section 5.1.2 a discrete optimization problem is solved in closed-form. (If there were no symmetry present this problem would be NP (non-polynomial) hard and it would not be possible to find global optimums with even a small number of blades.) However, the given symmetry solution only holds for the class of models that have monotonically decreasing stability coefficients, at present there is no obvious extension to the general case of arbitrary stability coefficients.

Future work should focus on several extensions to the work in this thesis. First, a methodology should be developed for tracking sharply veering eigenvalues. There has already been some work in this area [AN89] but this research has not made use of symmetry to simplify the tracking. Essentially, symmetry provides a simplification of order r, where r is the number of blades. So without symmetry, if we wanted to track eigenvalues to third order we would have to find r^3 coefficients; with symmetry we need only find r^2 coefficients. For leading order terms this is a tremendous simplification, we can find the quadratic dependence of eigenvalues on mistuning with only $r/2$ terms (equation (4.78)). However, when eigenvalues start veering we very quickly need to start keeping track of third, fourth and fifth order terms (look at Figure 4.10 and notice how sharply the eigenvalues can move). Even though symmetry provides a simplification of order r, the growth in required coefficients is still explosive. Hence additional techniques for simplifying the perturbations must be found. At present, it is not clear how model structure (as discussed in Section 4.5) might aid in the analysis but this is a promising avenue of study.

Second, the optimization tools employed in this thesis consist of fairly standard packages (branch and bound algorithms, gradient descent with random seed, and so forth). Many

of these methods have severe limitations: exhaustive search algorithms such as branch and bound quickly become computationally prohibitive while random seek algorithms cannot guarantee an approach to global optimums. None of these standard packages exploit symmetry to aid in the optimization. Yet we know from Section 5.1.2 that symmetry can, in some cases, greatly simplify the relevant optimization problems. Hence the design and implementation of optimization tools that exploit system symmetry should be pursued.

Third, it is well known that bladed-disk models have a large uncertainty associated with them. This is especially true for models dealing with complex aerodynamic phenomena such as shock waves, tip-losses, viscous effects and, most notably, turbulence. Hence one would like to know if the mistuning results derived are robust to model uncertainty. (This is different from robustness with respect to mistuning uncertainty which is addressed in this thesis, see Section 5.2.1.) There are at least two ways to approach this issue.

Method one is to try make conclusions based purely on phenomenological data. For example, suppose we know that blade coupling is caused primarily by a leading-edge shock wave interaction. Is it possible to say anything about the resulting mistuned behaviour based only on this fact, i.e. can we make any conclusions without writing down a specific model? Information obtained this way would be robust (true for any model whose coupling mechanism is caused by leading-edge shock waves). Results of this type would be an extension to those presented in Section 4.5.

Method two deals with analyzing a set of models and is more along the lines of standard robust analysis. Suppose we have a set of models parameterized by a vector δ. Here δ might be the location of a blade shock wave, or it could capture small variations in blade-shape, operating-conditions or some other parameters of interest. (Creating such a set of models is itself a non-trivial task. The low-order modeling work in [WPP99] can serve as a starting point.) In general, one would like to find bounds on the perturbation mistuning parameters ($a, b, c, \sigma, \phi, \psi, \Phi, \alpha$ of equations (4.16), (4.78) and (4.94)), and on the resulting optimal mistuning (see Chapter 5) for all δ in some set Δ that describes model uncertainty. A limited way to do this is to compute derivatives of the mistuning coefficients with respect to the model parameters of interest ($\partial a/\partial\delta, \partial b/\partial\delta, \ldots, \partial\alpha/\partial\delta$). Now for small variations of δ we can find rough bounds on the motion of the mistuning coefficients. If we further know

that the optimal mistuning is related robustly to the coefficients (as in Section 5.1.2 where the optimal answer remains a pyramid arrangement, Figure 5.2, so long as the mistuning stability coefficients are monotonically decreasing, see equations (5.5) and (5.6)) then we have some information at which δ's the optimal answer will change. Hence to gain robust analysis results about the tuned point we need to push bounds on model variation δ through to bounds on the mistuning coefficients $a, b, c, \sigma, \phi, \psi, \Phi, \alpha$. To gain robust optimization results we must transform the bounds on the mistuning parameters into bounds on the optimal mistuning. Symmetry can, and should be, used to help simplify these questions. For example, symmetry can be exploited to help compute bounds on the mistuning perturbation coefficients.

Additionally, one would like to examine the robustness of any large intentional mistuning outside the perturbation validity range. In that case either a new perturbation scheme with a larger method of validity should be developed and exploited in the computations, or the analysis must proceed without the aid of a perturbation about the tuned point. Perturbing, instead, about a mistuned point disallows the use of symmetry arguments (the starting point is not symmetric) and makes the problem harder. If the mistuned point in question has a partial symmetry (for example alternate blade mistuning has the symmetry that rotating the disk by two blades returns the same disk) then this can be exploited. One could envision progressing the robust analysis from a large degree of symmetry (lots of structure but far from optimal), through points of less symmetry (less structure, closer to optimal) to the final point of interest (no or least amount of symmetry, optimal mistuning). Examining such an approach, and others, is suggested as a topic for future research.

Fourth, it is known that mistuning can cause large changes in stability. However, the question of how mistuning affects the transition to limit cycles (soft/supercritical or hard/subcritical bifurcation) has not been addressed. In order to answer this question nonlinear flutter models must be developed that will capture the nonlinear limit cycle behaviour. The corresponding mistuned bifurcation analysis would require an extension of the current symmetry tools to the nonlinear case.

Fifth, the symmetry tools developed herein apply to any object with rotational symmetry. Hence some of the tools developed in this thesis could apply to other devices of practical interest. Possible applications might included devices as diverse as circular saws, car-brake

hubs and computer drives. However, there also exist a wide class of devices that have other types of symmetry. For example, turbo-machine compression systems contain axial bearings and so there is an approximate axial symmetry (bearing j and bearing $j+1$ experience the same dynamics if we neglect edge effects). Exploiting (the possibly approximate) system symmetry in these cases to aid in the analysis should be examined.

Finally, the methods in this thesis should be examined experimentally. Currently, an experiment is planned at NASA Glenn that would examine the effects of damping and intentional mistuning on a bladed-disk in the NASA spin-pit facility (see Appendix B for a short description of the planned experiment). The aim of the experiment is to determine the range of perturbation validity, demonstrate mistuning sensitivity to damping, and to show the feasibility of robust intentional mistuning.

Appendix A MAST Software

MAST, an acronym for Mistuning Analysis by Symmetry Techniques, is written in Matlab, runs on Unix platforms, and implements the results of Chapters 3 and 4. This software has been optimized for speed (the 120 state model of Section 6.3 runs in approximately 20 minutes on a Sun Ultra 10, 433MHz machine) and is well commented. (There also exists an earlier Mathematica version of MAST, which is much slower.) At the time of writing, the latest available version was MAST 2.0 created in April, 1999.

This software is available free of charge, so long as all copyright header messages are retained. It may be obtained as follows:

- `ftp cds.caltech.edu`
- login: `anonymous`
- password: `your email`
- `cd pub/bshapiro/MAST`
- `get MAST2.0.tar` (or later version if available)
- `quit`
- `tar -xf MAST2.0.tar` (uncompress tar file).

This will create a directory structure with all the MAST files. Documentation and help is available in the file `README/Description`, notation used is consistant with this thesis.

To run MAST, the user must input the first block row of the linear model (4.3). The standard format is to enter this information in symbolic form as a function of the mistuning vector z. Given this model, MAST finds the leading order perturbation for all the eigenvalues (equation (4.78)) and the forced response (equation (4.94)) and prints this data out to an output directory. The user can vary the forcing mode ℓ to get a response approximation

for any mode of interest. Other information can be displayed on screen. For example, MAST computes the number of destabilizing mistuning modes per eigenvalues and shows a plot of the tuned eigenvalues number by the number of destabilizing mistuning modes for each eigenvalue. Related packages include some optimization tools (random search gradient descent tools). All MAST files contain short descriptions which outline their purpose and function. Any questions or comments about this software may be sent to the author.

Appendix B Planned NASA Glenn Experiment

The experiment described here is in cooperation with Oral Mehmed at NASA Glenn and is funded internally within the Smart Green Engine program (managed by Kestutis C. Civinskas), which is part of the Aeronautics and Propulsion Systems Base R & T effort (managed by Frank D. Berkopec). Existing NASA Glenn spin-pit facilities will be used. The basic aim is to examine the change in mistuning sensitivity due to damping, and to test the feasibility of introducing intentional mistuning to robustly improve both stability and forced response. To this end, the experimental configuration under consideration is the simplest possible that allows mistuning, variable damping and engine-order forcing. A (tentative) schematic of the experimental setup is shown in Figure B.1.

The bladed disk will be cut out of a sheet of steel, currently 8 blades are planned (only 4 are shown on the figure to avoid crowding). Variable weights on the tips of the blades will provide the mistuning capability while forcing will be achieved by air-injectors. By turning on from 1 to 8 air-injectors and varying the speed of rotation, we will be able excite the natural modes of the bladed-disk. Finally, the damping of the metal disk will be varied by attaching a thin layer of a visco-elastic material (sold commercially) topped by a thin-layer of metal (say aluminum or brass). The resulting metal-elastic-metal sandwich causes the elastic layer to shear when the material is bent. During bending motion this shear creates dissipation in the visco-elastic layer and hence causes increased damping. The resulting change in stiffness is very small. The amount of damping may be varied by changing the width and thickness of the attached "constrained-layer-damping" strips (see reference [YD72] for details and damping computations). The capabilities above will allows us to examine the dependence of mistuning sensitivity on damping, and the feasibility of intentional mistuning as a robust passive control strategy.

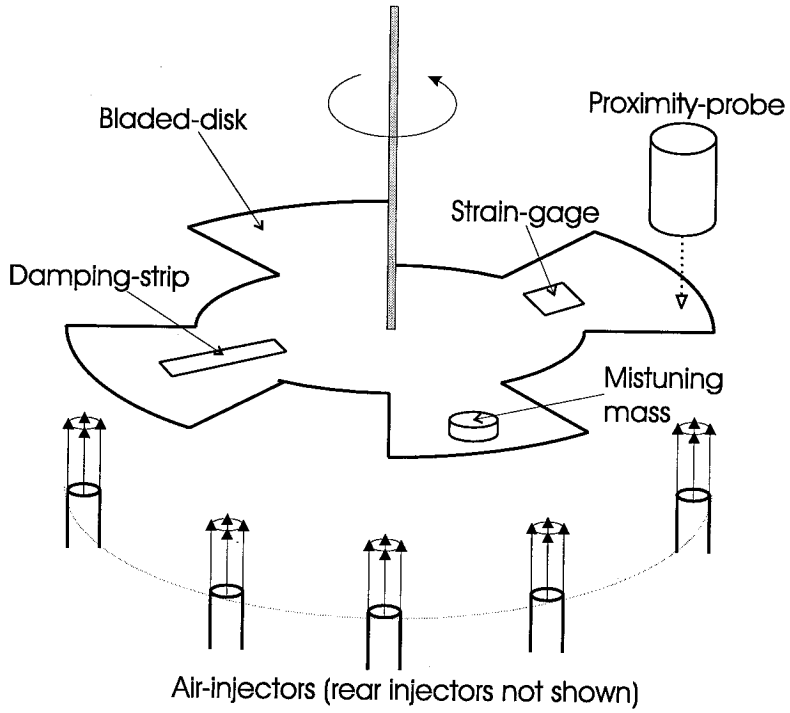

Figure B.1: Experimental Setup: all attached devices (masses, strain-gages, damping-strips, etc) are shown per blade and on top of the bladed-disk for clarity.

Bibliography

[AKLV95] F.A. Al-Khayyal, C. Larsen, and T. Van Voorhis. A relaxation method for non-convex quadratically constrained quadratic programs. *Journal of Global Optimization*, 6(3):215–230, 1995.

[AN89] D. Afolabi and O.D.I. Nwokah. The frequency response of mistuned cyclic systems. In *Vibration Analysis—Techniques and Applications; Twelfth Biennial American Society of Mechanical Engineers Conference on Mechanical Vibration and Noise*, pages 209–217, Jan 1989.

[Bat84] W. W. Bathie. *Fundamentals of Gas Turbines.* John Wiley & Sons, 1984.

[Ben84] O.O. Bendiksen. Flutter of mistuned turbomachinery rotors. *ASME Journal of Engineering for Gas Turbines & Power*, 106:25–33, 1984.

[Ben86] O.O. Bendiksen. Recent developments in flutter suppression techniques for turbomachinery rotors. *J.Propulsion*, 4(2):164–171, 1986.

[BF86] A. Bolcs and T.H. Fransson. Aeroelasticity in turbomachines; comparison of theoretical and experimental cascade results. Technical Report AFOSR-TR-870605, Ecole Polytechnique Federale de Lausanne, 1986.

[Blo87] H. Bloemhof. Flutter of mistuned cascades with structural coupling. In *Unsteady Aerodynamics & Aeroelasticity of Turbomachines & Propellers*, 1987.

[CH85] E.F. Crawley and K.C. Hall. Optimization and mechanisms of mistuning in cascades. *Transactions of the ASME*, 107:418–426, April 1985.

[Chi84] R.M. Chi. Mistuned flutter of shroudless turbomachine rotor blades. Technical report, United Technologies Research Center, East Hartford CT 06108, March 1984.

[Chi85] R.M. Chi. Separated flow unsteady aerodynamic theory. *Journal of Aircraft*, 22(11):956–964, 1985.

[Chi91] D.R.J. Chillingworth. *Bifurcation from a manifold*, volume 1463 of *Singularities Theory and its Applications, Lecture notes in mathematics.* Springer Verlag, 1991.

[CP97] M.P. Castanier and C. Pierre. Consideration on the benefits of intentional blade mistuning for the forced response of turbomachinery rotors. In *Proceedings of the ASME Aerospace Divison*, volume AD-55, pages 419–425, 1997.

[CS85] R.M. Chi and A.V. Srinivasan. Some recent advances in the understanding and prediction of turbomachine subsonic stall flutter. *Transactions of the ASME*, 107:408–417, April 1985.

[Dav95] O. Davenport. AFOSR high cycle fatigue workshop. Meeting Briefing, Oct 1995.

[DB84] J. Dugundji and D.J. Bundas. Flutter and forced response of mistuned rotors using standing wave analysis. *AIAA Journal*, 22(11):1652–61, 1984.

[DH69] R.C.F. Dye and T.A. Henry. Vibration amplitudes of compressor blades resulting from scatter in blade natural frequencies. *ASME Journal of Engineering for Power*, 91:182–188, July 1969.

[For94] H. Forching. Aeroelastic stability of cascades in turbomachinery. *Prog. Aerospace Sci.*, 30:213–266, 1994.

[GL97] F. Guyard and R. Lauterbach. Forced symmetry breaking perturbations for periodic solutions. *Nonlinearity*, 10:291–310, 1997.

[GM96] D.L. Gysling and M.R. Myers. A framework for analyzing the dynamics of flexibly-bladed turbomachines. In *International Gas Turbine and Aeroengine Congress and Exhibition*, 1996. ASME, 96-GT-440.

[Gre81] E. M. Greitzer. The stability of pumping systems—the 1980 freeman scholar lecture. *ASME Journal of Fluids Engineering*, 103:193–242, 1981.

[GS80] M. Golubitsky and D.G. Schaeffer. A discussion of symmetry and symmetry breaking. In *Proceedings of Symposia in Pure Mathematics*, volume 40, part 1, pages 499–515, 1980.

[GSS88] M. Golubitsky, I. Stewart, and D. G. Schaeffer. *Singularities and Groups in Bifurcation Theory*, volume 2. New York: Springer Verlag, 1988.

[KK82] K.R. Kaza and R.E. Kielb. Flutter and response of a mistuned cascade in incompressible flow. *AIAA Journal*, 20:1120–1127, Aug 1982.

[KMW98] M. Kim, J. Moon, and J.A. Wickert. Spatial modulation of repeated vibration modes in rotationally periodic structures. *Journal of Vibration and Acoustics*, 120, October 1998.

[Knu73] D.E. Knuth. *Sorting and Searching*, volume 3 of *The Art of Computer Programming*. Addison-Wesley, 1973.

[KP96] M.J. Kruse and C. Pierre. Dynamic response of an industrial turbomachinery rotor. In *Proceedings of the 32nd AIAA/ASME/SAE/ASEE Joint Propulsion Conference and Exhibit*, 1996.

[KP97] M.J. Kruse and C. Pierre. An experimental investigation of vibration localization in bladed disks, part i: Free response. In *Proceedings of International Gas Turbine and Aeroengine Congress and Exhibition, ASME, Orlando FL*, volume 97-GT-501, 1997.

[Lan64] P. Lancaster. On eigenvalues of matrices dependent on a parameter. *Numerische Mathematik*, 6:377–387, 1964.

[Lau96] R. Lauterbach. Symmetry breaking in dynamical systems. In *Nonlinear dynamical systems and chaos*, volume 19, 1996. Progress in nonlinear differential equations and their applications (Groningen).

[LWS93] M.B. Levine-West and M.A. Salama. Mode localization experiments on a ribbed antenna. *AIAA Journal*, 31(10):1929–1937, October 1993.

[MH97] M.P. Mignolet and W. Hu. Direct prediction of the effects of mistuning on the forced response of bladed disks. In *Gas Turbine and Aeroengine Congress and Exhibition*, June 1997.

[MK87] K.G. Murty and S.N. Kabadi. Some NP-complete problems in quadratic and nonlinear programming. *Mathematical Programming*, 39:117–129, 1987.

[MM88] O. Mehmed and D.V. Murthy. Experimental investigation of propfan aeroelastic response in off-axis flow with mistuning. In *24th Joint Propulsion Conference-AIAA, ASME, SAE and ASEE*, July 1988.

[NH85] E. Nissim and R.T. Haftka. Optimization of cascade blade mistuning, part II: Global optimum & numerical optimization. *AIAA Journal*, 23,no.9:1402–10, 1985.

[PD87] C. Pierre and E.H. Dowell. Localization of vibrations by structural irregularity. *Journal of Sound & Vibrations*, 114(3):549–64, 1987.

[PM77] M.H. Protter and C.B. Morrey. *A First Course in Real Analysis.* Springer-Verlag, 1977.

[PM92] C. Pierre and D.V. Murthy. Aeroelastic modal characteristics of mistuned blade assemblies: Mode localization and loss of eigenstructure. *AIAA Journal*, 30(10):2483–96, 1992.

[Pot72] J. H. Potter. The Gas Turbine Cycle, November 1972. ASME paper presented at the Gas Turbine Division Forum Dinner.

[SAB92] SAB. Report of the ad hoc committee on air force aircraft jet engine manufacturing and production processes. Technical report, U.S. Air Force Scientific Advisory Board, July 1992.

[SC85] A.V. Srinivasan and D.G. Cutts. Aerodynamically excited vibrations of a part-span shrouded fan. *Journal of Engineering for Gas Turbines and Power*, 107:399–407, April 1985.

[SC97] B. Shapiro and B.D. Coller. Characterizing optimal mistuning by symmetry arguments. In *IEEE Conference on Control Applications*, 1997.

[SF76] A.V. Srinivasan and H.M. Frye. Effects of mistuning on resonant stresses of turbine blades. In *Structural Dynamic Aspects of Bladed Disk Assemblies*, Dec 1976.

[Sha98] B. Shapiro. Symmetry approach to extension of flutter boundaries via mistuning. *Journal of Propulsion and Power*, 14(3):354–366, May-June 1998.

[Sin86] A. Sinha. Calculating the statistics of forced response of a mistuned bladed disk assembly. *AIAA Journal*, 24:1797–1801, 1986.

[Sir87] L. Sirovich. Turbulence and the dynamics of coherent structures. part 1: Coherent structures. *Quarterly of Applied Mathematics*, 45,no.3:561–571, October 1987.

[SS84] H.A. Schrieber and H. Starken. Experimental cascade analysis of a transonic compressor rotor blade section. *Journal of Engineering for Gas Turbines and Power, Transactions of the ASME*, 106:288–294, April 1984.

[Wat93] B.C. Watson. *An Investigation Into the Influence of Mistuning on the Forced Response of Bladed Disk Assemblies.* PhD thesis, Georgia Institute of Technology, 1993.

[Whi60] D.S. Whitehead. Force and moment coefficients for vibrating airfoils in cascade. *Great Britian A.R.C.*, R. & M. 3254, 1960.

[Whi64] D.S. Whitehead. Torsional flutter of unstalled cascade blades at zero deflection. *Great Britian A.R.C.*, R&M 3429, 1964.

[Whi66] D.S. Whitehead. Effect of mistuning on the vibration of turbomachine blades induced by wakes. *Journal of Mechanical Engineering Science*, 8:15–21, March 1966.

[WP90] S.T. Wei and C. Pierre. Statistical analysis of the forced response of mistuned cyclic assemblies. *AIAA Journal*, 28:861–868, May 1990.

[WPP99] K.E. Willcox, J.D. Paduano, and J. Peraire. Low order aerodynamic models for aeroelastic control of turbomachines. In *40th AIAA/ASME/ASCE/AHS/ASC Structures, Structural Dynamics and Materials (SDM) Conference, St Louis, MO*, volume 99-1467, April 1999.

[YD72] M.J. Yan and E.H. Dowell. Governing equations for vibrating constrained-layer damping sandwich plates and beams. *Journal of Applied Mechanics, Transactions of the ASME*, pages 1041–1046, 1972.